Title
Ultrafast X-Ray Absorption Spectroscopy of Isochorically Heated Warm Dense Matter

Author
Engelhorn, Kyle Craig

Publication Date
2015

Peer reviewed|Thesis/dissertation

Ultrafast X-Ray Absorption Spectroscopy of Isochorically Heated Warm Dense Matter

By

Kyle Craig Engelhorn

A dissertation submitted in partial satisfaction of the

requirements of the degree of

Doctor of Philosophy

in

Applied Science and Technology

in the

Graduate Division

of the

University of California, Berkeley

Committee in charge:

Professor Roger Falcone, Chair
Professor David Attwood
Professor Joel Fajans

Spring 2015

Abstract

Ultrafast X-Ray Absorption Spectroscopy of Isochorically Heated Warm Dense Matter

by

Kyle Craig Engelhorn

Doctor of Philosophy in Applied Science and Technology

University of California, Berkeley

Professor Roger W. Falcone, Chair

This dissertation will present a series of new tools, together with new techniques, focused on the understanding of warm and dense matter. We report on the development of a high time resolution and high detection efficiency x-ray camera. The camera is integrated with a short pulse laser and an x-ray beamline at the Advanced Light Source synchrotron. This provides an instrument for single shot, broadband x-ray absorption spectroscopy of warm and dense matter with 2 picosecond time resolution. Warm and dense matter is created by isochorically heating samples of known density with an ultrafast optical laser pulse, and X-ray absorption spectroscopy probes the unoccupied electronic density of states before the onset of hydrodynamic expansion and electron-ion equilibrium is reached. Measured spectra from a variety of materials are compared with first principle molecular dynamics and density functional theory calculations.

In heated silicon dioxide spectra, two novel pre-edge features are observed, a peak below the band gap and absorption within the band gap, while a reduction was observed in the features above the edge. From consideration of the calculated spectra, the peak below the gap is attributed to valence electrons that have been promoted to the conduction band, the absorption within the gap is attributed to broken Si-O bonds, and the reduction above the edge is attributed to an elevated ionic temperature.

In heated copper spectra, a time-dependent shift and broadening of the absorption edge are observed, consistent with and elevated electron temperature. The temporal evolution of the electronic temperature is accurately determined by fitting the measured spectra with calculated spectra. The electron-ion equilibration is studied with a two-temperature model.

In heated nickel spectra, a shift of the absorption edge is observed. This shift is found to be inconsistent with calculated spectra and independent of incident laser fluence. A shift of the chemical potential is applied to the calculated spectra to obtain satisfactory agreement with measured spectra.

Contents

List of Figures

List of Tables

Acknowledgements

This work would not have been possible without the support of a great many people. First, I would like to thank Roger Falcone for giving me the opportunity to pursue my post-graduate degree and for the calm and measured guidance I required along the way. I owe a great deal to Phil Heimann, whose patient mentoring has made this dissertation possible. I thank Byoung-ick Cho and Ben Barbrel for their technical expertise and companionship during long and sleepless experiments. I thank Alfredo Correa, Tadashi Ogitsu, and Vanina Recoules for their detailed calculations and invaluable knowledge. I would also like to thank Howard Padmore and Jun Feng for giving me the opportunity to work at Lawrence Berkeley National Laboratory and participate in the development of the streak camera. Finally, I would like to thank my parents and my girlfriend for their unconditional love and support.

Funding

This work was performed at LBNL under the auspices of the U.S. Department of Energy, Office of Science, Basic Energy Sciences, Materials Sciences Division Contracts No. DE-AC02-05CH11231. This material is based upon work supported at UC Berkeley by the U.S. Department of Energy, Office of Science, Office of Fusion Energy Sciences and by the National Nuclear Security Administration under Award Numbers DE-FG52-10NA29649 and DE-NA0001859.

Publications

A portion of the work presented in this dissertation has been previously published, submitted for publishing:

B. I. Cho, K. Engelhorn, *et al.*, Electronic Structure of Warm Dense Copper Studied by Ultrafast X-Ray Absorption Spectroscopy. *Phys. Rev. Lett*. **106**, 167601 (2011).

K. Engelhorn, B. I. Cho, *et al.*, The Electronic Structure of Warm Dense Silicon Dioxide. *Phys. Rev. B* (accepted).

Chapter 1

Introduction

Warm Dense Matter physics (WDM) is a growing research field with broad application and scientific interest. WDM is characterized by near solid densities and temperatures of 10,000 K to 100,000K [1]. In this regime, the temperature is comparable to the Fermi energy. This places WDM between the quantum mechanical regime of strongly degenerate matter and the classical regime of non-degenerate matter. Additionally, the temperature is comparable to Coulomb binding energy between the ions, so WDM may exist in plasma, gas, liquid, or solid phases. As a result, no one force or one phase dominates, and instead the complex interplay of physical phenomena makes WDM difficult to describe and model.

Figure 1.1 displays a density, temperature diagram of water, and identifies the phase space occupied by WDM. WDM lies between the developed fields of solid-state physics and plasma physics, and most physical descriptions of WDM are made by extrapolation of these two disciplines. However, many physical processes, which must be included for an accurate description of WDM, are neglected or treated as perturbations in these disciplines. As the models are extrapolated into the WDM regime and these processes become important, changes in physical behavior can be abrupt or discontinuous, so extrapolation becomes unreliable. Moreover, there have been few detailed experiments to provide the data necessary to guide and improve the theoretical understanding.

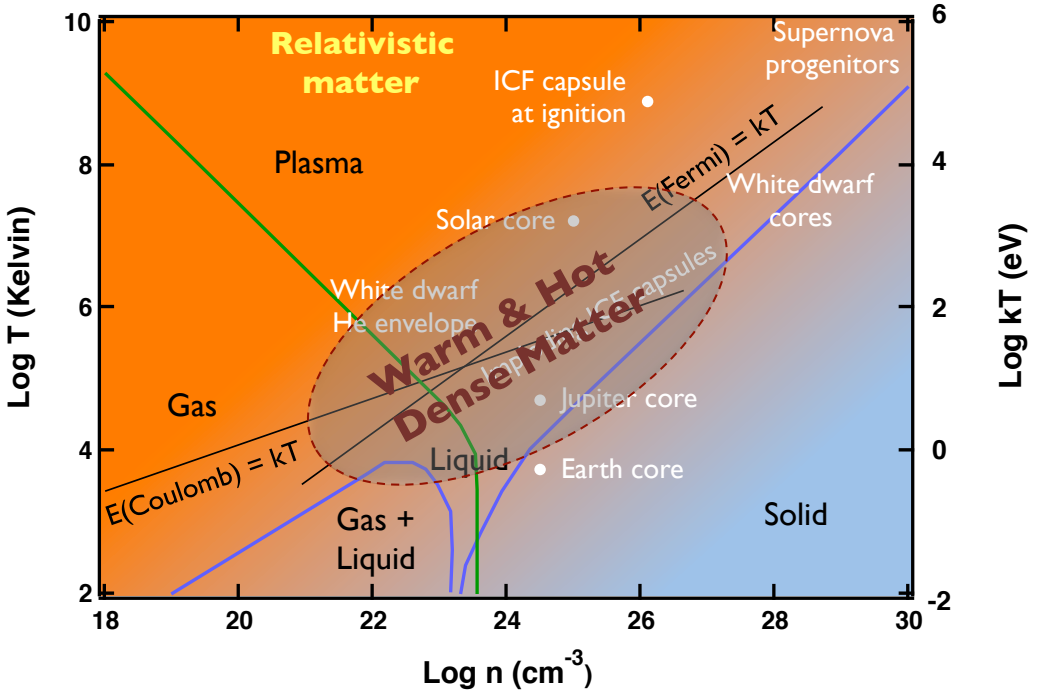

Fig. 1.1 Density temperature diagram of water. Adapted from [2].

Figure 1.1 provides a limited but not exhaustive set of astrophysical and experimental examples of WDM states (i.e. planetary cores, stellar cores, and ICF capsules). WDM states within astrophysics encompass a wealth of interesting but poorly understood planetary physics phenomena. As these WDM states occur within dense and thus opaque objects, study by traditional observational astronomy is not possible. This motivates a need for both laboratory experiments to create and study WDM, and a theoretical environment to describe WDM. In laboratory examples, the high temperature of WDM prevents the creation steady state samples, so sample creation and diagnosis becomes a fundamental challenge.

1.1 Motivations

Developing an understanding of WDM has relevance to the fields of material science, inertial confinement fusion (ICF), and planetary astrophysics [3-5]. These fields, while disparate in origin, size, and application, share the common need for theoretical models and experimental data of WDM.

Material science has seen an increased need for WDM models in recent years. The advent of modern lasers has allowed for new methods of material processing such as laser ablation [6-8], optical waveguide writing [9], and micro- and nanofabrication [10,11]. In all of these processes the laser energy is initially deposited in the electrons, by free-free, bound-free, or bound-bound absorption. If the laser pulse duration is shorter than the electron-phonon coupling time, the electrons will remain hotter that the ionic lattice until equilibrium is reached. This electronic excitation changes interatomic forces and can induce ionic motion, bond breaking, bond formation, and phase transitions. Accurately describing this scenario requires a precise Equation of State (EOS) and a detailed description of the electronic and ionic structure. WDM models are crucial to understanding how these transient states affect the final outcome.

In ICF temperatures and pressures far beyond that of WDM regime are achieved [12]. However, as an ICF capsule is compressed it traverses through the WDM regime and a thorough understanding of the EOS and energy transport properties is crucial to achieving fusion. In direct drive ignition, the capsule is compressed by a series of laser driven shocks [13]. The laser energy is initially coupled to the electrons, which equilibrate with the ions and results in ablation of the surface layers. The ablated layers form a coronal plasma that compresses the capsule by the rocket effect [12]. At early times, the rate and depth of electron-electron and electron-ion energy coupling determines the mass and temperature within the coronal plasma, which is essential to capsule design [14]. At later times, most the laser energy is absorbed in the coronal plasma and conducted to the imploding capsule via thermal electron transport [15], so accurate electron mean free paths are essential to capsule and laser design. Additionally, target homogeneity is crucial for avoiding hydrodynamic instabilities [16], so an understanding of phase transitions is crucial to avoiding local asymmetries that arise during phase transitions [17].

Developing an understanding of warm dense matter is also of critical importance to

planetary physics. There are many compelling planetary physics problems within the solar system, and with thousands of extrasolar planets now discovered [18], interest is extending far beyond it. The Earth's core is primarily composed of iron and nickel, with a solid inner region and a liquid outer region [19]. However, the exact crystalline phase of the inner core is unknown, and the outer core is much less dense [20], inconsistent with an isochemical phase transition. This suggest that the earths core also contains a significant portion of light elements [21]. Constraining the Earths composition is essential to understanding the accretion processes during formation, the formation of the moon [22], and the Earth's magnetic field, which is understood to involve a dynamo driven by convection of a conductive fluid [23]. Jupiter and Saturn played key roles in the formation and position of the other planets [24,25], so their formation is of particular interest [26]. Jupiter and Saturn are believed to consist of an inner core of rock and ice, a fluid metallic hydrogen shell, and a fluid molecular hydrogen shell [27]. Jupiter has an unusually strong magnetic field [28], and Saturn has an anomalous infrared luminosity [29]. Uranus and Neptune also consist of an inner rock and ice core, an 'ice' fluid shell of water, ammonia, and methane, and an outer layer of hydrogen and helium [5]. Uranus and Neptune have magnetic fields that are tilted from their rotation axis. A better understanding of these processes requires detailed understanding of material phases and electrical properties in the WDM regime.

1.2 Describing Warm Dense Matter

As previously mentioned WDM is described by thermal energies that are comparable to potential energies. This is shown in figure 1.1, where the degeneracy parameter is plotted. The degeneracy parameter, A, is equal to the ratio of potential energy to thermal energy,

$$\mathrm{A} = \frac{\varepsilon_f}{k_B T_e}, \varepsilon_f = \frac{\hbar}{2m_e}(3\pi n_e)^{2/3} \tag{1.1}$$

where ε_f is the Fermi energy, k_B is the Boltzmann constant, $\hbar^2$ is the reduced Planck constant, m_e is the electron mass, and n_e is the electron number density. When the degeneracy parameter is small ($\mathrm{A} \ll 1$) the electrons are unbound and behave classically. In this case, the electron occupation function follows a Boltzmann distribution.

$$\mathrm{f}(\varepsilon) = \sqrt{\frac{\varepsilon}{\pi k_B T_e}}\, e^{-\varepsilon/k_B T_e} \tag{1.2}$$

where ε is the electron energy. If the degeneracy parameter is large ($\mathrm{A} \gg 1$) then the electrons are mostly bound and behave degenerately. In this case, the electron occupation function follows a Fermi-Dirac distribution,

$$\mathrm{f}(\varepsilon) = \frac{1}{1 + e^{(\varepsilon-\mu)/k_B T_e}} \tag{1.3}$$

where μ is the chemical potential, and $\mu = \varepsilon_f$ at $T_e = 0$. The electron distribution is critical for determining many important physical parameters. The electrons near the Fermi level correspond to the outermost or valence states of atoms. These electrons distinguish metal from insulators, and determine parameters like the optical opacity, heat and electrical conductivity, electron heat capacity, and electron phonon coupling in atoms. As material transition into the WDM regime and the temperature increases, the electrons near the Fermi level are redistributed. This can transform insulators to metals, or otherwise drastically change material properties. As previously mentioned, many WDM experiments initially couple laser energy to electrons which then equilibrate with the ions, so two parameters of particular interest are the electron heat capacity and electron-phonon coupling constant [30]. The temperature dependent heat capacity is given by,

$$\mathrm{C}_e(\mathrm{T}_e) = \int \frac{\partial f(\varepsilon, \mu, T_e)}{\partial T_e} \rho(\varepsilon) \varepsilon d\varepsilon \tag{1.4}$$

where $\mathrm{C}_e(\mathrm{T}_e)$ is the temperature dependent electron heat capacity, and $\rho(\varepsilon)$ is the density of states. The temperature dependent electron-phonon coupling constant is given by,

$$\mathrm{G}(\mathrm{T}_e) = \frac{\pi k_B \lambda \langle \omega^2 \rangle}{\rho(\varepsilon_f)} \int \frac{-\partial f(\varepsilon, \mu, T_e)}{\partial T_e} \rho^2(\varepsilon) d\varepsilon \tag{1.5}$$

where $\mathrm{G}(\mathrm{T}_e)$ is the temperature dependent electron-phonon coupling constant, $\langle \omega^2 \rangle$ is the second moment of the phonon spectrum [31], and λ is the electron-phonon mass enhancement parameter [32]. The behavior of both of these parameters depends on the product of the electron occupation function and the density of states. In addition, as the electrons equilibrate with ions, the sample melts. This increases disorder and may result in bond breaking, which may also change the density of states. Therefore a describing WDM requires self-consistent treatment of both the electrons and ions in the system.

1.3 Molecular Dynamics and Density Functional Theory

In order to predict the behavior of materials in the WDM regime, models are extrapolated from traditional plasma physics or condensed matter theories. As this dissertation deals with near solid density material that is still highly degenerate, the best description is provided by modified condensed matter theories. Unlike traditional condensed matter WDM requires the treatment of disordered and dynamic ion systems and high temperature dependent electron structure. The most successful theoretical framework for describing WDM is molecular dynamics and density functional theory (MD-DFT).

Condensed matter presents complex multi-body problems that are difficult to solve analytically. DFT takes an iterative approach. DFT works by solving the Kohn-Sham

equations [33] (1.6, 1.7, 1.8),

$$\left[\frac{-\hbar^2}{2m_e}\nabla^2 + V_s(r)\right]\psi_i(r) = \varepsilon_i\psi_i(r) \tag{1.6}$$

where $\psi_i(r)$, is the i[th] electron wave function and ε_i, is the i[th] energy eigenvalue. This is essentially the Schrödinger equation, except that the effective single particle potential, $V_s(r)$, is written as a function of the electron density,

$$n_s(r) = \sum_i |\psi_i(r)|^2 \tag{1.7}$$

$$V_s(r) = \int \frac{n(r')e^2}{|r - \square'|} d^3r' - \sum_j \frac{Z_j e^2}{|r - R_j|} + V_{xc}\left[n_s(r)\right] \tag{1.8}$$

where Z_j is the effective nuclear charge (including screening) of the j[th] atom, and V_{xc} exchange-correlation. The exchange-correlation potential accounts for all the many particle interactions, which are often not known exactly but are instead approximated. It can be seen that $V_s(r)$ depends on $n_s(r)$, which itself depends on $V_s(r)$. So, these equations are solved in a self-consistent, iterative manner until a convergent solution is reached.

Unsurprisingly the effective potential also depends on the position and the screening of the ions in the system. Similarly, the ions will be affected by the electron density. So the ions must also be handled in a self-consistent, iterative way. This is done by molecular dynamics, where ion motion is treated classically. The combined process (MD-DFT) proceeds in the following manner, the ions are fixed and the electron wave functions are determined by the DFT process described above, these wave functions are used to calculate the forces on the ions and the ions are advanced by a small time-step, the ions are again fixed and the process repeats until equilibrium is achieved [34]. This is computationally expensive, but yields the detailed electron wave functions and ion positions from which material properties can be calculated.

1.4 Isochoric Heating

As mentioned in section 1.3**,** MD-DFT calculations are strongly dependent on both density and temperatures, so these calculation would ideally be confirmed by measurements on volumetric and uniform samples of a single density and temperature. However, creating such idealized states is experientially difficult. There are methods for volumetrically heating WDM such as, laser driven shock [35], x-ray heating [36,37], and ion heating [38]. These methods are advantages because thick samples can be heated uniformly. However, the high temperature and density of WDM results in high-pressure states that may be in local thermodynamic equilibrium but are not in global thermodynamic equilibrium. WDM samples cannot be maintained in a steady-state and undergo rapid hydrodynamic expansion within 10-100 picoseconds [39]. These heating

methods while rapid, μs-ns, are slower than the time-scales for expansion, and measure samples of poorly constrained density. To constrain sample density, the best method of creating a uniform WDM sample is isochoric heating. Derived from the Greek words isos, meaning equal, and choros, meaning space, isochoric heating describes systems that are heated at constant volume. In WDM studies, isochoric heating refers to the process where a sample of known density is heated quickly and studied before significant expansion occurs. Modern short pulse lasers systems achieve this by heating material to WDM conditions on ultrafast time scales (100 fs).

During laser heating, the incident laser energy is absorbed by the electrons in the material. This creates a population of non-thermal electrons with high kinetic energy. If photoabsorption (equation 1.9) is the dominant absorption mechanism, the kinetic energy of the excited electrons will be approximately equal to the photon energy, approximately 1-5 eV for optical photons. However, at high intensities the electric field of the laser is capable of accelerating electrons to high kinetic energies via the pondermotive force. This can produce electrons with kinetic energies that are much higher than the photon energy (e.g. a 1μm laser at 10^{14} W/cm^2 will generate electrons with a time averaged pondermotive energy of 20 eV for [40]). In both cases, these ballistic, non-equilibrium electrons travel through the sample with a velocity near the Fermi velocity, approximately ~10^6 m/s [41-43], and quickly equilibrate via electron-electron scattering. This equilibration time can vary between 100 fs for electron energies of a few eV [44] to about a picosecond for electron energies of about 100 eV [45]. This ballistic electron conduction transports the laser energy into the electronic system over the mean free path (mfp), which can exceed 100 nm [44]. By designing the sample thickness to match the mfp (figure 1.2), samples thicker than the laser absorption length, typically 10 nm in metals at optical wavelengths [46], can be heated uniformly in femtosecond time scales. Electron-ion equilibration occurs on much longer time scales, approximately 1-100 ps [47,48]. Thus, the electronic temperature immediately following the laser pulse is determined by the electron heat capacity, and the evolution of the electronic and ionic temperatures is determined by electron-phonon coupling.

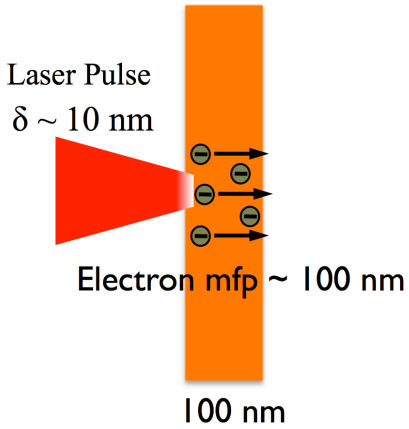

Fig. 1.2 Isochoric heating. The laser is absorbed in the optical skin depth δ, and ballistic electrons thermalize over the electron mean free path (mfp), which is matched to the target thickness.

1.5 X-ray Absorption Spectroscopy

MD-DFT calculations would ideally be confirmed by directly measuring the electron wave functions and their occupation along with the ion positions. However, no single experimental method provides complete information, and directly measuring the electronic wave functions is not experimentally possible. Instead a variety of methods must be utilized. In particular, absorption spectroscopy provides extremely detailed information on the electronic structure. It is also an efficient measurement, as it maintains source collimation. Photoabsorption occurs when a photon promotes an electron to a higher energy level, and the difference between energy levels is equal to the photon energy. Fermi's Golden Rule (equation 1.9) gives the probability of a photon with energy ε promoting electron in an occupied initial state, ψ_i, to an unoccupied final state, ψ_f,

$$P = \frac{2\pi}{\hbar}\left|\langle\psi_f|H|\psi_i\rangle\right|^2\rho_f(\varepsilon) \tag{1.9}$$

where ψ_i and ψ_f are the initial and final state wave functions, H is the electromagnetic Hamiltonian, and $\rho_f(\varepsilon)$ is the density of final states. To calculate the total probability of absorption for a given photon energy, this equation must be summed over all possible initial states for which a suitable final state exist. The valence and conduction bands of most materials posses many closely spaced states (ε~0-10 eV), so at optical and UV wavelengths there can be numerous combinations of initial and final states that result in absorption. This couples the density of states and wave functions of both the initial and final states, and makes rigorous interpretation difficult. Furthermore, typical absorption lengths in this range can be short (10 nm), so optical and UV light only sample the surface of many materials.

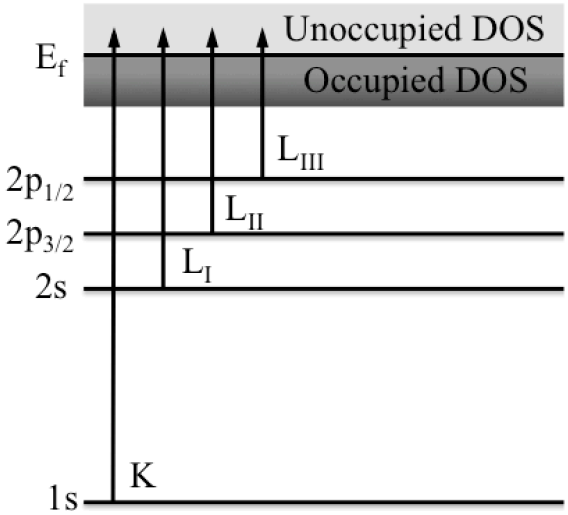

Fig. 1.3 X-ray absorption. Photo induced transitions form the n=1 state correspond to K-edge absorption, and transitions from the n=2 state correspond to L-edge absorption**.**

X-ray photons have sufficient energy to promote electrons from core levels to the Fermi level. The core levels of atoms are discrete and well-separated states (ε ~10 eV-

100keV), as shown in figure 1.3. Additionally, core states of atoms are less effected by material changes near the Fermi level and remain atomic like, so the wave functions are more easily calculated. Therefore, x-ray absorption spectroscopy (XAS) simplifies the problem by half and provides accurate measurement of the final states, as the initial states available are few, distinguishable, and well known. Furthermore, the binding energy of core levels of different atomic species are also well separated, so XAS allows selective measurement of a specific atomic species. Typical x-ray absorption lengths are also long (>100 nm) [49] and provide a better measure of the material volume.

X-ray absorption spectroscopy still has some limitations. First, absorption only occurs when the final state is unoccupied, so the occupied states cannot be measured. Second, equation 1.9 couples the matrix elements to the density of states. Finally, the matrix elements themselves have selection rules (i.e. $\Delta m=\pm 1$), so some entire bands may not be measured with a single initial state. Nonetheless, equation 1.9 can be used to calculate the absorption cross-section from a single initial state,

$$\sigma_\varepsilon = \frac{4\pi\hbar^2\alpha}{{m_e}^2\varepsilon}\left|\langle\psi_f|\boldsymbol{e}\cdot\boldsymbol{p}|\psi_i\rangle\right|^2\rho_f(\varepsilon) \tag{1.10}$$

where α is the fine structure constant, $\boldsymbol{e}$ is the x-ray polarization vector, and $\boldsymbol{p}$ is the momentum operator [50].

At room temperature, the Fermi occupation function (equation 1.9) is a sharp step function, with near completely occupied states below the chemical potential and near completely unoccupied states above the chemical potential. Since absorption can only proceed when the final state is unoccupied, the incoming photon must have sufficient energy to promote the electron to states above the chemical potential. This results in sharp x-ray absorption edges, as shown in figure 1.4. Traditionally, x-ray absorption spectroscopy is broken down into two categories, the absorption that occurs near the edge, X-ray Absorption Near Edge Spectroscopy (XANES), and Extended X-ray Absorption Fine Structure (EXAFS). While the absorption mechanism in these two regimes is the same, details of the final state wave function give different physical information.

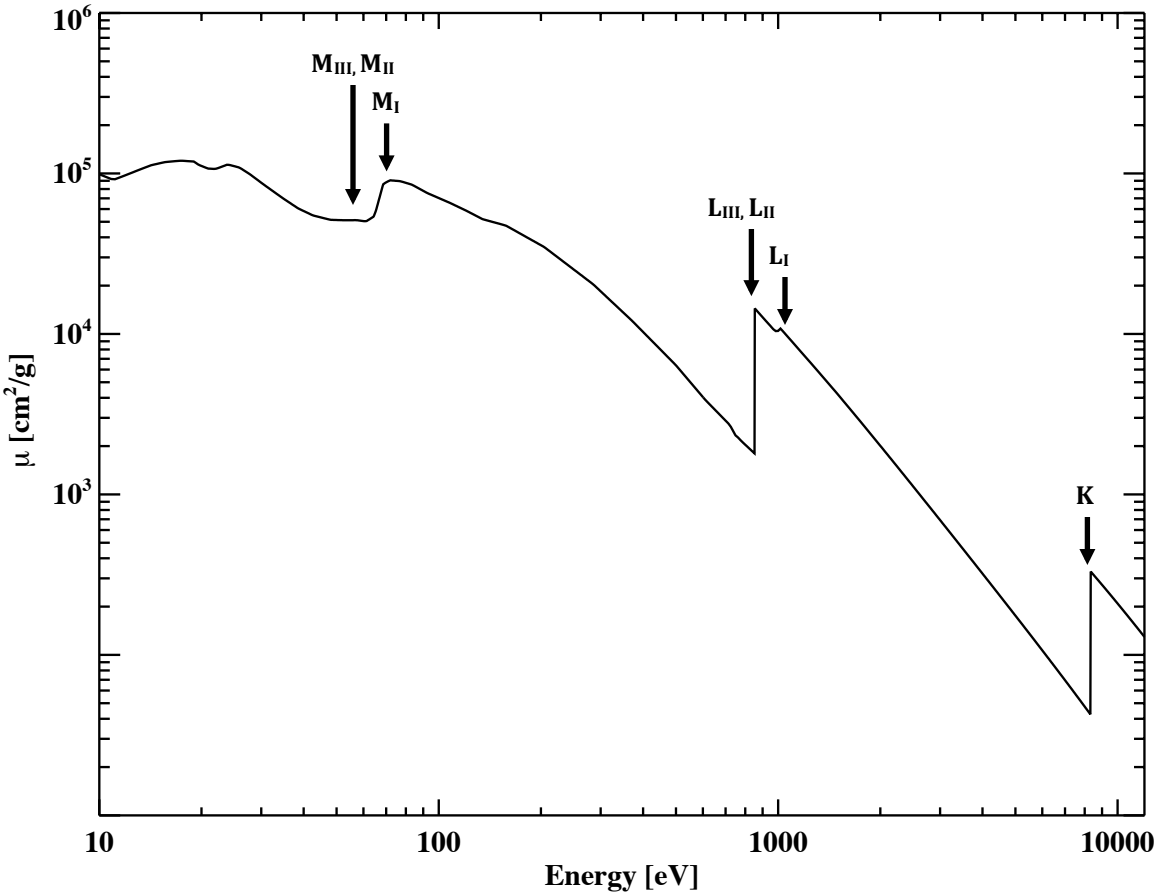

Fig. 1.4 X-ray absorption edges of Nickel. The M_I, M_{II}, M_{III} edges are seen at 111, 68, and 66 eV, respectively and correspond to initial states with n=3. The L_I, L_{II}, L_{III} edges are seen at 1,009, 870, and 853 eV, respectively and correspond to initial states with n=2. The K_1 is seen at 8,332 eV and corresponds to initial states with n=1. Generated from [49].

XANES includes the edge region, approximately 0-5 eV above the edge, and extends approximately 200 eV above the absorption edge. In the edge region, the absorbing electron is promoted to unoccupied states just above the Fermi level, so the absorption edge is set by the Fermi Occupation function (equation 1.9). The position and width of the edge provides an accurate measure of the chemical potential and electronic temperature. At higher photon energy (starting about 5 eV above the edge) the states are mostly unoccupied, except at very high temperature, and variations in the XAS provide valuable information on antibonding resonances and band structure. Above the edge, scattering of the final state wave function must also be considered. In the XANES regime, the photoelectron energy is small, and its corresponding wavelength is longer than interatomic distances and the scattering processes involve many atoms. Variations in the absorption spectra are caused by multiple scattering resonances and provide useful information on long-range atomic order. These factors make XANES a powerful technique for studying the electronic and ionic structure and temperature of WDM.

In EXAFS regime, the photoelectron energy is higher, and the electron wavelength is shorter than interatomic spacing, so variations in the absorption spectra result primarily from single-scattering events. EXAFS provides a useful tool for determining interatomic distances and can be used to determine material phase (i.e. BCC vs. FCC). In this regime, the absorption spectra are mostly smooth and EXAFS variations are small (typically 1%), so accurate EXAFS measurements require good signal-to-noise. The process of measuring X-ray absorption is simple. X-rays are propagated through a sample, and the transmitted intensity is measured (figure 1.5).

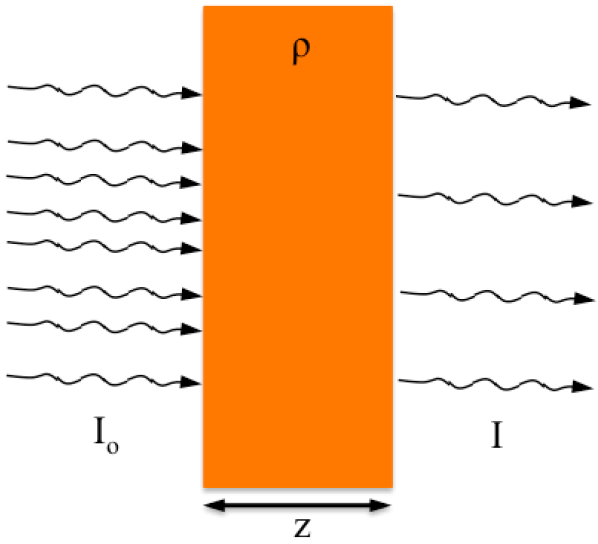

Fig. 1.5 X-ray absorption measurement.

The transmitted intensity is given by,

$$I(\varepsilon) = I_o(\varepsilon)e^{-\mu_\varepsilon \rho z} \tag{1.11}$$

where ε is the x-ray energy, I_o is the incident intensity, μ_ε is the mass absorption coefficient, ρ is the sample density, and z is the sample thickness. The mass absorption coefficient is given by,

$$\mu_\varepsilon = \frac{N_A}{A}\sigma_\varepsilon \tag{1.12}$$

where N_A is Avogadro's number, and A is the atomic weight, and σ_ε is the absorption cross section, as given in equation 1.10. For a sample of known composition, density, and thickness equations 1.11 and 1.12 accurate measure the absorption cross-section, which provides a rigorous test for MD-DFT calculations

1.6 Ultrafast XANES

Hydrodynamic expansion of WDM samples, as discussed in section 1.4, occurs on picosecond time scales, so to measure samples of known density, time-resolved

techniques must be used. Time-resolved XANES provides an accurate measure of electronic temperature and ionic correlation and has been used to study warm dense aluminum [9,51,52]. A broadening of the K edge and a smoothing of the absorption spectrum were observed as the solid sample becomes a liquid and then a plasma. Comparison with *ab intio* MD-DFT calculations revealed that the slope of the absorption edge was connected to the electron temperature, and the broadening of the edge was connected with a loss of ionic order in the high temperature liquid. These two experiments used protons or shock compression to heat the samples [9,51], and the relative timescales were 10's of picoseconds. As a result, electron-ion equilibrium was assumed, $T_e=T_i$.

This dissertation will present a technique for ultrafast XANES at the Advanced Light Source [53], which not only probes the sample before the onset of hydrodynamic expansion but also before electron-ion equilibrium is reached, $T_e>T_i$. The technique utilizes a Ti:sapphire laser to isochorically heat thin sample, an x-ray beamline including a spectrograph for broadband XANES measurements, and an ultrafast streak camera to provide 2 ps resolution. The experimental setup is discussed in detail in chapters 2 and 3. Results obtained on WD SiO_2, Cu, and Ni will be presented in chapters 4, 5, and 6.

Chapter 2

Experimental Setup

The experimental setup is comprised of three main components, the synchrotron and beamline, the laser system, and the x-ray streak camera. This chapter will cover the synchrotron, beamline, and laser configuration. These components undergo frequent changes in a constant effort to improve their operation, instead of cataloguing all of the changes made in the duration of the work presented, the mode of operation used for the majority of this work will be presented. The description of the streak camera operation and integration into the beamline is explained in chapter 3.

2.1 Synchrotron Operation

The experiments described in chapter 4 and 5 were preformed at the Advanced Light Source (ALS) at Lawrence Berkeley National Laboratory. The ALS is a third generation synchrotron facility, with the general layout shown in figure 2.1. This dissertation will not provide a detailed description of the synchrotron facility or its operation. Instead, a quick overview of the accelerator and storage ring operation is given in this section, along with a summary of the most important beam parameters.

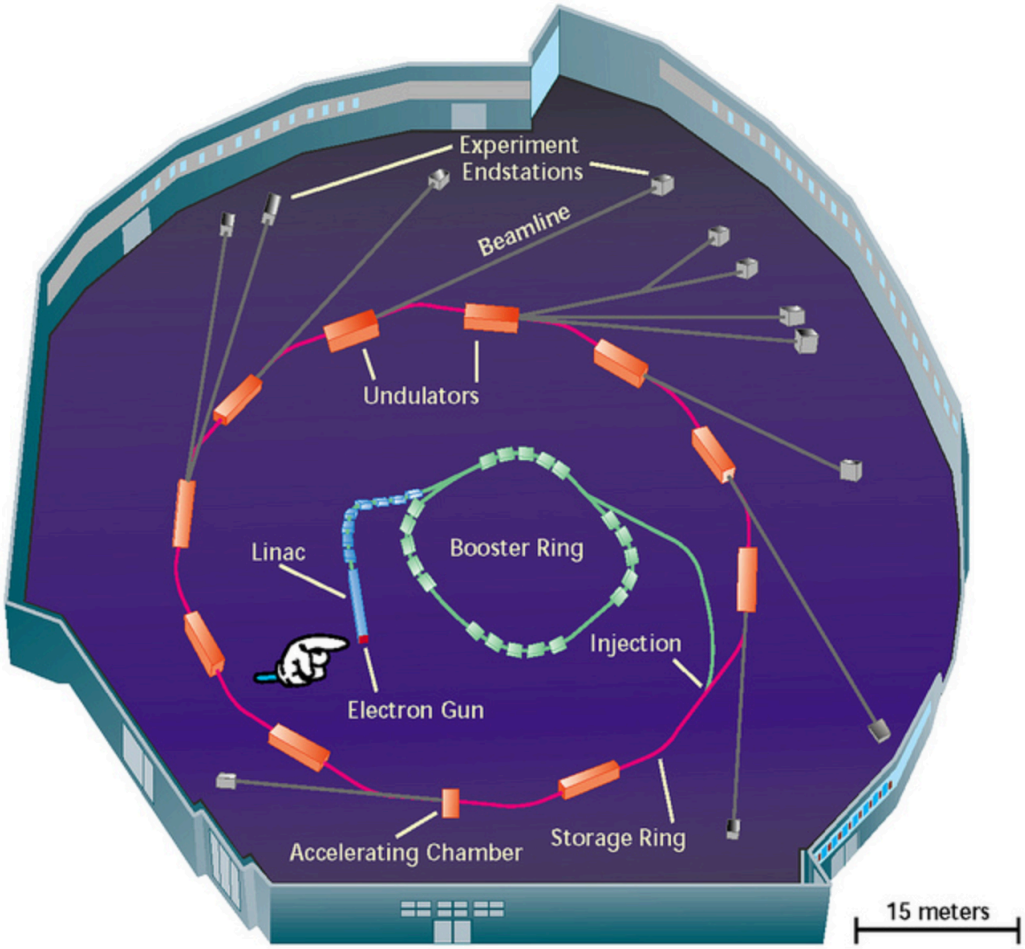

Fig. 2.1 ALS layout. Image courtesy of ALS, Berkeley Lab.

Synchrotron radiation is produced when a charged particle traveling at relativistic speed is accelerated radially. Synchrotrons facilities operate by accelerating electrons pulses or "bunches" to relativistic velocities (GeV energies) and storing them within an evacuated ring. The trajectory of the stored electrons pulses is altered by magnets and the induced accelerations maintain the electrons orbit within the ring. At the ALS, electrons are first produced by thermionic emission from a heated barium aluminate cathode. The extraction voltage of the anode is periodically pulsed to create bunches of electrons, which are then shaped by a buncher. The buncher can change the pulse duration or spilt the single bunch to several lower current bunches. These electron bunches are first accelerated by a traveling wave linear accelerator to ~50 MeV, and then enter a booster ring. The electrons make ~ 1 million round trips in the booster ring, receiving ~150 keV per round trip, and attain and energy of 1.5 GeV. The accelerated bunches are then injected into the storage ring. Within the storage ring a final RF acceleration chamber achieves an energy of 1.9 GeV. These RF cavities also compensate the electron energy for the radiation losses that occur within the ring. After the initial bunch injection, scattering processes also reduce the current stored within the ring, to compensate for this

electrons are continually added to the stored bunches to maintain a constant ring current ("Top off" mode).

The electrons are kept within the ring by a series of bending magnets that maintain an approximately circular orbit and an orbital period of 656 ns. The bend magnets cause the electrons to accelerate along a circular trajectory and produce a smooth spectrum, and relativistic length contraction reduces the forward emitted wavelengths into the x-ray regime. Alternatively, x-ray radiation can be achieved by inducing simple harmonic motion with a series of magnets of alternating polarity, undulators or wigglers. This can be understood as the electron undergoes many dipole oscillations in the rest frame. The periodic nature of undulators results in interference that narrows the emission angles and spectral width. This increases the spectral brightness, and undulators are typically several orders of magnitude brighter then bend magnets, making them preferential for the low repetition rate experiments. This can be seen in figure 2.2. A detailed description of synchrotron facilities, bend magnet and undulator radiation can be found in the references [54] and [55]. A schematic of an undulator is shown in figure 2.3. The x-rays, unaffected by the magnetic fields, propagate tangentially to one of 39 beamlines.

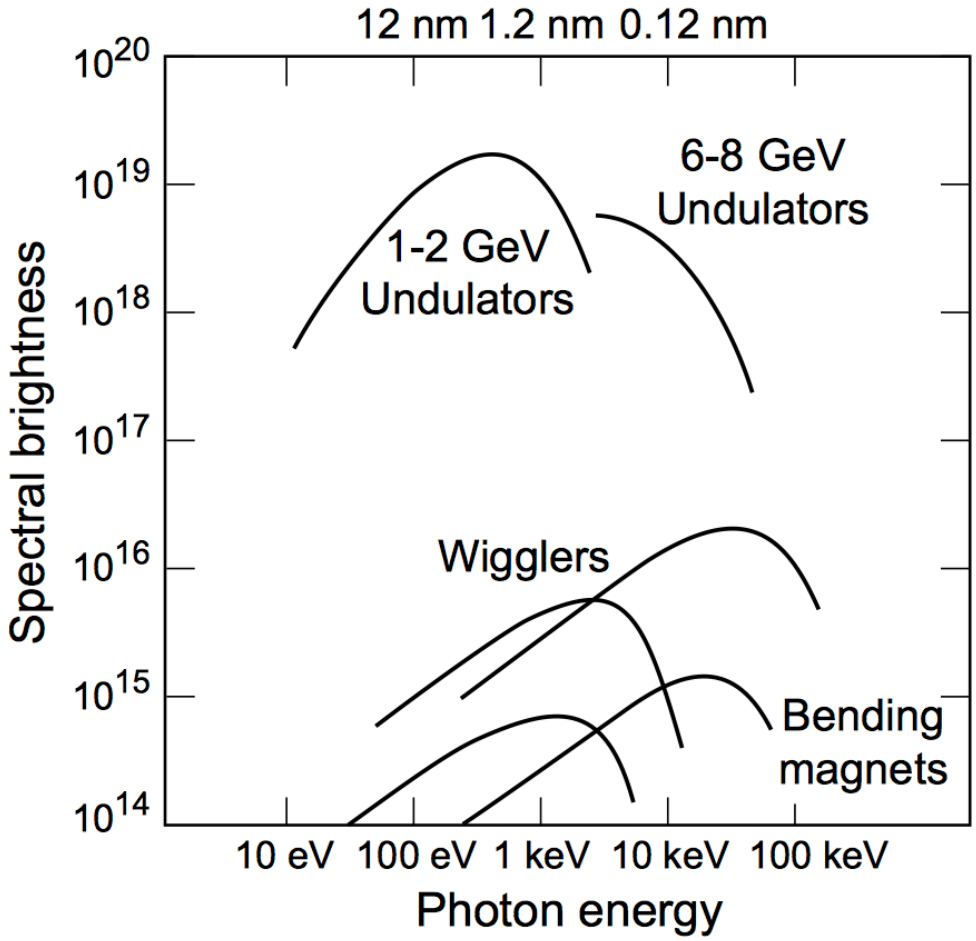

Fig. 2.2 Spectral brightness trends. Spectral brightness are in units of photons/s/mm^2/mrad^2/0.1% bandwidth [55].

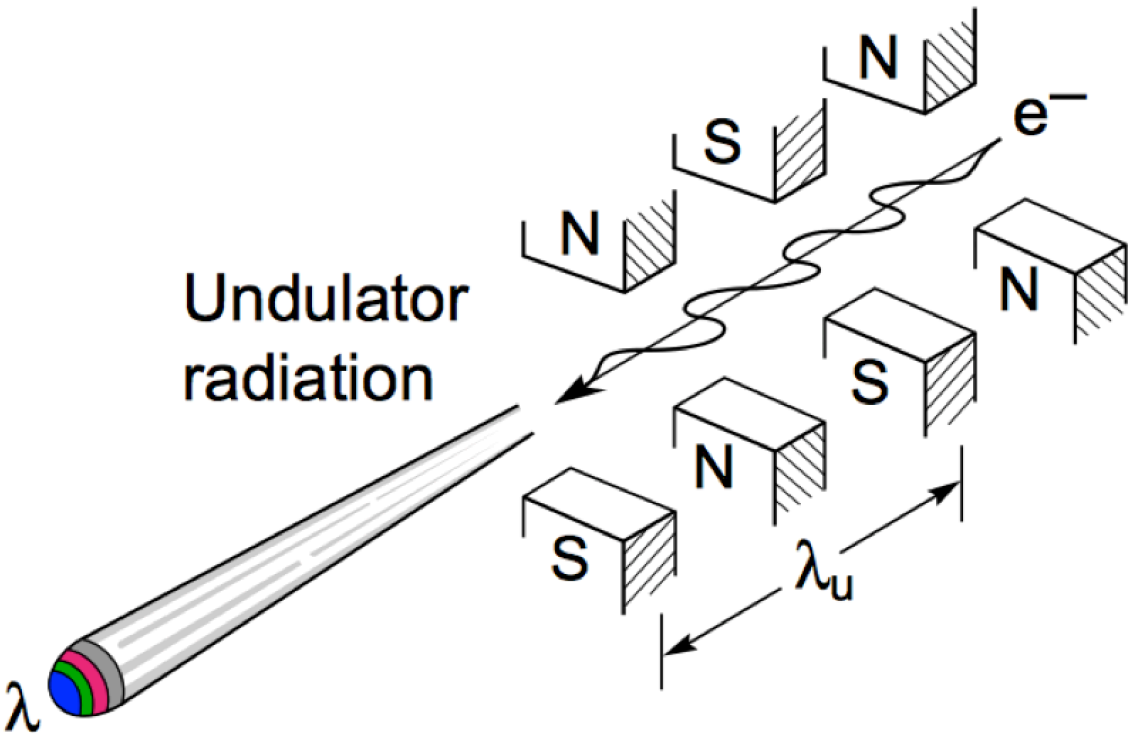

Fig. 2.3 Undulator schematic. Adapted from [55].

The storage ring operates in two modes. The primary mode, multi-bunch, operates at 500 MHz and 500 mA. In this mode, the ring is filled with 276-320 bunches (with an average current of ~2 mA each) which are separated by 2 ns. Additionally, there is a single bunch, the camshaft, with twice the current (~5.5 mA) within a ~100 ns gap. This serves two purposes. First, it allows the camshaft to be isolated with gated detectors (i.e. avalanche photodiodes or image intensifiers) for time resolved experiments that operate at a fraction of the ring frequency. Second, this gap allows ions attracted to the electron beam by the Coulomb force to clear the path, reducing the scattering of the electron bunch.

The second mode, two-bunch, operates at 3 MHz and 35 mA, filling the ring with just two bunches (~17.5 mA) separated by 328 ns. In both cases the electron beam size (RMS) in the straight sections of the ring is ~ 10 μm vertically and ~200 μm horizontally, Table 2.1 shows a more complete list of parameters for the ALS.

Mode	Energy (GeV)	Nominal Frequency (MHz)	Pulse Separation (ns)	Current per pulse (mA)	Pulse Duration (ps)	Horizontal size (μm)	Vertical size (μm)
Multi-bunch	1.9	500 MHz	2	2	70	200	10
Two-bunch	1.9	3 MHz	328	17.5	70	200	10

Table 2.1 ALS operating modes.

2.2 The X-ray Beamline

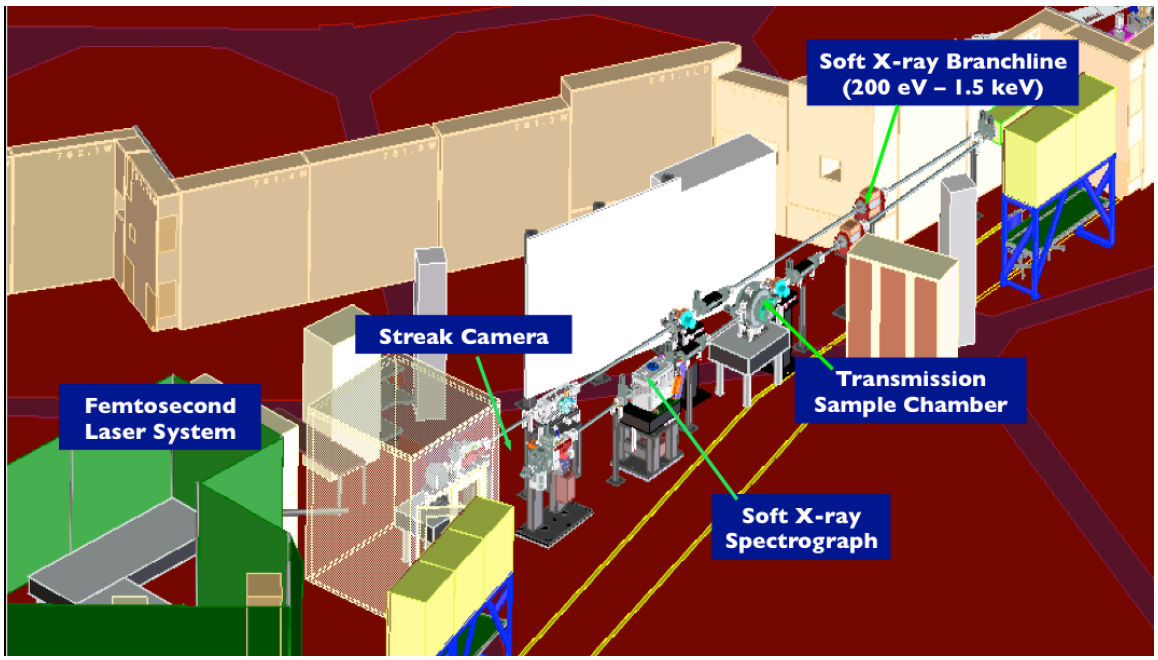

Fig. 2.4 Beamline layout. The general layout of BL 6.02 at the ALS including the laser hutch (shown in green).

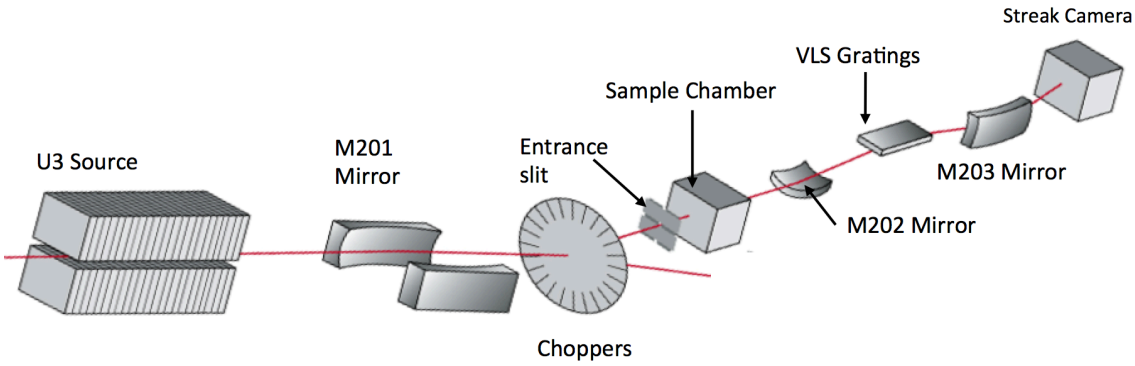

Fig. 2.5 Beamline schematic.

A schematic of the X-ray beamline is shown above in figures 2.4 and 2.5. The electrons in the storage ring pass through an in-vacuum insertion device with an undulator period, λ_u, of 30 mm. Within the undulator, the electrons undergo simple harmonic motion in their rest frame and emit dipole radiation. Radiation is produced at harmonics of the electrons' oscillation period, and the peak X-ray wavelength, as seen in the rest frame, is given by equation 2.2. The effective photon energy range of the 6.02 undulator is ~250 eV-1.5 keV. The undulator consists of permanent magnets separated by the undulator gap. The effective field strength (B_o in equation 2.2) can be changed by varying the magnet separation, undulator gap, to produce the desired peak photon energy, λ_x. A typical undulator spectrum is shown in figure 2.6.

$$\lambda_x = \frac{\lambda_u}{2\gamma}\left(1 + \frac{K^2}{2} + \gamma^2\theta\right), K \equiv \frac{eB_o\lambda_u}{2\pi m_e c} \tag{2.1}$$

Here γ is the Lorentz factor, e is the electron charge, m_e is the electron mass, θ is the emission angle, and K is the undulator strength parameter.

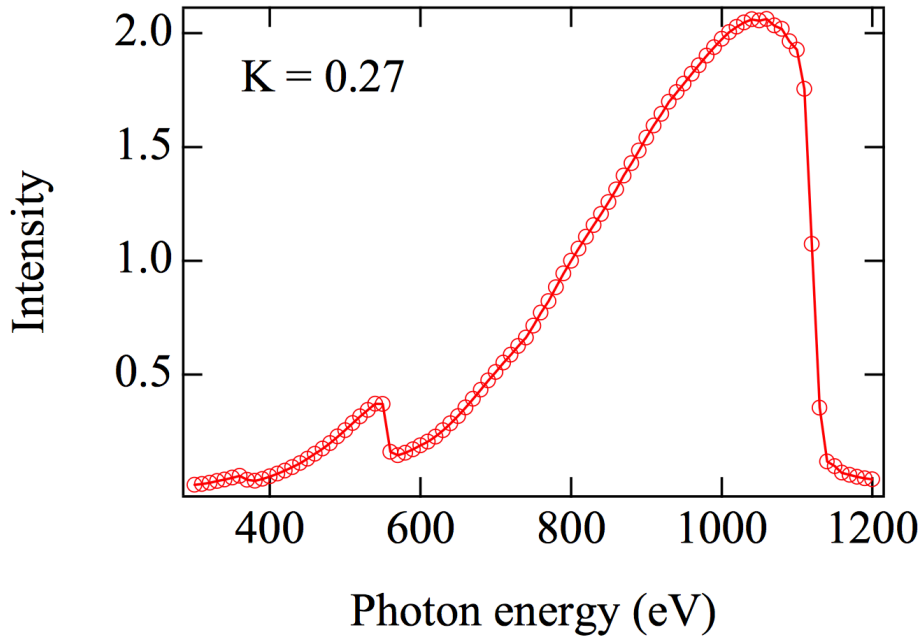

Fig. 2.6 Undulator spectrum. This is a typical spectrum produced by beamline 6.02 with K=0.27. From [56].

Fig. 2.7 In-vacuum undulator. Image courtesy of ALS, Berkeley Lab.

The polychromatic x-ray beam reflects from a toroidal mirror (M201), which produces a 1:1 image of the undulator source at the entrance slits. The toroidal mirror has a grazing incidence angle of 1.35 degrees. The dimensions of the image at the entrance slits (FWHM) is ~80 μm vertically and ~500 μm horizontally. The entrance slits consist of four movable tungsten knife-blades that can be used to reduce the x-ray spot size at the target.

The repetition rate of the x-ray beam is reduced by the chopper, which is immediately upstream of the entrance slits. The chopper is a free-running, water cooled, and slotted aluminum disk that spins at high speed. The slots pass x-rays at a frequency of 4 kHz with an opening time of 8 μs. This reduces the repetition rate and total x-ray flux by 97%. The total x-ray power is typically ~100 W before the chopper and ~ 3 W after the chopper. A fast (1 ms) solenoid driven shutter is placed directly downstream of the entrance slit and provides additional gating. The shutter passes as few as four chopper openings and reduces the x-ray dose downstream by 1000 to the μJ level. This shutter is selectively driven to facilitate a single shot acquisition mode.

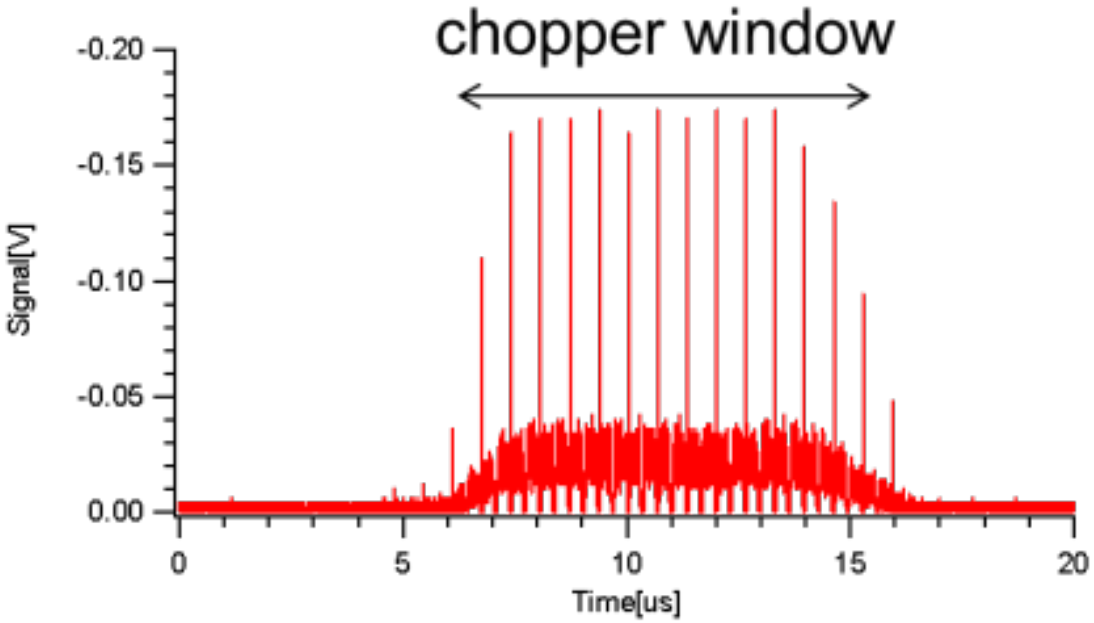

Fig. 2.8 Chopper window. Approximately 12 round trips from the storage ring (656 ns) pass through the 8 μs chopper opening. From [57].

The sample is mounted in transmission on a 3-axis manipulator. The transmitted x-rays are passed to the monochromator. The monochromator consists of a vertical focusing spherical mirror, M202, and varied-line-spacing (VLS) grating. This combination forms a spectral image at the detector. There are three different M202 mirrors that can be selected. The M202 mirrors set different deviation angles at the gratings, 86, 87 or 88 degrees, thereby shifting the peak grating efficiency to different photon energies. There are two gratings 250 and 1000 l/mm, which provide either higher efficiency and bandwidth or higher resolution. Finally, a plane elliptical mirror, M203, forms a 50 μm horizontal focus to couple as much light as possible into the streak camera slit. It is important to note that this experiment operates without a monochromator exit slit. This allows a range of photon energies to be diffracted in focus onto the detector. The bandwidth is determined by the grating used and the length of the streak camera slit.

2.3 Pseudo Single Bunch

The ALS has recently developed a method for isolating the camshaft bunch from the multi-bunch pulse train at variable repetition rates [57]. This is an incredibly useful for time resolved measurements that operate at a fraction of the ring repetition rate, as it allows for the use of integrating detectors and limits sample damage. The method for achieving bunch isolation is as follows. A pair of electrodes placed within the ring, stripline kicker (figure 2.9) , is driven by co-propagating plane wave voltage pulses. These 1 kV, 40 ns square pulses are generated are generated by DEI (Directed Energy Inc.) pulse generators. The electric field within kicker causes an angular deflection of the temporally isolated camshaft bunch. The deflection results in a sinusoidal orbit around the ring, and at each position along the ring the kicked bunches have a different vertical

position or a different angular trajectory. After two round trips the oscillation has a 180 degree phase shift, and another set of voltage pulses return the beam to its nominal trajectory (figure 2.10). This is referred to as "kick and cancel" pseudo-single-bunch [58].

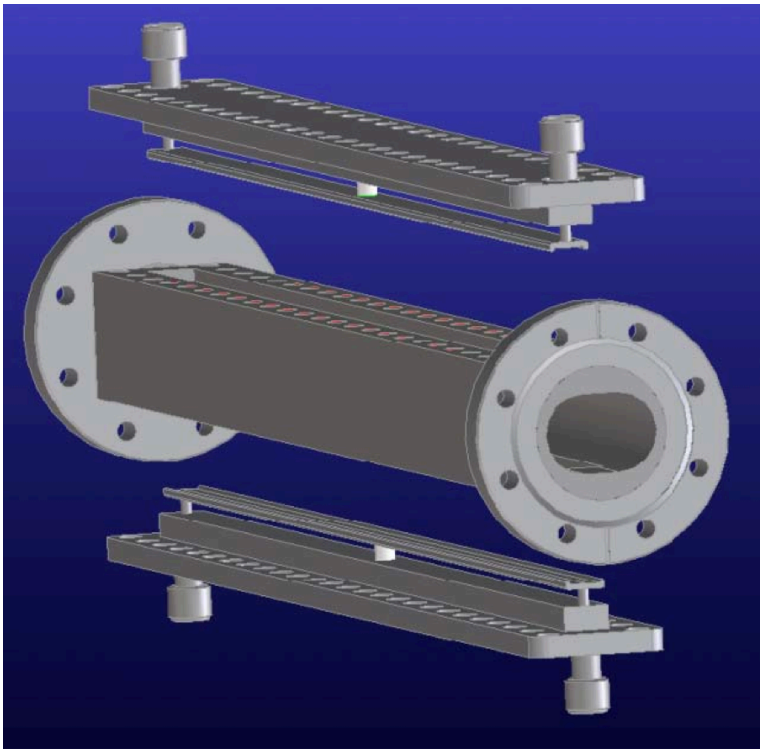

Fig. 2.9 Stripline Kicker. The kicker consists of two 0.6 m, 50 Ω transmission lines separated by 15 mm. From [59].

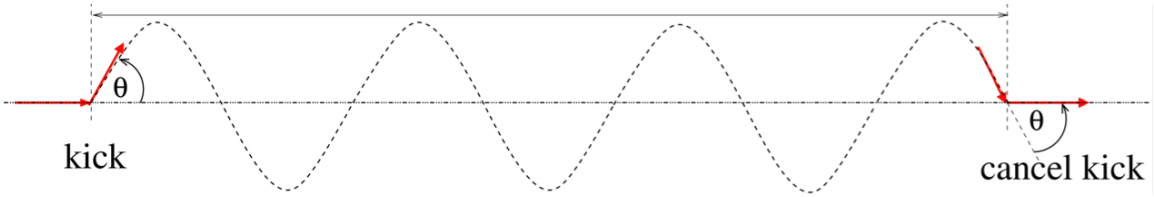

Fig. 2.10 Kick and Cancel Operation. Two identical kicks induce a sinusoidal orbit and cancel it after a 180 degree phase shift.

With the vertically displaced beam, a pair of slits is used to accept the kicked bunch and reject the un-kicked bunches, as shown in figure 2.11. A vertical deflection is chosen because the vertical beam size and divergence is smaller than the horizontal. This allows for greater suppression of the un-kicked pulses. PSB allows for a beamline to operate at variable repetition rate, from single-shot to 1.5 MHz (the maximum repetition rate of the pulse generators). However, because the un-kicked bunches greatly outnumber the kicked bunches and the vertical separation is only 180 μm (about twice the nominal beam width, 80 μm fwhm), the unkicked bunches still create background signal (figure 2.11). Experiments performed at beamline 6.02, using the chopper in combination with PSB operated at 4 kHz suppresses the unwanted pulses by ~7000.

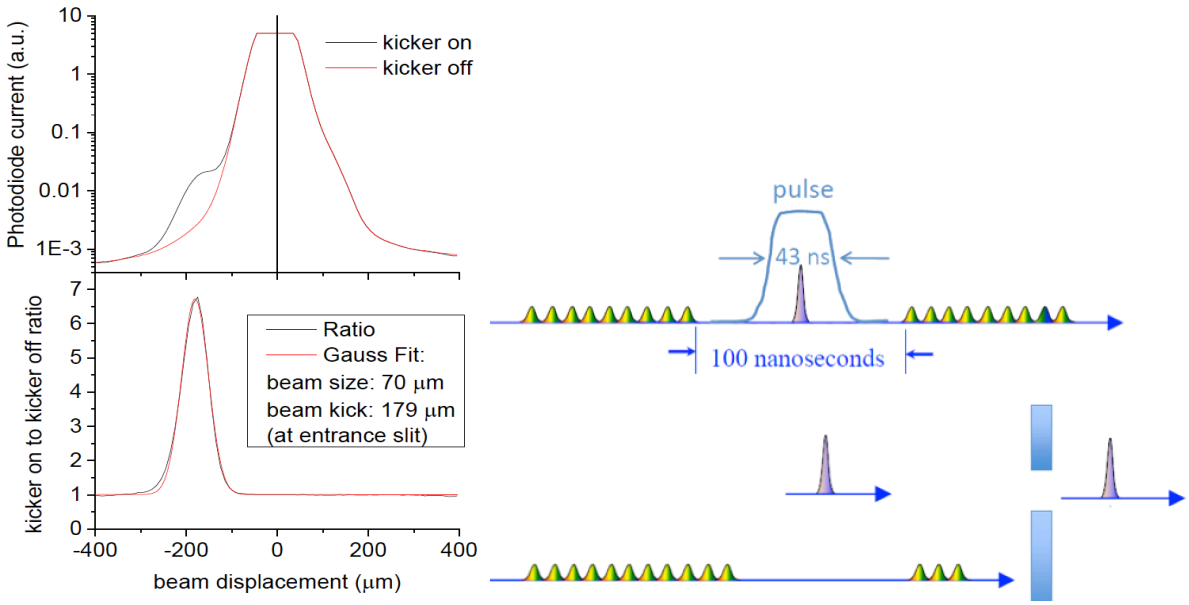

Fig. 2.11 Pseudo Single Bunch. The PSB mode provides a signal to background of 7:1 when operated at 4 kHz at BL 6.02 (right). A vertical displacement of the camshaft pulse allows it to be passed through a pair of slits that reject the multi-bunch pulses (right). Adapted from [58] and [57].

2.4 Laser System

A Ti:sapphire laser system is used to isochorically heat targets to a WDM state. A schematic of the laser system is shown is figure 2.12. The laser system consists of an oscillator, a regenerative amplifier, a 2-pass, and a 4-pass amplifier.

The oscillator is a mode-locked Coherent Vitara pumped by a 4.5 W continuous wave Coherent Verdi laser. The oscillator produces ~20 fs pulses with a center wavelength of 800 nm and a bandwidth of 40 nm. The total power output of the oscillator is ~400 mW. The oscillator has a nominal cavity length of 4.8 m and repetition rate of 62.5 MHz (16 ns period). However the oscillator has a variable cavity length, which synchronizes the optical pulses with the synchrotron pulses. Within the cavity, a flat end mirror is mounted directly to a piezoelectric crystal, which maintains the high frequency (~kHz) and fine (~ps) synchronization with the ALS pulses. The piezoelectric crystal has a limited range (~100 microns), so this cavity mirror also sits along a picomotor driven translation stage. This translation stage provides a rough adjustment to the cavity length and keeps the crystal centered within its range. These motors are incorporated in a feed-back loop that maintains a fixed phase between the oscillator pulses and the storage ring bunches. This is done by measuring the oscillator pulses with a fast diode. The diode signal is sent to a 500 MHz band-pass filter, isolating the 4th harmonic of the 16 ns oscillator pulse period. This signal is then amplified and mixed with the 500 MHz signal from the storage ring, which has passed through a phase shifter. This varies the relative phase between the two signals and gives control over the relative timing of the oscillator

and x-rays. The mixer outputs the difference frequency between the oscillator and storage ring and is used to drive a high voltage bias to the piezoelectric crystal, completing the feedback loop and phase locking the oscillator pulses to the x-ray pulses. Finally, the voltage on the piezoelectric crystal is monitored. When the crystal is near the end of it range the picomotor acts to compensate.

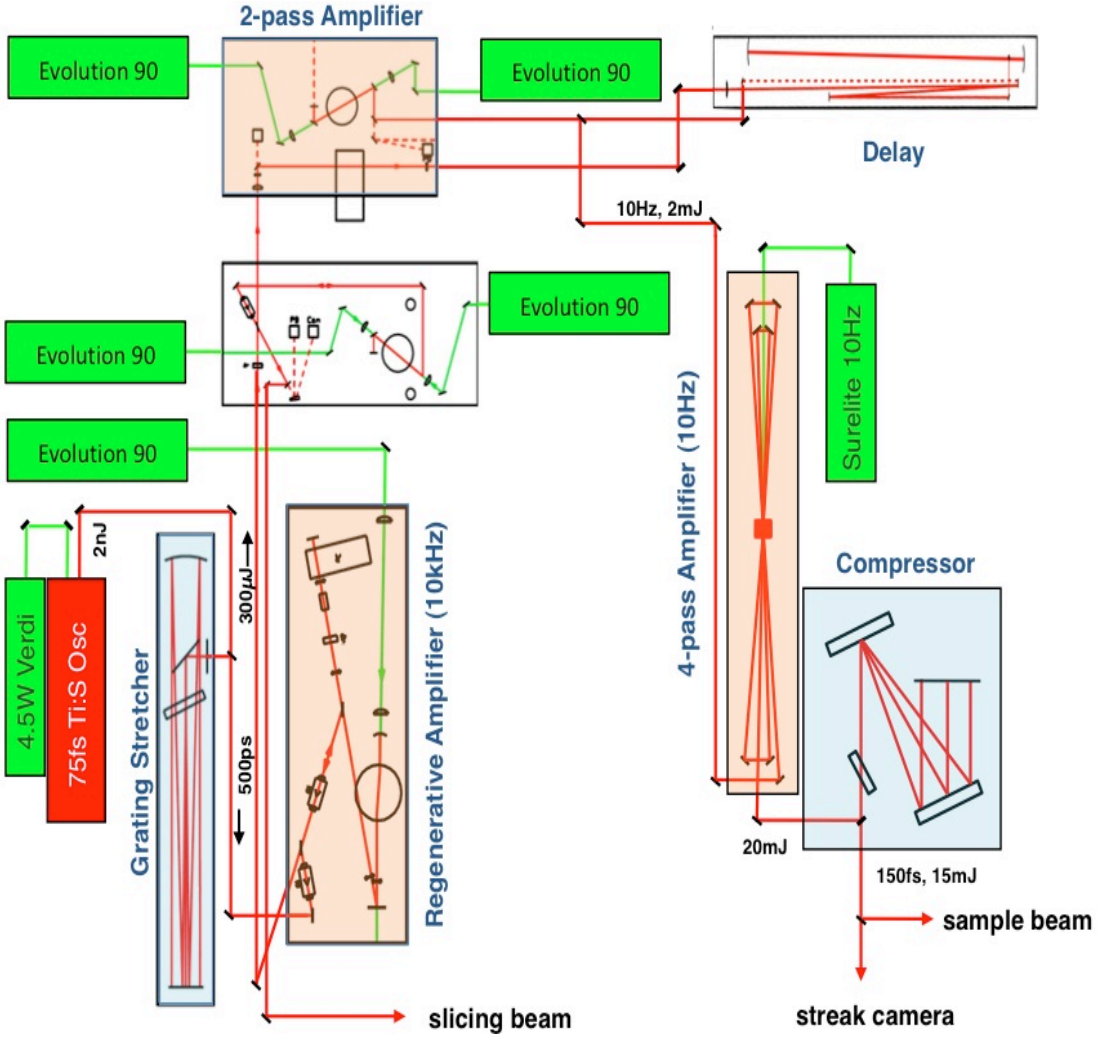

Fig. 2.12 Laser system schematic. The 800 nm beam path is displayed in red, and the pump laser beam paths are displayed in green.

In preparation for amplification, the phase-locked oscillator pulses (75 fs) are temporally stretched by a grating stretcher to 500 ps. These pulses enter a regenerative amplifier. The Ti:sapphire crystal is cryostat cooled and pumped by a Coherent Evolution 90 laser. It has an output pulse energy of 250 μJ. The input Pockels cell of the amplifier is synchronized to the free running chopper (4 kHz), to ensure that the amplified laser pulse is synchronous with center of the chopper opening. Another cryostat cooled 2-pass amplifier pumped by two Evolution 90s provides additional amplification to 2 mJ at 1 kHz. The last stage of amplification is provided by a 4-pass, 10 Hz amplifier pumped by a Continuum Surelite, which delivers a pulse energy of ~ 30

mJ. After 4-pass amplifier, the beam is temporally compressed by a grating compressor to a pulse duration of 150 fs and energy of ~20 mJ. The laser is then split into two beams: a sample pump beam and a beam for driving the streak camera (covered in chapter 3). A summary of the laser parameters is given in table 2.3.

Beams	Pump Beam: 20 mJ (800 nm) or 4mJ (400 nm)
	Streak Camera Beam: 1.5 mJ (800 nm)
Duration	150 fs
Bandwidth	30 nm (FWHM)
Beam Diameter	1.5 cm
Rate	10Hz
Pre-pulse	10^{-3}

Table 2.2 Summary of the laser parameters.

The pump beam is transported upstream of the laser hutch to the sample chamber. It is focused by a 30 cm focal length lens mounted to a translation stage. The sample is put behind the focal plane, to provide a variable spot size of 200-500 μm at the sample with a grazing incidence angle of 80 degrees. An additional 30 cm focal length lens and a CCD are placed behind the sample and the beam is imaged at the sample plane for spot size measurement.

Overlap between the x-rays and laser are achieved in the following manner. The x-ray beamline is aligned. A pinhole is placed at the sample plane. The pinhole position is scanned and the transmitted x-ray intensity measured. Once the position of the x-rays in the sample chamber is determined, the laser illuminates the pinhole, and the x-ray position is recorded by the imaging system. The laser pointing is adjusted to overlapped with the pinhole position by using a motorized mirror mount immediately upstream of the focusing lens. This procedure is repeated periodically to account for pointing drift and assure that good laser-x-ray overlapped is maintained.

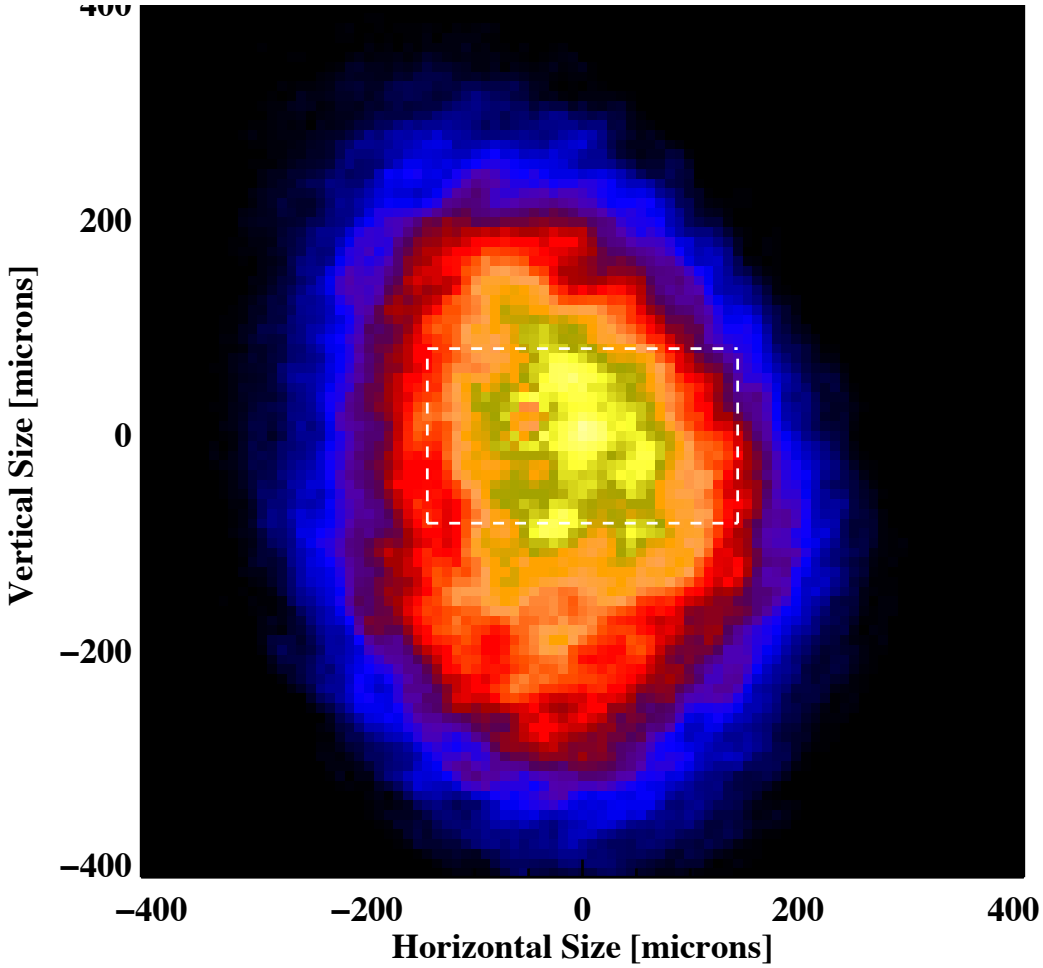

Fig. 2.13 Laser spot measurement. An example laser image 300 μm horizontally and 400 μm vertically (FWHM). The area sampled by the x-rays is shown within the dashed lines.

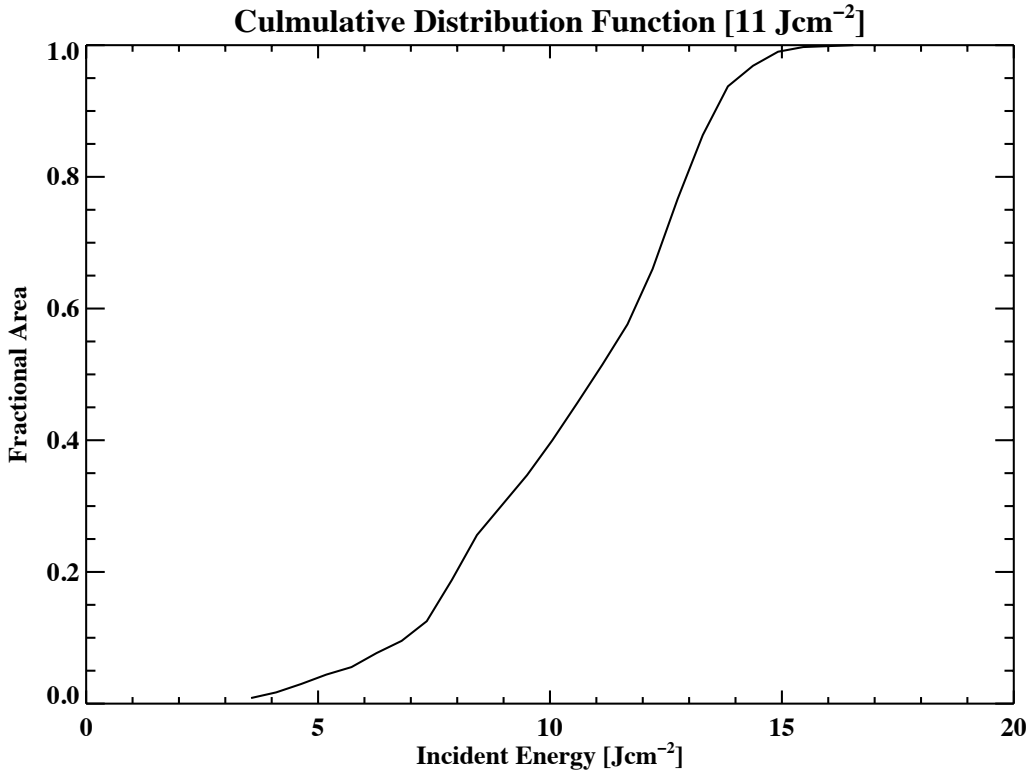

Fig. 2.14 Cumulative distribution function. The cumulative distribution function of sampled laser energy derived from figure 2.13.

The laser spot measurement and a measurement of the x-ray spot can be used to determine a weighted distribution of the sampled fluences. This is illustrated in figures 2.13 and 2.14.

It is also necessary to make an accurate determination of the laser energy deposition. This is achieved by measuring the sample's transmission and reflection of the pump laser pulse. This is illustrated schematically in figure 2.15. The procedure measuring reflection is as follows. An integrating sphere is placed directly upstream of the sample plane. A mirror is placed at the sample plane. The beam is attenuated for calibration. A diode upstream of the sphere records the incoming pulse energy, and the diodes on the surface of the sphere record the reflected pulse energy. The attenuation is then removed, and the reflection from the sample can be measured. In transmission, the process proceeds identically, except calibration is preformed with the laser pulse incident on the integrating sphere.

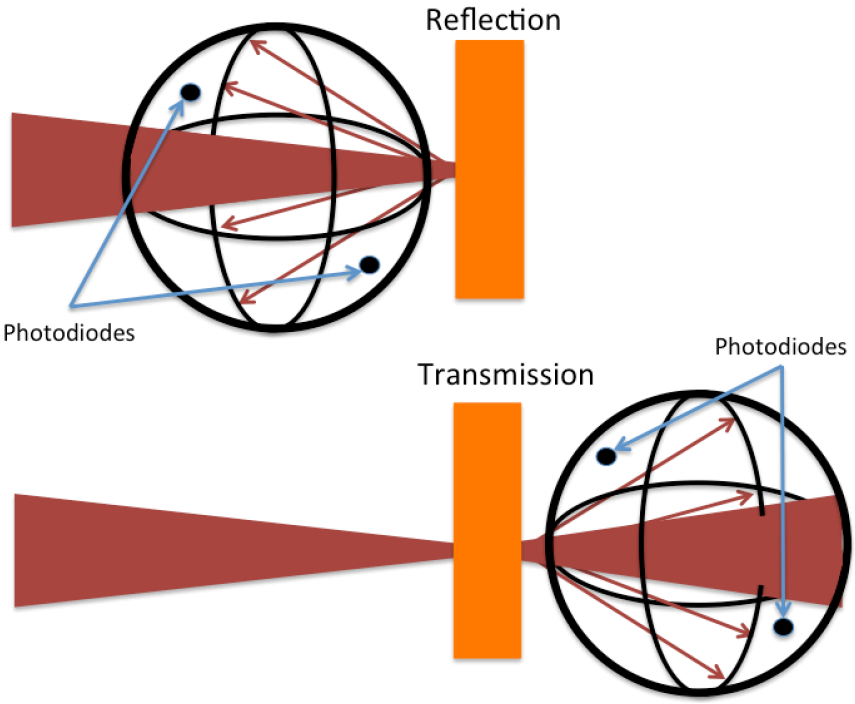

Fig. 2.15 Laser absorption measurement.

Chapter 3

X-ray Streak Camera

The intrinsic pulse duration of the ALS (70 ps) is longer than the time scales of hydrodynamic expansion, so an x-ray streak camera is used to provide ultrafast temporal information. Streak cameras operate by projecting the temporal (i.e. longitudinal) profile of a light pulse into transverse spatial information. The first streak cameras were mechanical and used a rotating mirror to project the light pulse directly onto a detector. First appearing in the 1960's and 1970's, optoelectronic streak cameras were developed. These cameras convert the light pulse to an electron pulse with a photocathode and use an electric field ramp to "streak" the electron pulse. These cameras had a temporal resolution of tens to hundreds of picoseconds [60,61]. Advances in photocathodes, deflector plates, and photoconductive switches has allow for the development of sub-picosecond streak cameras [62]. Modern streak cameras have the unique ability to simultaneously resolve sub-picosecond temporal and microscopic spatial phenomena [62,63]. This makes streak cameras a versatile diagnostic tool and ideal for studying the fast dynamics and transient states encountered in WDM experiments. X-ray streak cameras have been previously applied to study WDM at synchrotron facilities [64,65].

This chapter will cover the development of an x-ray streak camera and the integrated operation at the x-ray beamline. The new development of a grazing incidence streak camera that allows for more robust operation with increased efficiency [66] will be presented. Area detectors and gating methods will be discussed. Finally, temporal resolution and data analysis will be discussed.

3.1 Transmission Streak Camera

The x-ray streak camera consists of 5 primary components: a photocathode, a pair of sweep plates, a photoconductive switch, a solenoid lens, and an image detector. Most x-ray streak cameras use a transmission geometry. A schematic of the transmission streak camera developed at the ALS is shown in figure 3.1. The streak camera operates by projecting the temporal (i.e. longitudinal) information into transverse spatial information. X-rays are first transmitted through a horizontal slit of a photocathode, and produce secondary electron emission at the rear surface. These electrons are accelerated by across an anode mesh to keV energies. A pair of meander strip line plates is driven with an electric field ramp. This field deflects the electrons vertically, and the strength of the deflection is determined by the electron's time relative to the field ramp. Finally, a magnetic solenoid lens images the x-rays from the source point (photocathode) onto an area detector. The streak camera is housed in a vacuum chamber that at ~10^{-8} Torr, reduces electron scattering, keeps components clean, and prevents arcing in the high field region of the photocathode.

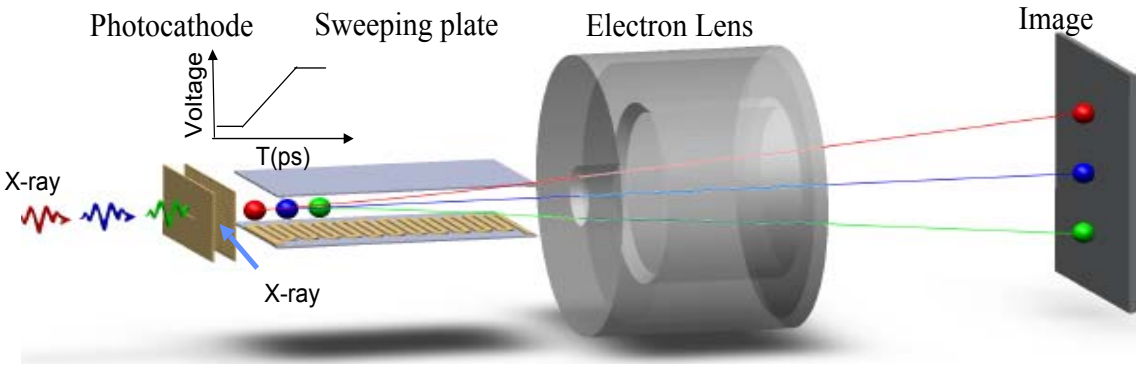

Fig. 3.1 Transmission streak camera schematic. X-rays are transmitted through a slit and generate photoelectrons at the rear surface of the photocathode (at high voltage). Extracted by an anode mesh (at ground), these electrons are swept by a voltage ramp propagating through deflection plates and imaged onto an area detector by a solenoid lens.

The transmission photocathode used is shown schematically in figure 3.2. It consists of a 300 μm silicon substrate with a thin, ~100nm, silicon nitride (Si_3N_4) layer, a 5 nm chromium binding layer, and ~10-30 nm gold cathode layer. The Si substrate is coated with Si_3N_4, and a slit is chemically etched with 44% KOH. The etching process terminates at the Si_3N_4 window and creates a tapered channel (110 degree opening angle) in the silicon wafer. The slit size is typically 10-100 μm in width and 3-6 mm in length, but the exact size of the slit is tailored to fit experimental constraints. A thin chromium binding layer and cathode layer are evaporated onto the Si_3N_4 surface. Typical cathode materials include gold or cesium iodide, and will be further discussed in the section 3.9. In this work, gold is chosen because of ease of handling and high tolerance to high x-ray flux.

The anode is a copper or gold electroformed mesh with rectangular openings. The mesh has a thickness of 2.5-5 μm, a wire width of 8.6 μm, and a hole width of 25 μm. The open area of the mesh is 55%. The mesh serves as a smooth equipotential surface, limiting non-uniformities in the electric field. This reduces the likelihood of arcing and image distortion, by creating a uniform and parallel accelerating electric field.

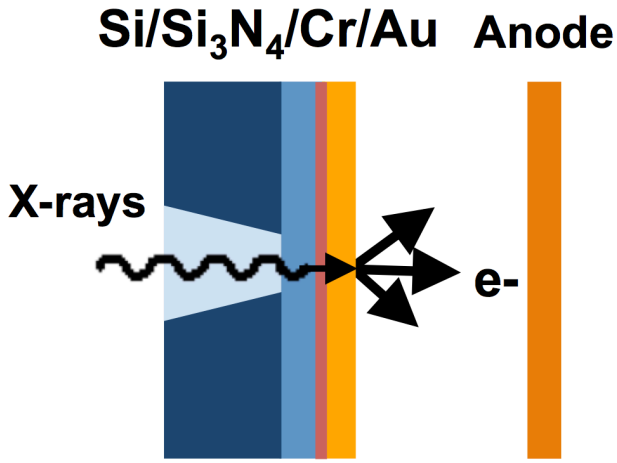

Fig. 3.2 Transmission photocathode schematic. A silicon substrate (dark blue, 300 μm), a silicon nitride window (light blue, 100 nm), a chromium binding layer (red, 5 nm), and a cathode layer (gold, 30 nm). The anode mesh is gold or copper (orange) and the gap is 1-2 mm.

The thickness of the cathode layer in this geometry is designed to match the escape depth of secondary electrons. The escape depth varies between materials but is typically ~10 nm [67]. The X-ray absorption length, however, can be much longer and is typically ~100 nm [49]. This mismatch limits the x-ray absorption that occurs within the electron escape depth and the quantum efficiency to <10%, for the transmission geometry. The thin cathode layer also presents a problem of robustness. Si_3N_4 is a ceramic, (10 times less thermally conductive then gold 30 and 314 $Wm^{-1}K^{-1}$, respectively [68]), and since the gold layer is thin (thickness to width ratio ~1:1000), the cathode has poor lateral conductivity. This limits heat dissipation under high intensity x-ray illumination. As a result, transmission photocathodes are susceptible to x-ray induced heating and damage. Transmission photocathodes were observed to suffer degradation after a 30 minute exposure to a 1 keV x-ray flux of $2x10^{12}$ photons/second/mm^2 [66]. This damage reduces overall efficiency as well as spatial and temporal resolution. An example of this can be seen in figure 3.3.

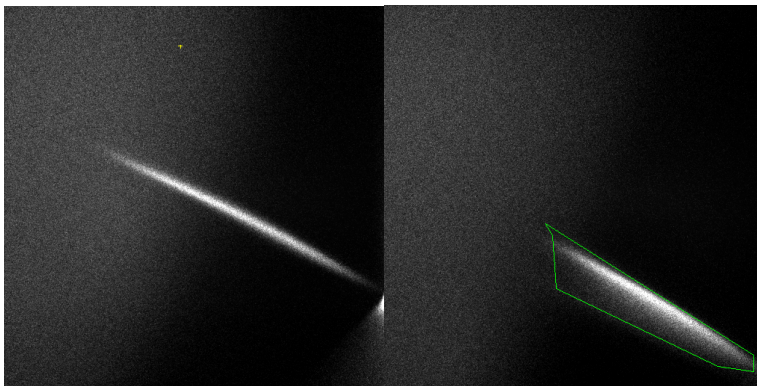

Fig. 3.3 X-ray induced photocathode damage. A streak camera image of swept, monochromatic x-rays taken before x-ray damage (left) and after x-ray damage caused by 10 minutes x-ray of exposure (right).

3.2 Grazing Incidence Streak Camera

The efficiency and robustness of the photocathode can be simultaneously improved by employing grazing incidence geometry. This is illustrated in figure 3.4. Grazing incidence decreases the absorption depth in the cathode by the cosecant of the grazing angle, thereby increasing the interaction region of x-ray absorption and electron escape depth. Since the x-rays are not transmitted through the cathode, it also allows for the use of a thick layer of photocathode material. This allows the heat load to be dissipated across the entire photocathode volume, thereby decreasing the local heating of the interaction region. In this case, the photocathode is a 10 mm thick silicon substrate coated with 600 nm of gold. In this geometry, the slit is 25-100 μm of tungsten, and it is place directly downstream of the anode mesh. The grazing incidence streak camera is shown in figure 3.5.

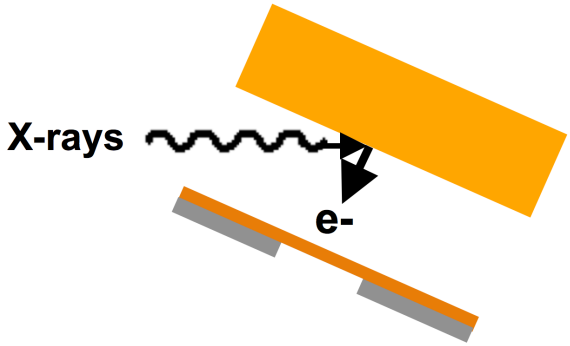

Fig. 3.4 Grazing incidence photocathode. In this geometry, x-rays arrive at grazing incidence, and a slit is placed behind the anode mesh.

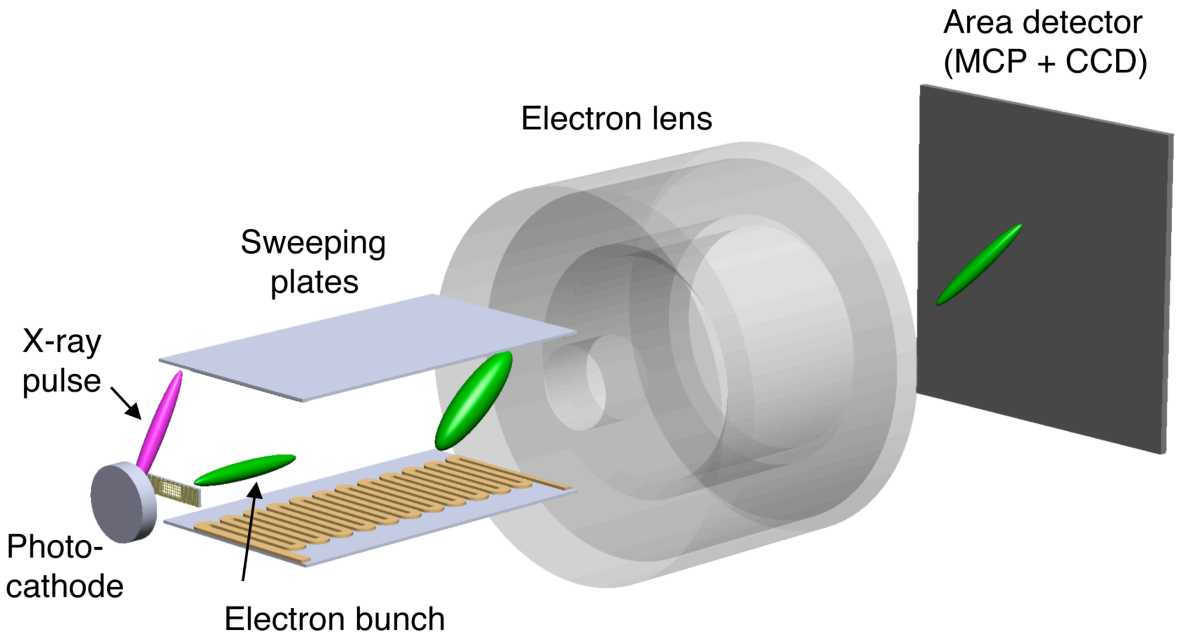

Fig. 3.5 Grazing incidence streak camera schematic.

The total electron yield is given by equation by [69],

$$Y = E_{ph} \cdot \varepsilon^{-1} \cdot \mu \cdot csc\,\alpha\,[1 - R(\alpha)]P_s(0)\int_0^T e^{-z(\mu \cdot \csc\alpha + L_s^{-1})}dz \qquad (3.1)$$

where Y is the total electron yield, E_{ph} is the is the x-ray energy, ε is the energy required to promote a single secondary electron from the valence band with sufficient kinetic energy to escape the sample, μ is the absorption coefficient, α is the grazing angle, $R(\alpha)$ is the Fresnel reflectivity, $P_s(0)$ is the electron escape probability at the surface, T is the cathode thickness, L_s is the secondary electron mean free path, and z is the vector normal to the cathode surface. This equation is used to calculate the electron yield as a function of grazing angle at various photon energies, as shown in figure 3.6. It can be seen that decreasing the grazing incidence angle increases the electron yield, until, at low grazing angle, the x-rays begin to reflect from the cathode surface. It is also apparent that grazing incidence can greatly improve streak camera efficiency in the hard x-ray energy range, where transmission streak camera measurements are very difficult. However, decreasing the grazing angle also increases the x-ray footprint on the photocathode, which decreases the transmission through a fixed anode slit width. The grazing angle also reduces the temporal resolution (discussed in section 3.9). A grazing angle of 20 degrees was chosen as a compromise.

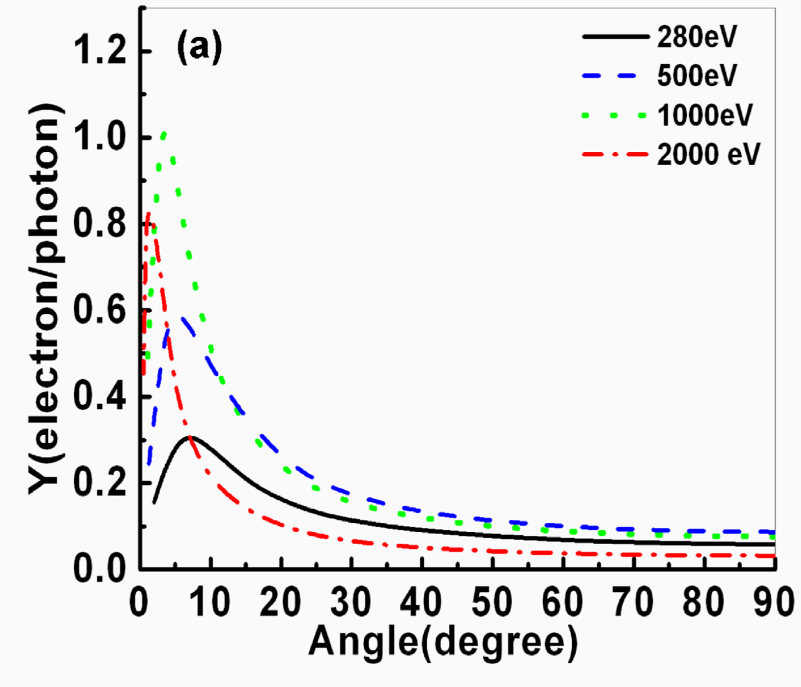

Fig. 3.6 Grazing incidence electron yield. The calculated electron yield vs. incidence angle from a gold photocathode excited by 280 eV, 500 eV, 1000 eV and 2000 eV photons [66].

3.3 Solenoid Lens

In order to resolve spatial information at the photocathode and achieve the best temporal resolution, the photocathode surface and slit are imaged onto an area detector. This is achieved with an asymmetrical solenoid lens. The lens is made of magnetic steel and houses a solenoid coil. A current is driven through the coils generating an axial magnetic field that focuses the electron beam. A schematic of the lens is shown in figure 3.7. The asymmetric shape of the lens reduces the magnetic field in the region of the sweep plates. The focal length of the lens is given by equation 3.2. The lens also induces a rotation in the electron beam and this is given by equation 3.3.

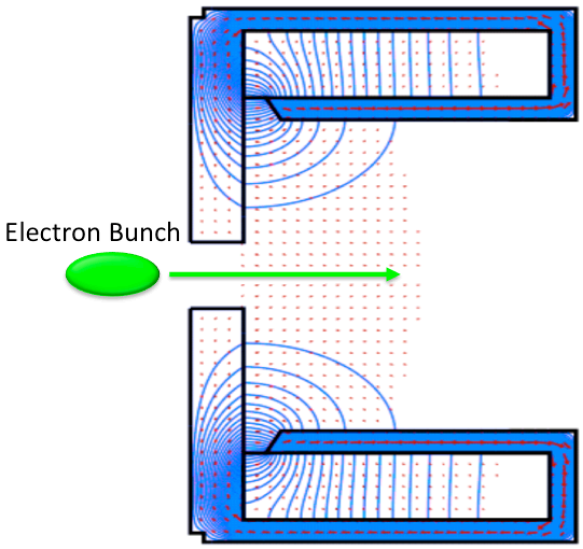

Fig. 3.7 Solenoid lens. A diagram of the solenoid lens showing the magnetic field lines as calculated by the Poisson Superfish code [70].

$$\frac{1}{f} = \frac{e}{8mV}\int_{-\infty}^{\infty} B_z^2(r,z)dz \tag{3.2}$$

$$\theta = \sqrt{\frac{e}{8mV}}\int_{-\infty}^{\infty} B_z(r,z)dz \tag{3.3}$$

This lens was designed to have a large opening aperture (20 mm), using the COSY [71] particle tracking code to reduce aberrations. A measurement of the magnetic field is shown in figure 3.8. Since the focal length and image rotation depend on the integrated axial field strength (equation 3.2 and 3.3), care was taken to ensure that the integrated field is approximately constant over that lens aperture. This can be seen in figure 3.8. However, at large radii the spatial resolution of the lens will decrease, and the lens will impart curvature in the image. This must be considered when analyzing streak camera images, and is discussed further in section 3.11.

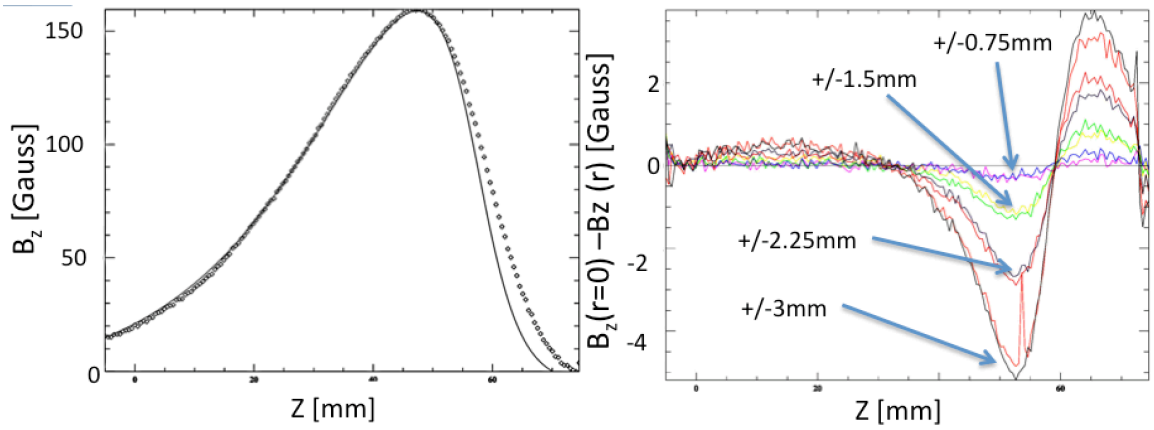

Fig. 3.8 Solenoid lens field. The axial field strength along the length of the lens (left) and the deviation of the axial field strength as a function of radial distance from the optical axis (right).

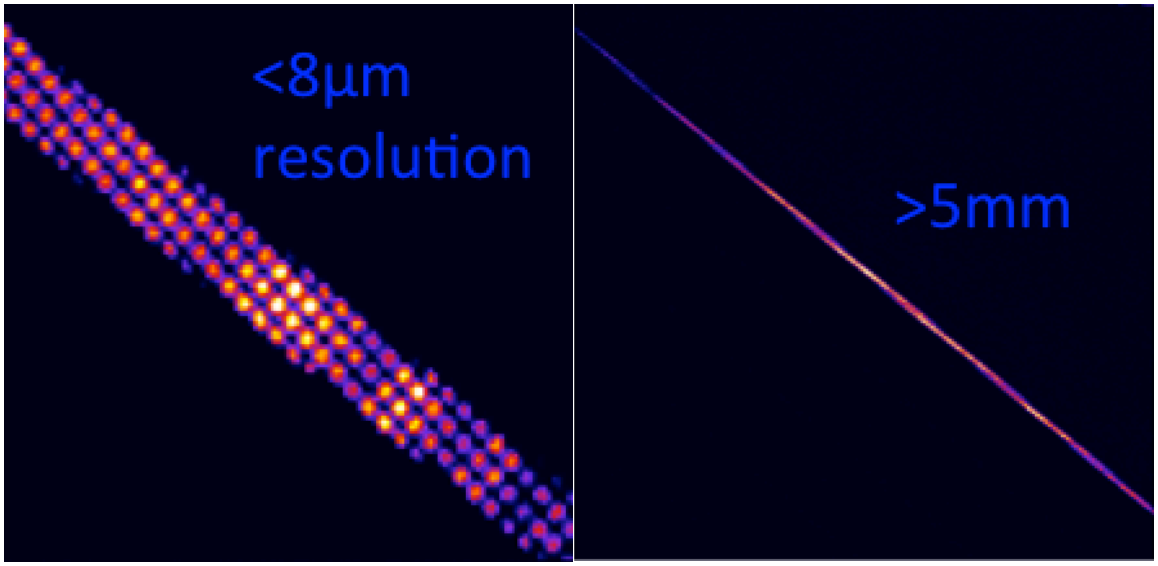

Fig. 3.9 Solenoid lens imaging. The solenoid lens produces an image with <8 µm resolution that is mostly free from curvature over a large length.

3.4 Gallium Arsenide Photoconductive Switch

The temporal information of the streak camera is achieved by deflecting the electron beam with a pair of sweep plates. The deflecting field is fast voltage ramp generated by a photoconductive Gallium Arsenide switch, which is triggered by a portion of the 800 nm laser. A well designed photoconductive switch produces a fast voltage ramp, requires little laser energy for switching, and has a long operating life time.

The switch is made by forming contacts on a 300 µm thick GaAs substrate. A simple diagram of the switch is shown in figure 3.10. The contacts are deposited by e-beam evaporation (20 nm Ni/ 20 nm Ge/ 150 nm Au). The laser penetration depth of 800 nm light in GaAs is ~750 nm [72]. To increase the depth of the contact regions the contacts

are flash annealed at 450 °C for 30 seconds after deposition. Germanium and gallium arsenide from a low temperature eutectic, and a liquid mixture of gold and germanium dissolves into the GaAs layer during annealing. This forms a highly doped region of the GaAs and creates ohmic contacts. A SIMS analysis (figure 3.12) indicates that eutectic penetration is about 200 nm. This allow reduces charge crowding at the edges of the gold contacts [73], as can be seen in figure 3.11. The switches are coated with a protective SiO_2 layer (100 nm) and then wire bonded onto an integrated circuit board.

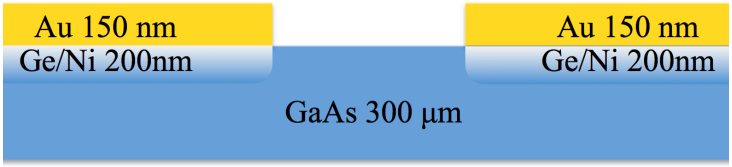

Fig. 3.10 GaAs switch schematic.

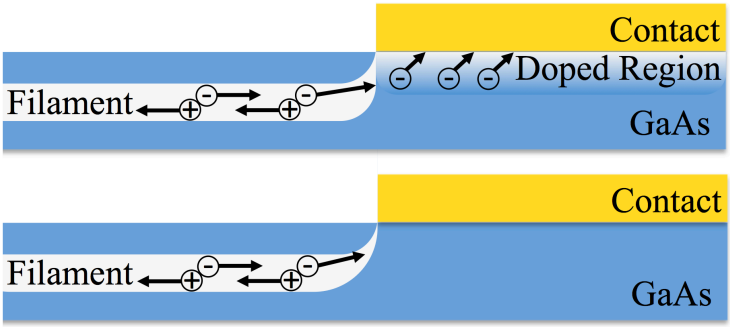

Fig. 3.11 Charge flow in the GaAs switch. An example of charge flow with and without doped contacts (top and bottom). Without ohmic contacts, current within the substrate is attracted to the edge of the gold contact, resulting in high current densities and potential damage.

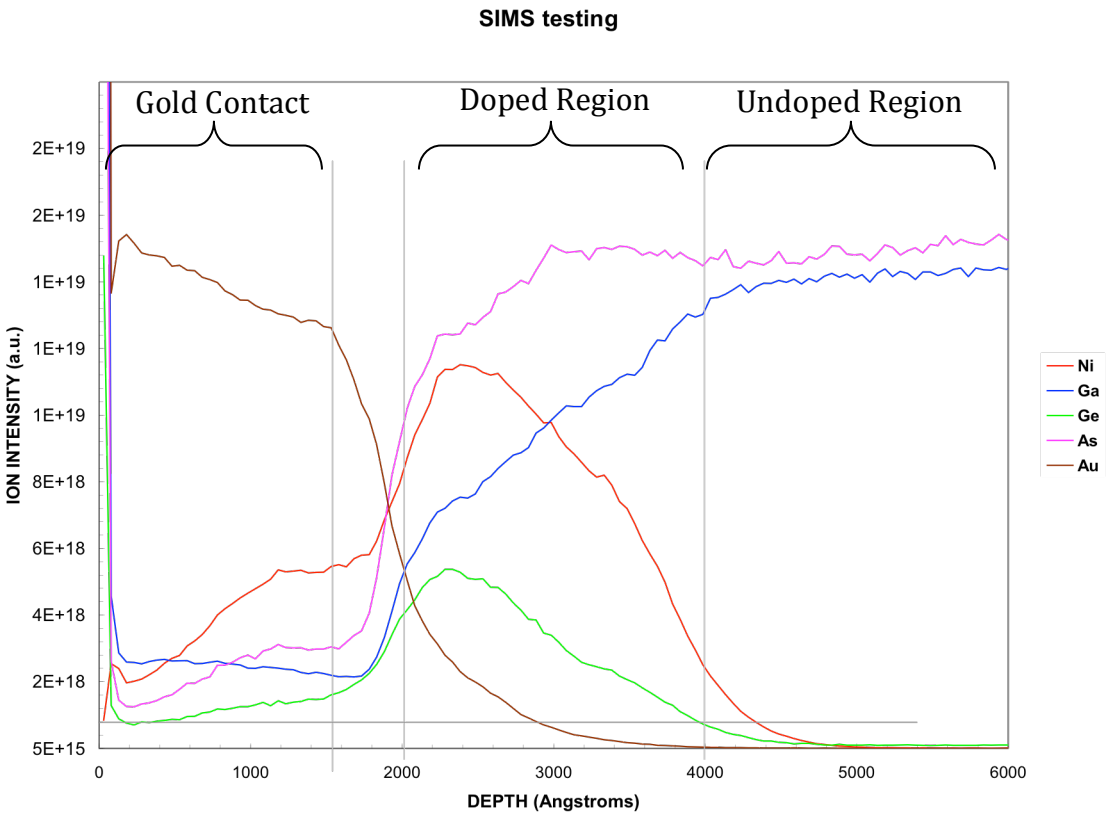

Fig. 3.12 SIMS analysis.

Several different geometries have been used, but in general the contacts are ~ 5 cm in length, 3mm in width, and a gap of 3 mm. The semi-insulating, undoped GaAs used has a dark resistivity of 10^8 Ω-cm, (carrier density, $n_c=1.8\cdot10^6$ cm^{-3}), and this results in a high open state resistance of the switch. The open state resistance is given by,

$$R_{open} = \frac{\rho_o \cdot l}{w \cdot t} \sim 10^{12}\ \Omega \tag{3.4}$$

where l is the switch length, w is the switch width, and t is the switch thickness. ρ_o is the resistivity of the semiconductor. The switch is operated with 500-1000 V bias between contacts and driven by an 800 nm laser pulse (50-500 μJ). This results in peak currents of up to 10 Amps. Since the penetration depth of the laser light exceeds the thickness of the contacts, the effective thickness of the switch is limited to the depth of the contacts. The band gap of GaAs is 1.4 eV, and the optical photons of the 800 nm laser (1.55 eV) possess sufficient energy to generate electron-hole pairs in the GaAs within the laser penetration depth. If the laser pulse duration is short compared to the carrier recombination time, then the initial carrier density after laser excitation can be expressed as,

$$n_o = \frac{E(1 - S_r)}{\varepsilon \cdot l \cdot w \cdot \delta} \tag{3.5}$$

where E is the laser energy, S_r is the reflection coefficient, ε is the photon energy, and δ is the laser absorption depth. After the laser excitation the carrier density will decay exponentially by electron-hole recombination,

$$n_c(t) = n_o \cdot e^{\frac{-t}{\tau}} \tag{3.6}$$

where τ is the carrier lifetime. In general, carrier lifetime differs between electrons and holes, so carrier decay can have multiple time constants. GaAs experiences carrier saturation at carrier densities above ~10^{20} cm^{-3} [11]. This provides a saturation mode and assures that the switching speed and efficiency are independent of laser energy fluctuation. This yields stable temporal dispersion and limits jitter in acquisition mode. This can be seen in figure 3.13. With a 60 μJ laser pulse and typical spot size equation 3.5 gives n_c=1x10^{20} cm^{-3}. The time jitter is measured to be a maximum of 60 fs at an average laser energy of 60 μJ with 1.5% energy fluctuation (fwhm), which is small compared to other resolution elements (see section **3.9**).

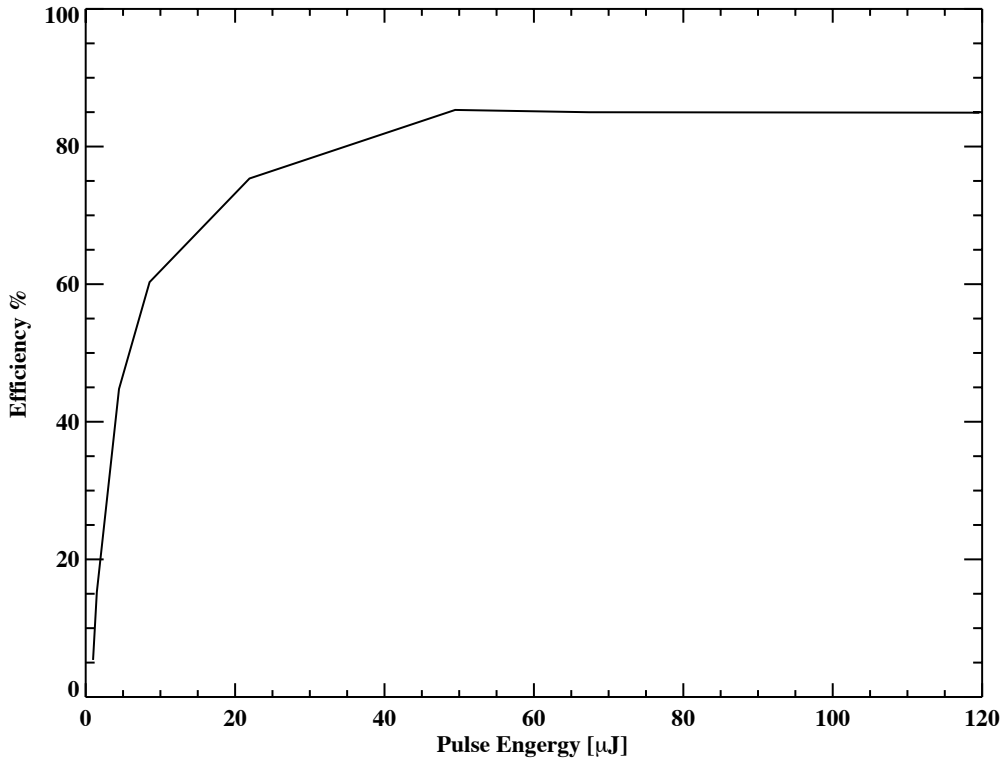

Fig. 3.13 Switch Saturation. Output efficiency (output voltage/input voltage) of GaAs switch as a function of input laser pulse energy (at 1 kHz) with 200V applied.

These carriers allow the switch to conduct current, and the closed state resistance can then be written as,

$$R_{closed} = \frac{l}{\sigma_s \cdot w \cdot h} \tag{3.7}$$

where h is the effective depth of the switch. The closed state conductivity, σ_s, can be expresed as,

$$\sigma_s = n_c \cdot \mu_c \cdot e \tag{3.8}$$

where n_c is the carier denisty, and the carrier mobility, μ_c, is the sum of electron and hole mobility. Calculting the closed state resistance using the equations 3.7and 3.8 gives 0.6 Ω.

The field applied across the switch is 1.5-3.5 kV/cm, this keeps the switch in the linear regime and below the lock-on or avalanche regime of GaAs (4-8 kV/cm) [74]. Lock-on mode reduces the required laser energy and decreases jitter. However, the gain achieved in the avalanche process results in strong current filamentation and is destructive to the GaAs substrate. Lock-on mode also requires the use of a pulsed voltage source. For these reasons a linear mode was chosen.

Parameter	E_{gap} (eV)	δ@800 nm (nm)	ρ_o (Ω-cm)	μ_e ($cm^2 V^{-1}s^{-1}$)	μ_h ($cm^2 V^{-1}s^{-1}$)	τ_e (ns)	τ_h (ns)	S_r
GaAs	1.4	743	10^8	8500	400	10	10	0.33

Table 3.1 GaAs properties. A summary of relevant GaAs values [72,74,75].

The switch is connected to a standard circuit board is shown below in figure 3.14, with the circuit schematic shown in figure 3.15. The switch operates as two identical circuits. Each is driven by an equal and opposite bias voltage (V_s). This reduces the total voltage to ground on the circuit components and cables and reduces the likelihood of arc damage. A set of resistors (R_s) prevent the voltage pulse from traveling into the power supplies. A capacitor (C_s) is used to block the DC voltage from the sweep plates. The circuit board is impedance matched to 50 Ω, 30 GHz Pasternack SMA cables that pass through the vacuum chamber to the sweep plates. These are also designed to be impedance matched at 50 Ω . Additional SMA cables carry the pulse out of the vacuum chamber where it is terminated (R_L). To ensure that the electrons in the streak camera remain centered on the optic axis, the center of the voltage ramp must be biased to 0 V. Two additional DC power supplies are used for this (V_b). A final capacitor blocks the DC current from this DC bias before 50 Ω termination.

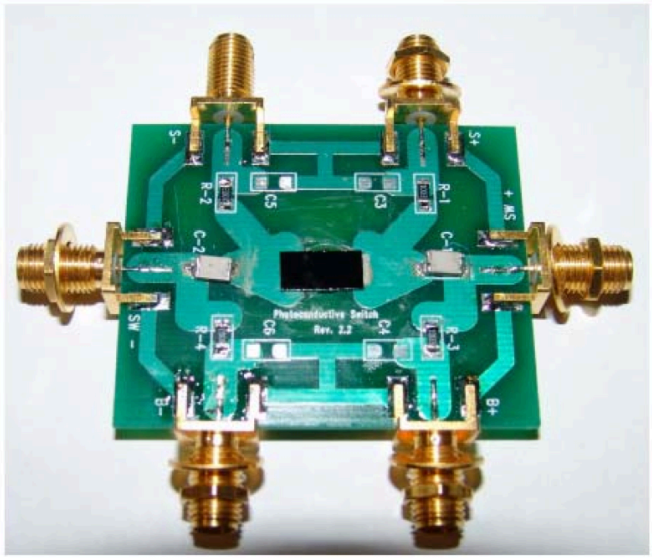

Fig. 3.14 Switch circuit board.

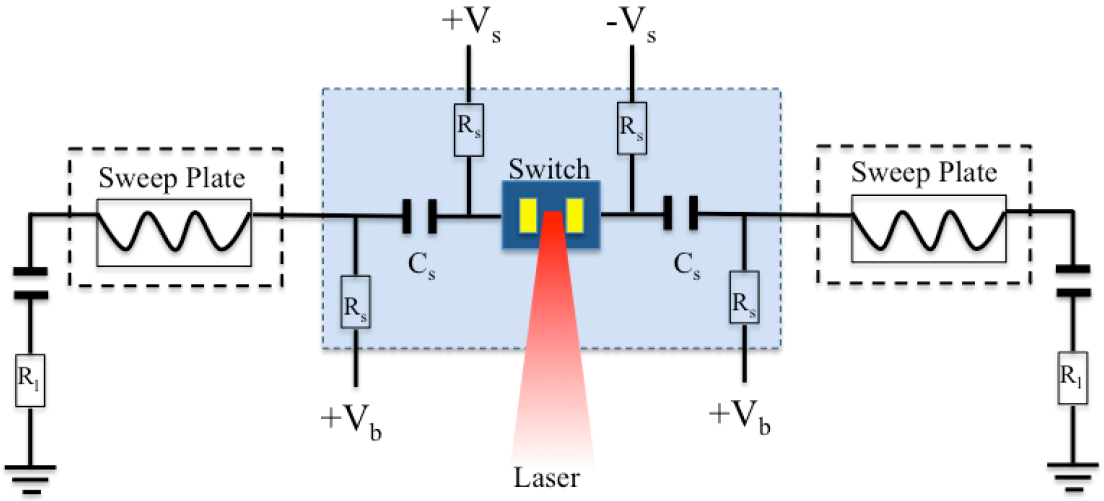

Fig. 3.15 Switch schematic. The switch is shown in dark blue, the circuit board is shown in light blue, and the sweep plates are enclosed within a vacuum chamber (dashed lines).

Figure 3.16 shows a measured high voltage ramp from the switch. The switching of the GaAs is fast <100 ps, but the overall rise time at the sweep plates is limited by the inductive and capacitive loads of the system (primarily the cables and sweep plates). For this reason, the cables must be kept short. The output of the switch generates a traveling wave with a rise time of 180 ps (10%-90%) and an efficiency of 80% percent of the input voltage. This provides a linear region of ~100 ps, which provides a constant sweep speed for the 70 ps x-ray pulse.

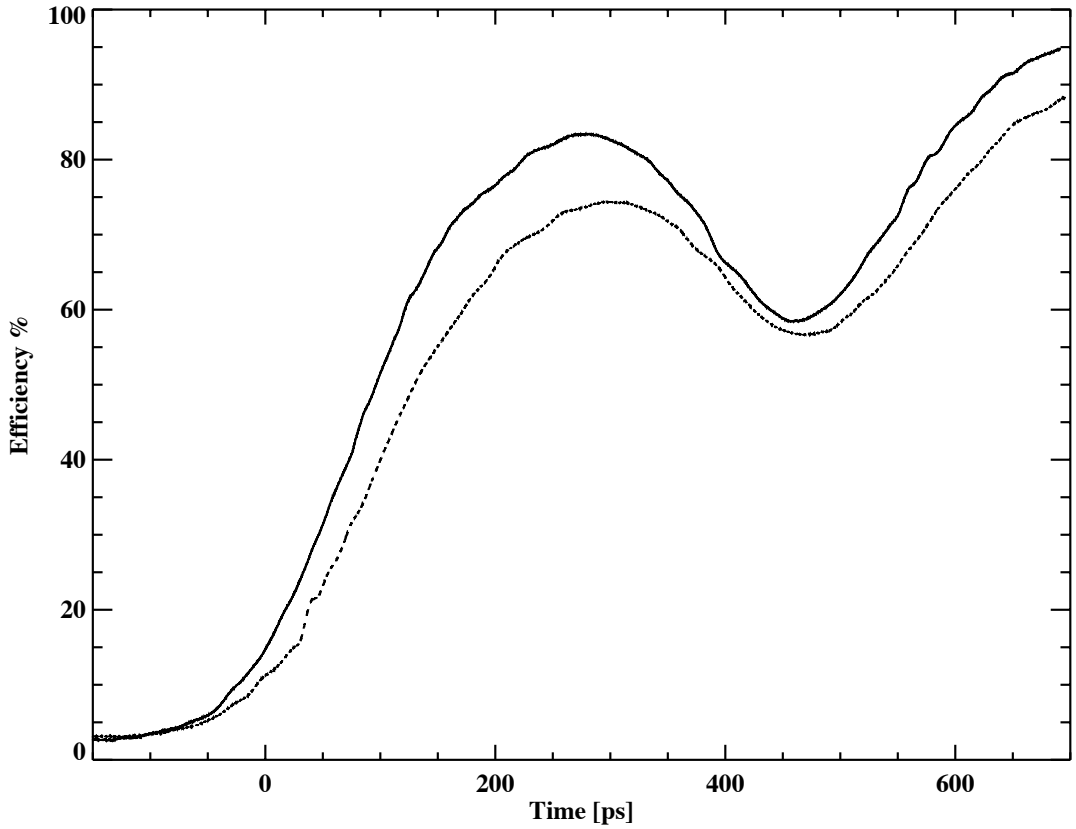

Fig. 3.16 Switch output. The output of the GaAs switch after exiting the streak camera chamber (solid), and after the addition of 13ft of SMA cable (dashed), which shows a decrease in switch speed and efficiency.

3.5 Sweep Plates

The deflection of the electron beam is produced by a pair of parallel sweep plates. The sweep plates consist of a copper microstrip meander line that is lithographed onto a circuit board. The sweep plates are 60 mm in length, 40 mm in width, are separated by a distance of 3-4mm, and are shown in figure 3.17. The separation is chosen to be as small as possible without interfering with the electron beam path. The small separation maximizes the electric field and sweep speed. The meandering path is designed maximize the deflection of the electron beam by matching the propagation speed of the voltage ramp to the velocity of the electron beam. The width of the meander line and thickness of the dielectric substrate are chosen to provide an impedance of 50 Ω . The propagation speed of the voltage ramp is approximately 0.66 *c*, whereas the electron beam has a speed of 0.2 *c*. The slits in the circuit board reduce the cross-talk between adjacent lengths of the meander line as the high voltage pulses travel along the plate.

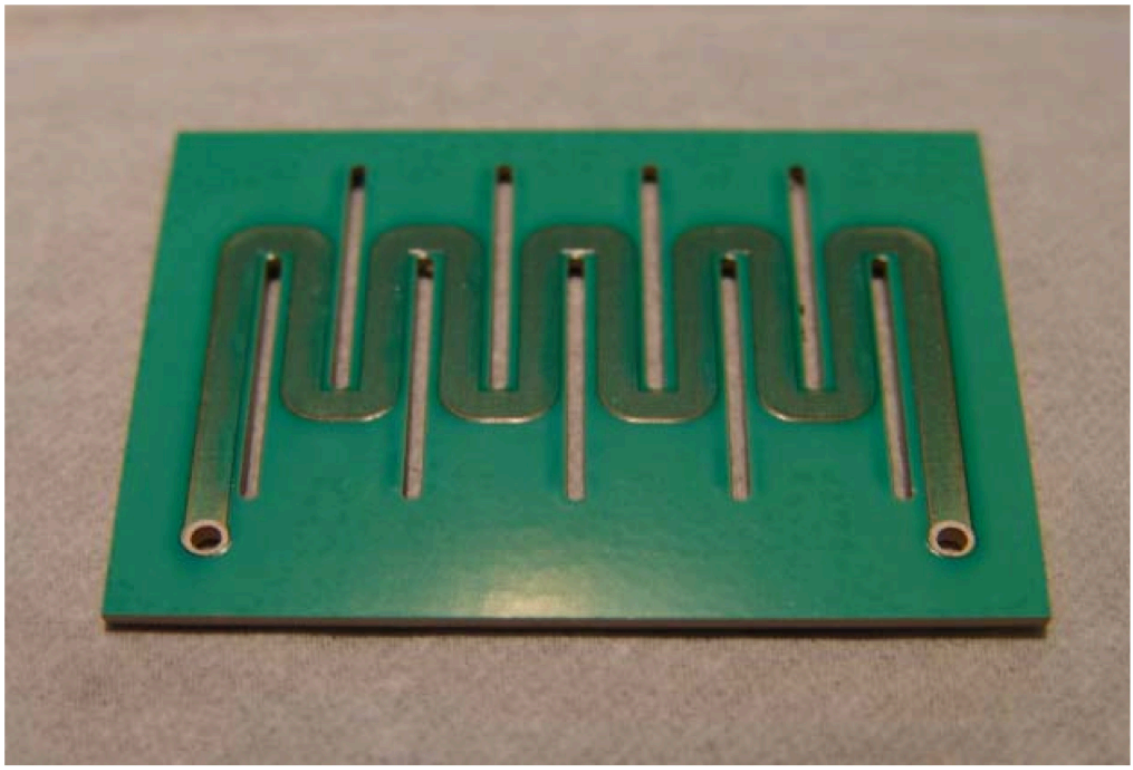

Fig. 3.17 Meander sweep plate.

3.6 Background

The sweep voltage provides some gating for the streak camera. The voltage ramp is biased so that the center of the ramp is at 0 V. This keeps the center of the synchronized electron bunch on the optical axis, as shown in figure 3.18. However, electrons that are not synchronized with the voltage ramp are deflected by the DC bias field. This deflection is large and moves the electrons off of the area detector. However, the sweep plates are separated by a small distance to maximize the sweep speed of the camera and improve temporal resolution. So, many of the unsynchronized electrons hit the sweep plates and scatter (figure 3.18), and this generates background counts at the detector. The electron scatter can be minimized, but not eliminated, by carefully designing the streak camera geometry.

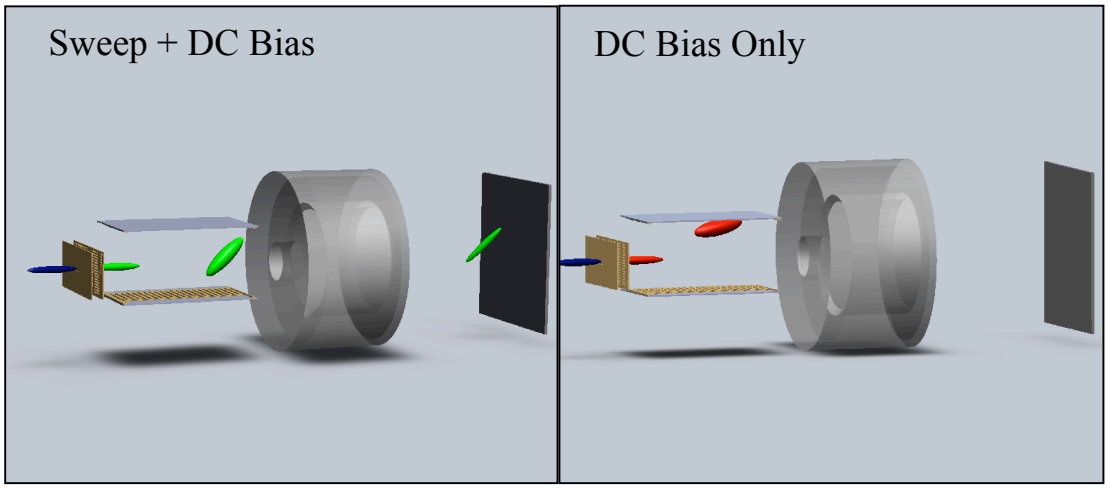

Fig. 3.18 Unswept electron scatter. An electron bunch synchronized with the voltage ramp is swept, but remains centered on the optical axis (left). An electron bunch that is not synchronized with the voltage ramp is deflected off the optical axis by the DC bias field and scatters off the sweep plates.

3.7 Area Detectors

The streak camera produces an image of the photocathode slit with a magnification of 2.5. This image is collected by an area detector. Two different detection schemes can be used depending on the background signal levels: a high resolution and nearly 100% efficient direct detection scheme, and a lower resolution and efficiency, gated detection scheme. As discussed in section 3.6 the streak camera provides some internal gating, but it may also require additional gating at the detector. In general, a gated detector is required during normal multi-bunch operation without PSB, but a gateless detector can be used in two-bunch operation or if PSB is used.

In the direct detection scheme, the 10 KeV electrons impact an in-vacuum, deep-cooled Andor IKon-M CCD. This is a 16-bit back-illuminated sensor with 1024 x 1024 pixels and a pixel size of 13.3 x 13.3 μm. A single 10 KeV electron produces ~2000 electron hole pairs. While this limits the dynamic range (100,000 electrons in a pixel well depth), at -40 C the readout noise is limited to a ~7 electrons per pixel. This allows for nearly noiseless detection. The response of the Andor CCD is shown in figures 3.19 and 3.20. The pixel limited resolution for this scheme is ~5 μm at the photocathode.

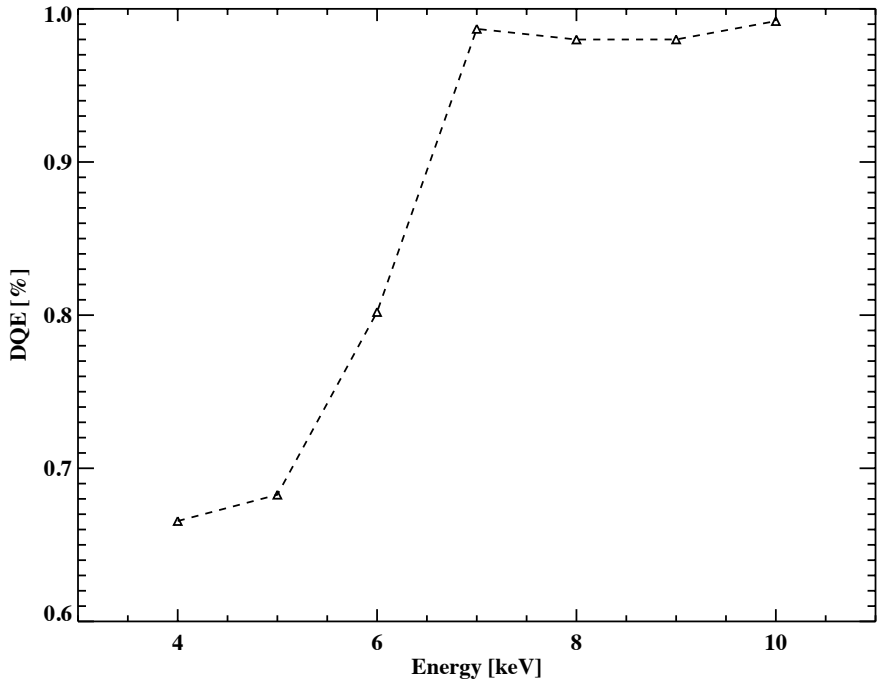

Fig. 3.19 Andor CCD detected quantum efficiency. The Andor CCD shows near perfect DQE above 7 keV.

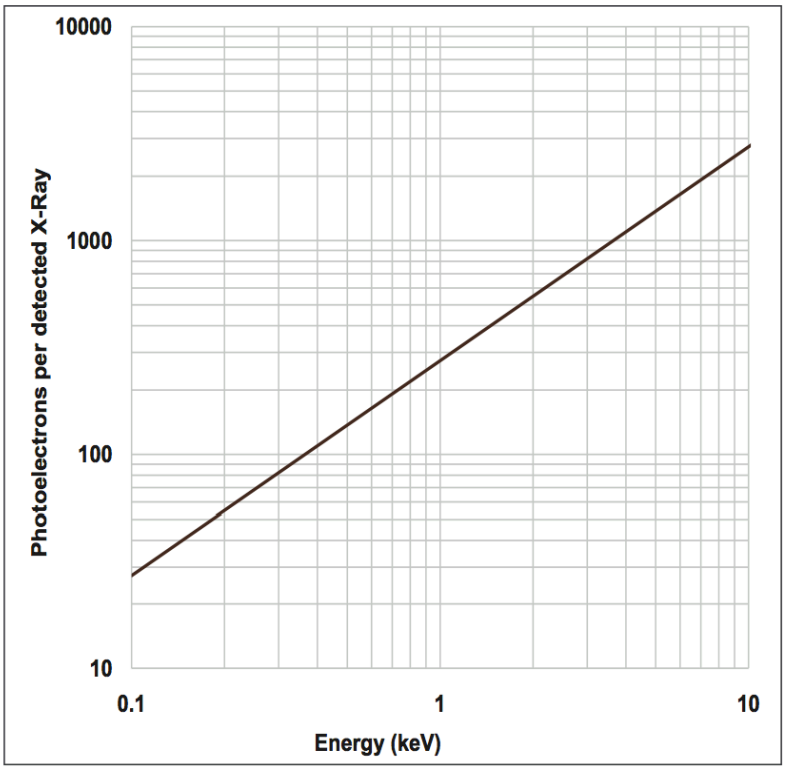

Fig. 3.20 Andor CCD photoelectrons per X-ray. High energy x-rays, or electrons in this case, create many photoelectrons within the CCD limiting dynamic range.

As discussed in chapter 2.2 the x-ray beamline utilizes several components to reduce the average x-ray flux and repetition rate. However, the background signal still dominates, so a gated detector must be utilized. The gated detector consist of a micro-channel plate (MCP) and phosphor screen which is fiber coupled to a Princeton CCD (1300x1340 pixels with a size of 20x20 μm) . This is illustrated by figure 3.21. The drawback of this scheme is that it has a lower detected quantum efficiency ~40% and a decreased spatial resolution. While the pore size of the MCP is comparable to the CCD pixels and the point spread function of the phosphor on the fiber is small (~35 μm), spreading of the electron cloud in the gap between MCP and phosphor screen causing a substantial decrease in resolution [76]. This is estimated to be ~150 μm, and limits the resolution at the photocathode to ~60 μm.

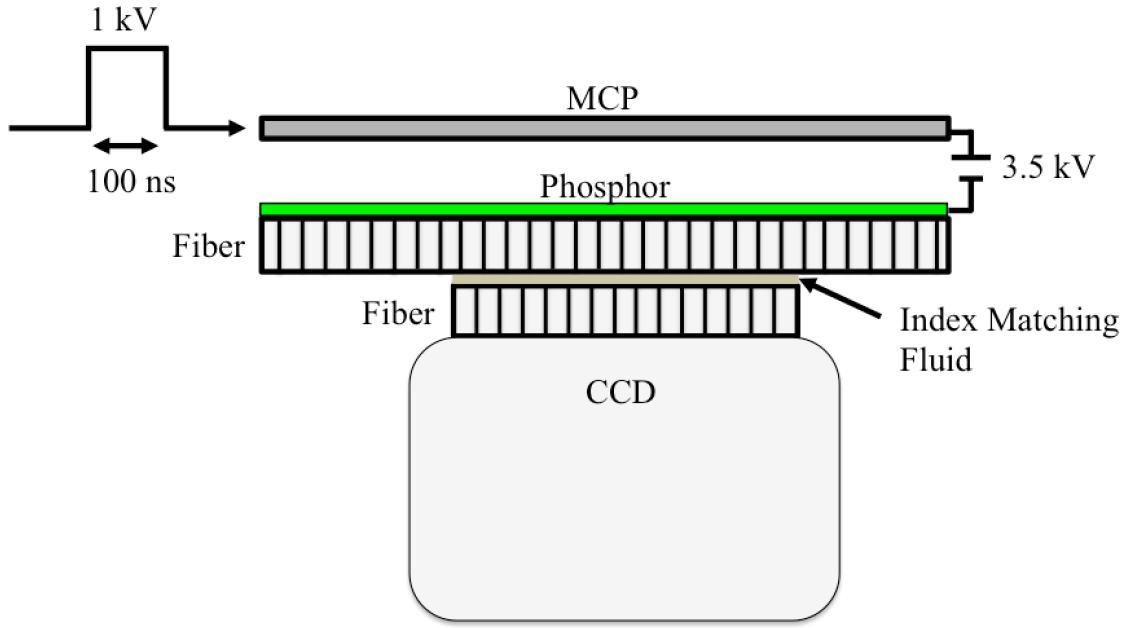

Fig. 3.21 MCP schematic. The MCP is gated by a 1 kV, ~100 ns voltage pulse. Electrons are extracted from the MCP and traverse a 3mm gap before exciting a phosphor screen. The phosphor luminescence is fiber coupled out of vacuum. A thin layer of index matching fluid minimize reflection losses and couples to a fiber coupled Princeton CCD.

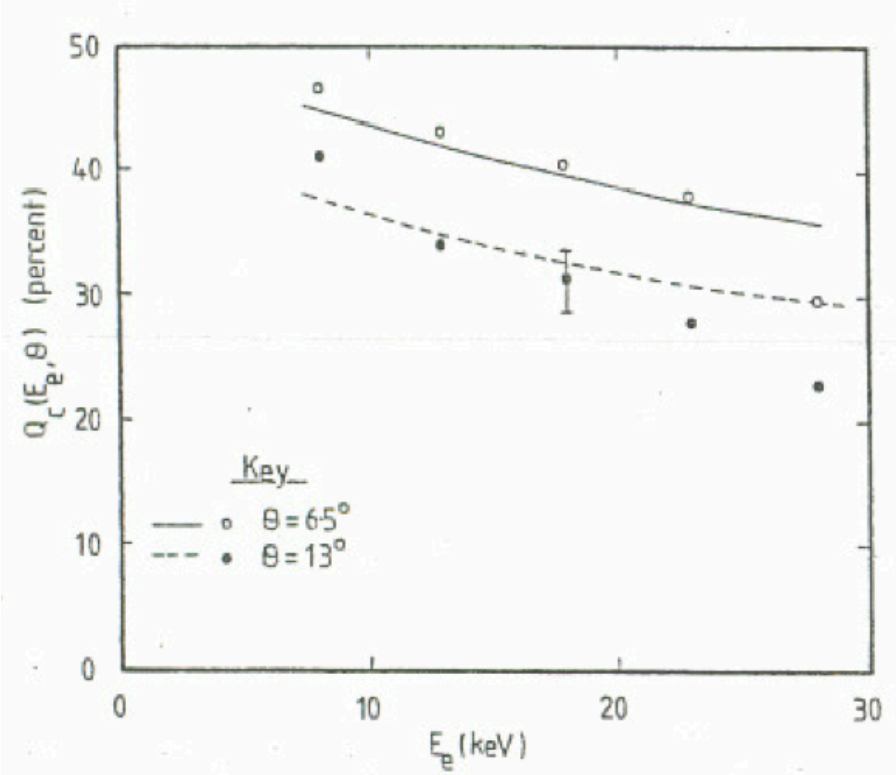

Fig. 3.22 Detection Quantum Efficiency of MCP. The detection quantum efficiency depends on the angle between the incident electron and MCP pores. Here curves for 6.5 degrees (solid) and 13 degrees (dashed) are shown [77].

3.8 UV Production

As illustrated above, the streak camera has many variable parameters including anode extraction and sweep voltage, and these parameters effect the temporal dispersion produced by the streak camera. In order to maintain a constant calibration of the temporal axis, two UV (266 nm) laser pulses are used as fiducials. The 266 nm pulses are the third harmonic of the 800 nm laser and are produced by second harmonic and sum frequency generation. While, the work function of oxidized poly-crystalline gold (4.2 eV) [67,78] is higher than the fundamental photon energy (1.55 eV) of the laser, the third harmonic has sufficient energy (4.66 eV) to generate photoelectrons in the gold cathode. The harmonic generation setup is shown in figure 3.23.

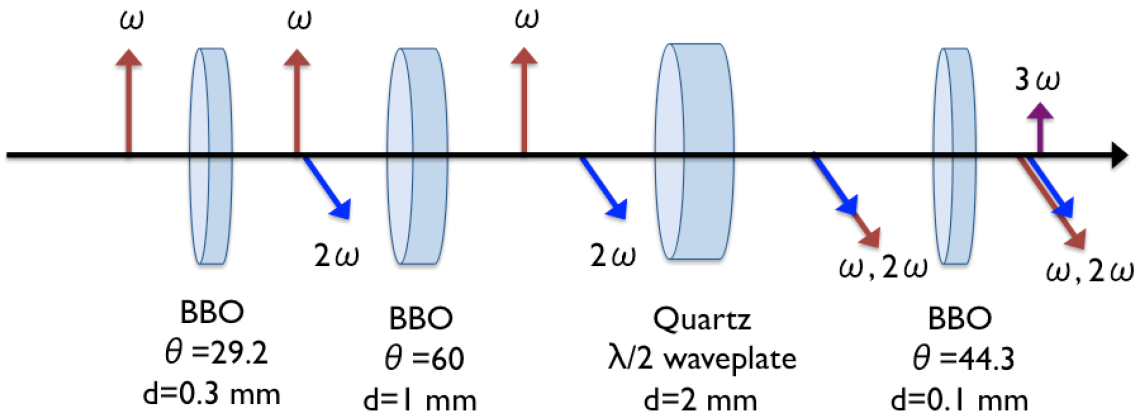

Fig. 3.23 Third harmonic generation schematic.

The harmonic system consists of four components. A second harmonic crystal, a temporal dispersion compensator, a waveplate, and a sum harmonic crystal. Beta barium borate (BBO) is an anisotropic, birefringent material with high second order susceptibility. By selectively orienting the axis of anisotropy, phase matching between the input and output beams can be achieved. This allows for high efficiency harmonic conversion and phase matching to be achieved.

The first BBO crystal is cut 29.2 degrees to it axis anisotropy, to achieve phase matching between the fundamental and second harmonic. The second harmonic is produced with its polarization vector perpendicular to that of the input beam. For this reason a waveplate is used to align the polarization of the fundamental and second harmonic. Dispersion within the quartz produces a delay between the two input beams, and another BBO crystal is used to compensate for this. Finally, with the polarizations aligned, a third BBO crystal, cut at 44.3 degrees, produces third harmonic light by sum frequency generation of the first and second harmonics. The overall conversion efficiency of our setup is about 5-10% percent, and provides more than enough for UV light for temporal calibration.

3.9 Streak Camera Temporal Performance

The temporal resolution of the grazing incidence streak camera is the sum of many factors: slit size, photocathode material, photon energy, sweep speed, spatial resolution of the imaging system, etc. The best resolution achieved for the transmission streak camera was 266 fs for UV light [62]. However, this transmission camera was optimized for temporal resolution and employed a 10 μm slit, which drastically limits light coupling and efficiency for larger source sizes. The grazing incidence streak camera operates with an 80 μm and achieves best resolution of 1.75 ps for UV light (measured) and 1.8 ps for x-rays (estimated). The single shot time resolution can be estimated by equation 3.9,

$$\Delta t_{ss} = \sqrt{\Delta t_{transit}^2 + \Delta t_{sweep}^2 + \Delta t_{sc}^2 + \Delta t_{\theta}^2} \qquad (3.9)$$

where the total single shot temporal resolution (Δt_{ss}) is determined adding the individual error contributions in quadrature. These terms result from energy dispersion of the secondary electrons produced ($\Delta t_{transit}$), finite sweep speed and imaged slit width (Δt_{sweep}), longitudinal elongation of the electron pulse from space charge effects (Δt_{sc}), and path length difference caused by the grazing angle (Δt_{θ}^2). It should be pointed out that equation 3.4 does not account for signal-to-noise, temporal jitter (Δt_{jitter}) and finite laser pulse width (Δt_{pulse}), all of which must often be considered when measuring the temporal resolution. The individual terms in equation 3.9 will now be individually considered.

The photon energy, both UV and x-ray, exceeds the work function of the cathode material, and as a result photoelectrons liberated from the photocathode have non-zero initial kinetic energy. In the case of UV light, these electrons have maximum energy spread of 0.5 eV (i.e. the difference between the photon energy and the work function). In the case of x-rays, the photon energy greatly exceeds the work function, and the secondary electron energy distribution is dictated by scattering processes within the photocathode material. Figure 3.24 shows the secondary energy distributions from Au and CsI cathodes under 1.487 keV x-ray illumination.

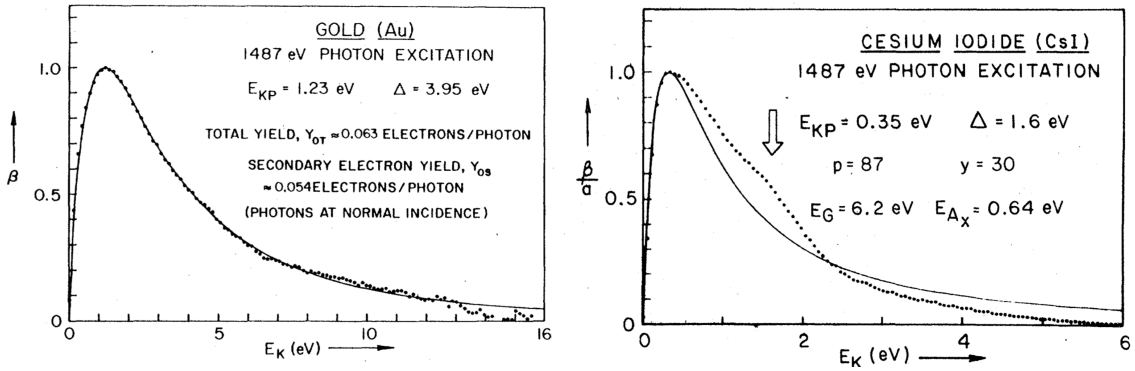

Fig. 3.24 Secondary electrons distributions. Normalized secondary electron distributions for gold and cesium iodide. Gold has a larger spread of secondary electron energies, but is chosen for its robust operation. [67]

For two electrons simultaneously emitted from the cathode surface with their velocity along the normal and an energy difference, ε, the difference in cathode to anode transit time will be,

$$\Delta t_{transit,\ c-a} = \frac{1}{E}\sqrt{\frac{2m_e\varepsilon}{e}} \tag{3.10}$$

where E is the electric field in the cathode to anode gap. To properly calculate the time dispersion the secondary electron distribution is integrated over all energies. The distribution of initial energies is given by [67],

$$N(\varepsilon) = \frac{C\varepsilon}{(\varepsilon + w)^4} \tag{3.11}$$

where C is a constant and w is the work function of the material. Integrating over the distribution and all initial velocity vectors gives,

$$\Delta t_{transit,\ c-a} = \frac{2.63}{E}\sqrt{\delta\varepsilon}\ (ps) \tag{3.12}$$

where $\delta\varepsilon$ is the FWHM of the secondary electron distribution in eV (~4 eV for x-ray photons and a Au cathode) and $E = \frac{V_o}{d}$ is the electric field in keV/mm. For a voltage, V_o, 10keV and a cathode to anode gap, d, of 1.2 mm gap this gives 225 fs (UV) and 630 fs (x-ray). It is also necessary to consider the difference in transit time from the anode to the sweep plates, l_{a-sw}, which can be calculated by,

$$\Delta t_{transit,\ a-sw} = l_{a-sw}\left(\frac{1}{v_{e(V_o+\delta\varepsilon)}} - \frac{1}{v_{e(V_o)}}\right) \tag{3.13}$$

where v_e is the velocity of the electron beam. At a voltage of 10 keV and an anode to detector length, l_{a-sw}, of 1.5 cm this value is small, but not negligible at 5 fs (UV) and 50 fs (x-ray). The secondary electron dispersion and transit time limit the maximum temporal resolution of many streak cameras designs, specifically in the x-ray regime, and drives demand for low dispersion cathode materials. Here, the greatest limitation in resolution is the large slit size, so gold becomes a good choice of cathode material because of its stable and robust operation. The error due to the limited sweep speed, v_{sweep}, and the width of the slit image on the detection is given by,

$$\Delta t_{sweep} = \frac{mw}{v_{sweep}} \tag{3.14}$$

where m is the magnification and w is the slit width. The sweep speed of the streak camera is measured by separating two UV pulses by a known path difference and recording their relative position on the detector. Sweep speeds up to $1.2\text{x}10^8$ m/s have been measured, and for an 80 μm slit size and m=2.5 this gives, Δt_{sweep} =1.66 ps. Δt_{sc} is the temporal broadening that is caused by the elongation of the beam due to space charge effects. This value depends on the charge of the electron bunch, but it is typically smaller than 100 fs.

The final term, Δt_θ, is due to the optical path difference of the light across the slit. This is given by,

$$\Delta t_\theta = \frac{w\cos(\theta)}{c} \tag{3.15}$$

where θ is the grazing angle. For a slit width of 80 μm and a grazing angle of 20 degrees this gives, Δt_θ=250 fs. Table 3.2 summarizes the individual resolution elements and

overall performance of the streak camera at UV and x-ray wavelengths. While the x-ray resolution is difficult to measure, the agreement between the estimated and measured UV resolution gives confidence in the estimate x-ray resolution.

80 μm Slit	$\Delta t_{transit}$	Δt_{sweep}	Δt_{θ}	Δt_{sc}	Δt_{laser}	Δt_{ss}
UV	230	1660	250	100	150	1704 fs
X-ray	630	1660	250	100	0	1796 fs

Table 3.2 Calculated streak camera resolution. All values are in fs. The top line identifies the individual resolution elements. The second line gives the estimated values for UV photons, and includes the laser pulse duration (Δt_{laser}), which must be included when measuring the resolution. The third line gives the estimated values for x-ray photons.

3.10 Beamline integration

Figure 3.25 shows a schematic of how the streak camera is integrated into beamline 6.02 at the ALS. The main laser pulse is initially split by a 10/90% beam splitter. The majority of the laser energy (10 mJ) is used to pump the sample and ~ 1mJ is used for the GaAs switch and UV fiducials. The pump beam is synchronized to the x-rays at the sample with the phase shifter discussed in chapter 2. A delay stage is used to time the streak camera optics. This synchronizes the voltage ramp within the sweep plates to the arrival of the photoelectrons liberated by x-rays absorption within the photocathode. Additional delay stages synchronize the arrival of two UV fiducials and set their temporal separation.

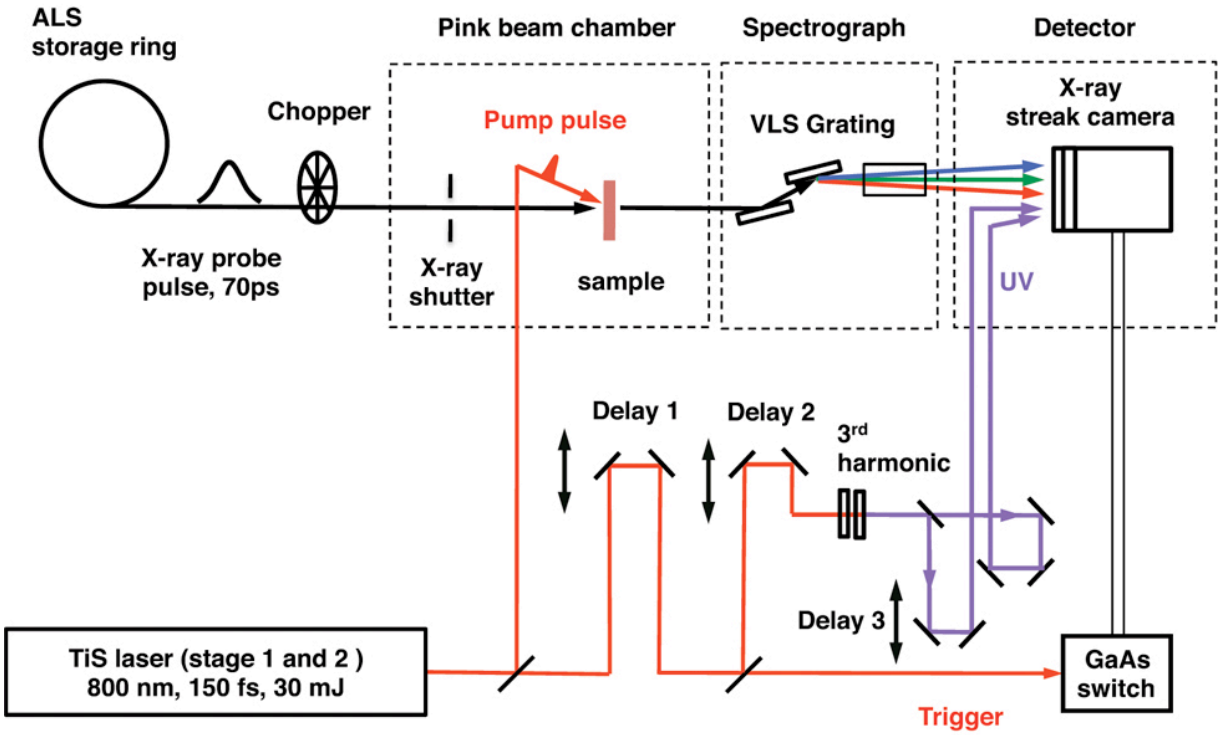

Fig. 3.25 Streak camera integration.

3.11 Image Processing

To acquire data of suitable signal to noise, approximately one hundred sample positions are measured at each laser pump fluence. The streak camera images are collected by a LabView program that automates sample motion. For each sample position three x-ray exposures are collected, one before the laser pulse, one during the laser pulse, and one after the laser pulse. In addition, background images, grating zero order images, and UV only images are collected. The images are processed in the following sequence. First a background is subtracted from each image. Then the images are shifted by aligning the UV pulses to account for any timing jitter, and each set (i.e. before, during, and after) is averaged. Then the image of the time resolved absorption spectra before and during the laser pulse is calculated by equation 1.11, where the after image is the incidence x-ray, because it passes through the damage hole. The grating zero order images and UV only images allow for the calibration of the energy axis and temporal axis, and can correct for any image curvature present (as shown in figure 3.27).

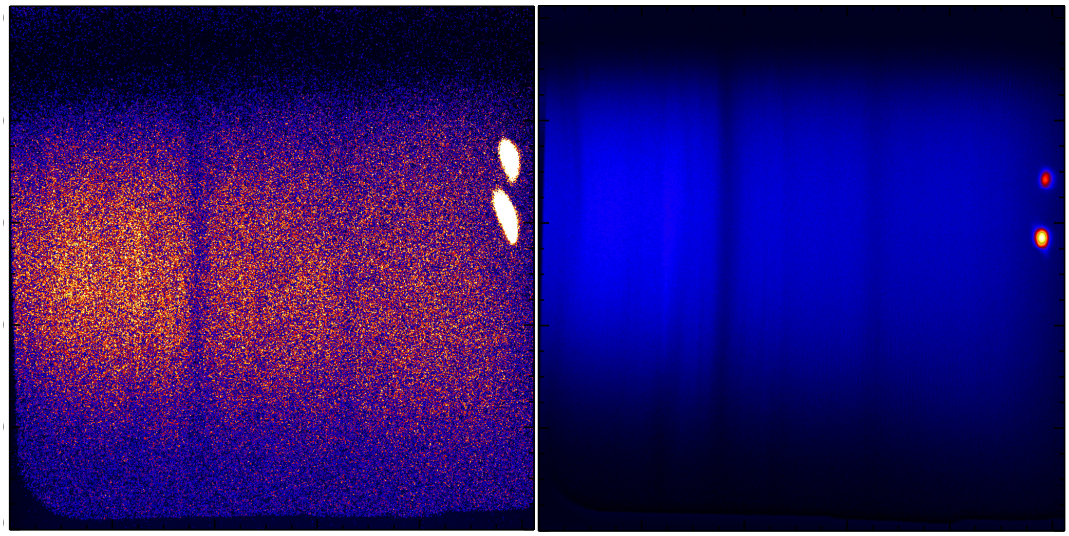

Fig. 3.26 Image Processing. A single streak camera image taken before the laser pulse with the Andor CCD (left). The average of 100 images after background subtraction and UV alignment (right).

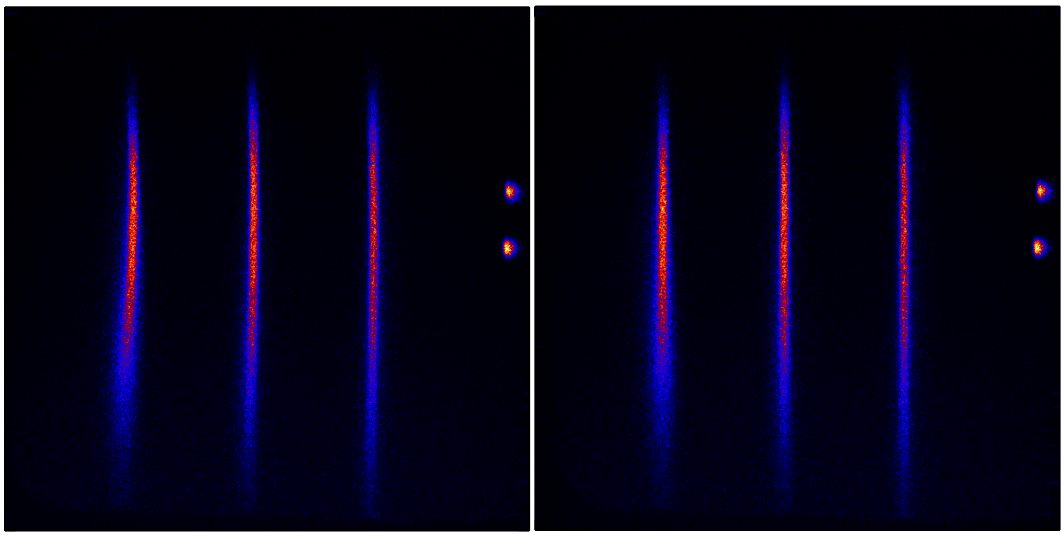

Fig. 3.27 Curvature Correction. Zero order images with curvature (left) and after curvature correction (right).

The result of this analysis is two images (with and without laser) of the x-ray absorption as a function of time and energy for the full duration of the x-ray pulse. This can be seen in figure 3.28.

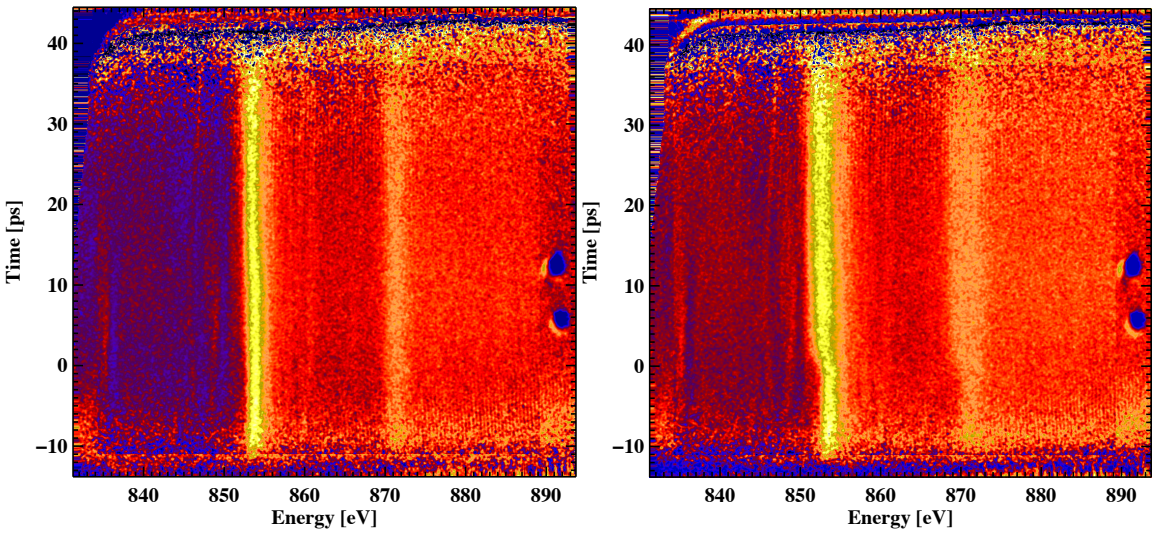

Fig. 3.28 Processed Images. An average of 100 x-ray exposure of nickel at the nickel L-edges without laser (left) and with laser (right).

Chapter 4

Warm Dense Silicon Dioxide

Silicon dioxide is a major constituent of the earth's crust and mantle. It is also a common material for optics, and optical damage can be initiated at "warm" conditions caused by the laser-matter interaction at high intensities. Additionally, optical waveguides have been written in fused silica by intense femtosecond optical pulses [3]. The mechanism is understood to involve the formation of a localized plasma followed by a micro-explosion inside the glass. Specifically, at low fluence, below 8 J/cm^2, smooth waveguides are formed, while at higher fluence rough waveguides are produced. From *ex situ* Raman scattering measurements, an increase in 3- and 4-membered rings in the silica network is inferred to be the result of the high intensity interaction. Ultrafast spectroscopy of transient warm dense silicon dioxide could provide information about the electronic and ionic states underlying the mechanisms of optical damage and waveguide writing by femtosecond lasers.

In SiO_2, previous electron spin resonance experiments have shown that ultrafast laser pulses can induce E' center defects in SiO_2 [79]. In an E' center, a Si atom is bonded to three oxygen atoms with a dangling sp^3 orbital. Using *ab initio* molecular dynamics (MD) simulations, Boero *et al.* [80] modeled the femtosecond laser irradiation by considering initial conditions of high T_e and ambient T_i. At 25,000 K T_e, Si-Si bonds were observed and displaced O atoms appear in three-membered rings.

Most recently, Denoeud et al. [81] used silicon K-edge XANES to study shock compressed SiO_2 at 1-5 g/cm^3 and temperatures up to 5 eV. MD-DFT calculations agreed well with the measured spectra and indicated a pseudo-gap corresponding to either a semimetal or a significant metallic component of warm dense SiO_2. The pseudo-gap was associated with a loss of Si and O correlation.

Here, we present a novel study of the electronic structure of warm dense silicon dioxide created by ultrafast laser excitation and probed by time-resolved XANES. MD-DFT simulations are used to support the interpretation of the experimental spectra. This leads to conclusions about the modification of bonding following an ultrafast laser excitation.

4.1 Experimental Parameters

The experiments were performed at Beamline 6.0.2 at the Advanced Light Source synchrotron facility at Lawrence Berkeley National Laboratory. The experimental setup is described in chapters 2 and 3 shown in Figure 3.25. The sample is 400 nm thick amorphous SiO_2. The sample is deposited from crystalline material via e-beam evaporation to a room temperature substrate, resulting in a completely amorphous structure [82]. The sample is then attached to a supporting mesh (70 lines per inch). A

150 fs, ~10 mJ Ti:sapphire laser pulse is focused to a 250 or 400 μm (fwhm) diameter spot at the sample, depending on the required fluence.

Silicon dioxide is an insulator whose band gap, in both amorphous and crystalline phases, is 8.9 eV [83,84]. This greatly exceeds the energy of the optical photons, 1.5 eV. The absorption of the optical photons occurs through multi-photon absorption exciting electrons from the valence band to the conduction band, free carrier absorption of electrons once in the valence band and plasma absorption after the conduction electrons reach a density approaching the critical density, n_c [85]. At the beginning of the laser pulse multi-photon absorption is expected to predominate, while at the end of the pulse, interaction with the plasma should be most important [86]. The optical absorption of the sample was measured at 800 nm by using an integrating sphere to collect the reflected and transmitted portions of the laser beam, as shown in figure 2.15. The absorption was observed to increase roughly linearly from 6 % at low fluence (2.5 J/cm^2) to 25 % at high fluence (15 J/cm^2), as shown in figure 4.1. It should be noted that the measured absorption is averaged over the temporal and spatial profile of the laser pulse and sample thickness. The excitation of the sample at the front and back surfaces varies according to the optical absorption. Since the sample remains mostly transparent, it is expected to be heated relatively uniformly across its thickness. The laser intensity also had transverse non-uniformity within the x-ray probe area, as discussed in section 2.4; this is determined by observing the distribution of laser intensities within the x-ray beam, as shown in figure 2.13. The absorbed fluences given below are average values, with standard deviations of, σ_+=10 % above and σ_-=35 % below the stated values.

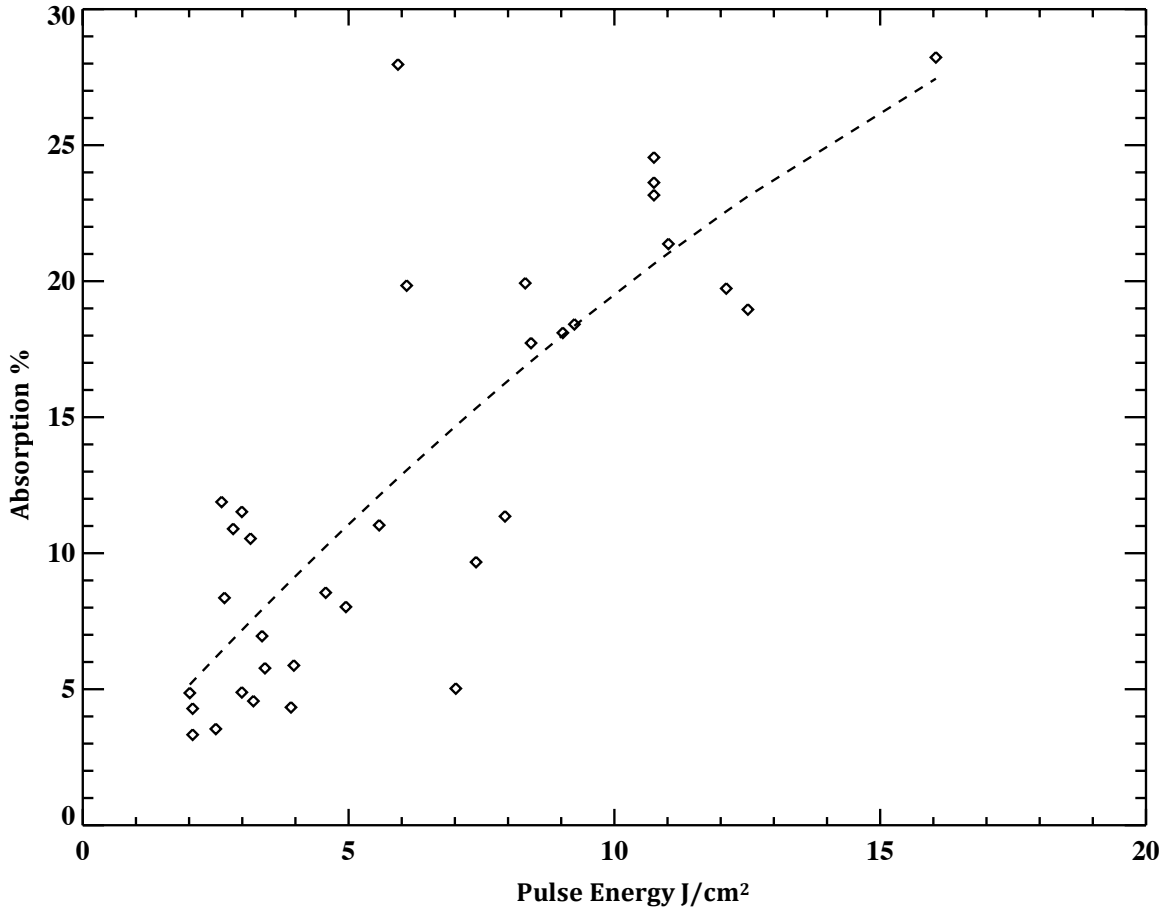

Fig. 4.1 SiO_2 Laser absorption. The absorption varies roughly linearly with incident laser pulse energy.

The SiO_2 sample is probed by a 70 ps duration, polychromatic x-ray pulse tuned to the oxygen K-edge. The x-ray bandwidth, ~25 eV, was limited by the grating dispersion and streak camera slit length. Consequently three spectral windows with different central photon energies were stitched together to produce the complete spectra shown below. The spectra have been confirmed with lower resolution spectra in which no stitching was preformed. A pair of slits reduces the x-ray spot size to either 150 x 150 μm^2 or 150 x 250 μm^2, in order that an area of relatively uniform fluence is sampled within the laser spot. The X-rays transmitted through the sample are dispersed by a variable line spaced grating spectrometer [56] and focused horizontally onto an x-ray streak camera [66], as discussed in chapter 2 and 3. The XANES spectra have an energy resolution of 0.6 eV determined mainly by the dispersion of the spectrometer and the spatial resolution of the streak camera. After each laser pulse the sample is translated to avoid the damaged area created by the previous laser pulse, and single shot spectra are collected at ~1 Hz. Roughly one hundred spectra are averaged for each laser fluence.

4.2 Experimental XANES of SiO_2

Figure 4.1a shows the oxygen K-edge XANES spectrum of SiO_2 at room temperature. The oxygen absorption edge is seen at 535 eV as well as two maxima above the edge. The measured spectrum is in agreement with the spectrum of vitreous silica [87]. Compared to the spectrum of α-quartz obtained by electron energy loss spectroscopy and XANES [88,89], the second peak of vitreous silica is observed at lower energy, but the general spectral features are mostly unchanged. This indicates that the XANES spectrum reflects the local structure of oxygen bonding. The spectra do not show the double peak feature characteristic of stishovite built from SiO_6 octahedra [88]. The structure of both α-quartz and vitreous silica is based on SiO_4 tetrahedra connected by corner-shared oxygen atoms. From multiple scattering calculations, Davoli *et al.* [90] concluded that the energy separation between the two peaks is sensitive to the Si-O-Si angle, which effects the local environment of the oxygen atoms [91]. Amorphous SiO_2 has been shown to have a range of bond angles [91], which contributes to the broadness of the spectral features present in the experiment.

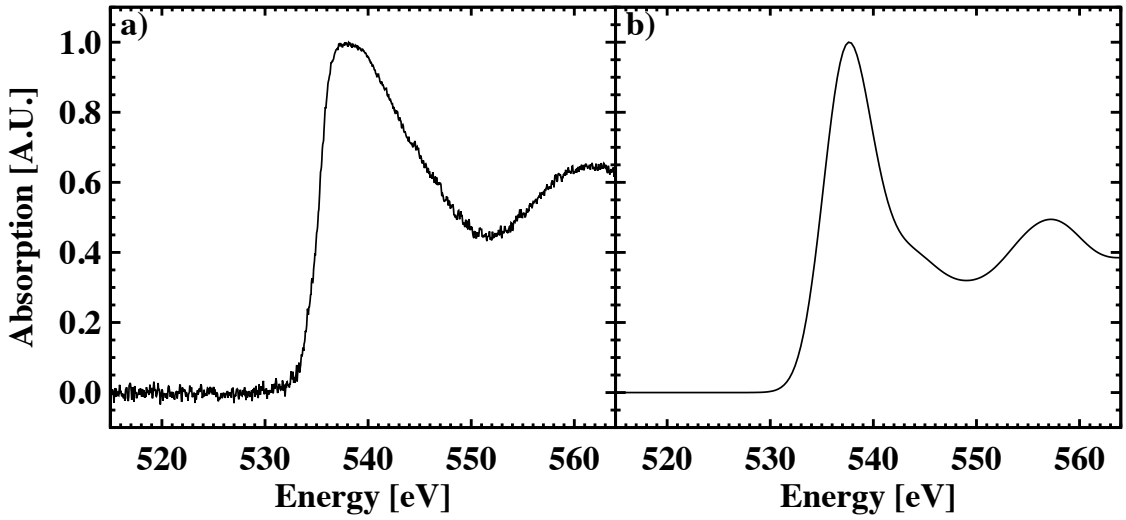

Fig. 4.2 XANES spectra of SiO_2. The room temperature O 1s spectra of SiO_2, experimentally measured in a) and the MD-DFT calculated in b).

Figure 4.2 shows the experimental oxygen K-edge XANES spectra at various laser fluences, 2.5, 5.5 and 15 J/cm^2 corresponding to absorbed energy densities of 1.7, 3.8, 10.5 MJ/kg. The optical to x-ray time delay is integrated from 0 to 20 ps. As stated previously, the x-ray streak camera time resolution is much higher than 20 ps; however, no significant change in the spectra was observed within this range of time delay. In comparison with the room temperature XANES spectrum, four qualitative changes are observed. The absorption edge is broadened. There is reduced contrast above the edge. There is absorption within the band gap. Finally, a peak is seen below the band gap (9 eV below the edge).

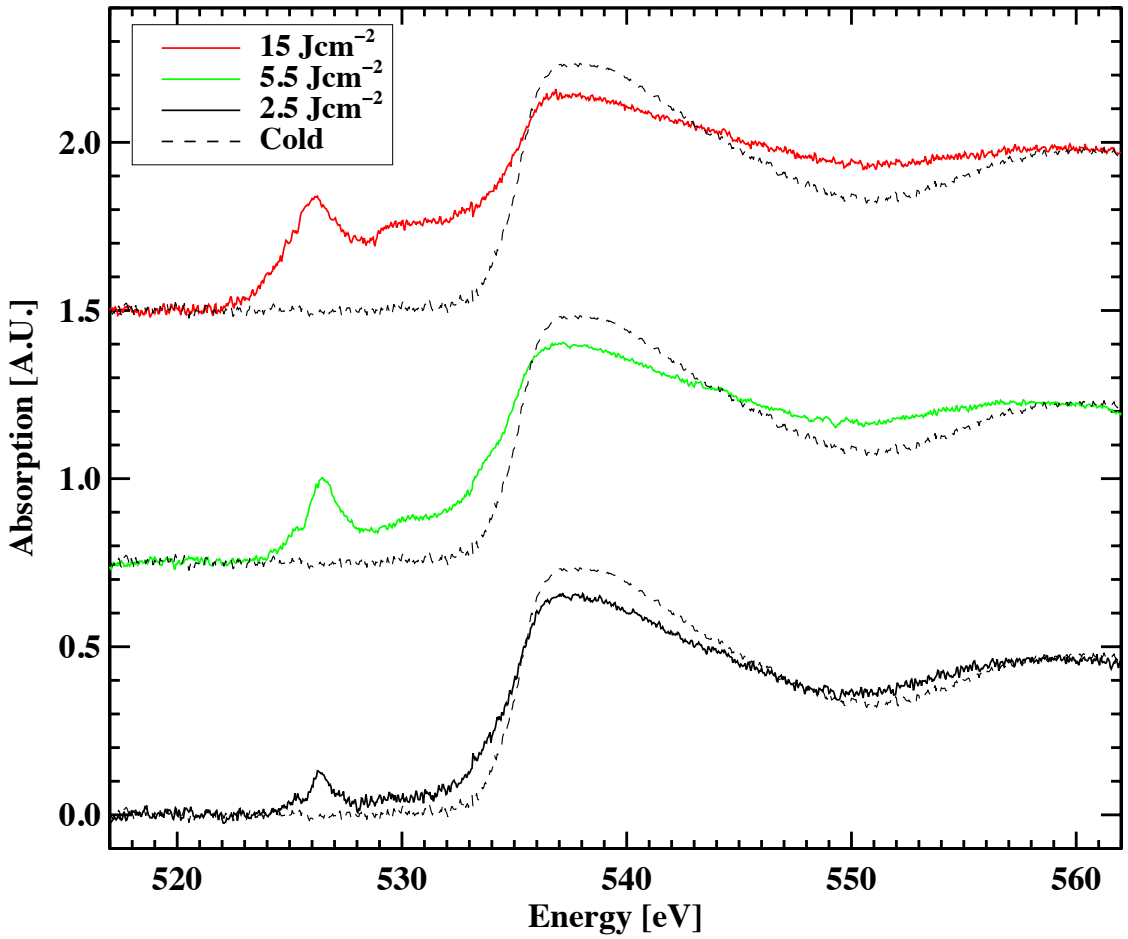

Fig. 4.3 XANES spectra of WD SiO_2. The experimental O 1s XANES spectra of SiO_2 at various laser fluences.

4.3 MD-DFT Calculations of WD SiO_2

In order to fully interpret the experimental spectra, we have performed *ab initio* MD simulations for SiO_2 at solid density (2.65 g/cc) and temperatures of 300 K, 5,000 K and 10,000 K using the ABINIT electronic structure code [92,93]. All calculations are carried out in the framework of the DFT with the generalized gradient approximation parameterization of the exchange and correlation potential [94]. The PAW (Projector Augmented Wave) [94,95] atomic data for Si consists of four outer electrons ($3s^2 3p^2$) and a cutoff radius of r_c=1.7 Bohr and six outer electrons ($2s^2 2p^4$) and a cutoff radius of r_c=1.2 Bohr for O. We used an energy cut-off of 680 eV. To obtain silica structure at a given temperature, 36 Si and 72 O atoms initially arranged in the perfect quartz lattice were propagated up to 1 ps using time steps of 1 fs in the iso-kinetics ensemble. All MD calculations were performed at the Γ-point. To obtain the optical response in the x-ray domain, we performed a detailed calculation of the electronic structure using a 3x3x3 Monkhorst-Pack mesh and 2,000 bands. Then we applied linear response theory to

obtain XANES spectra extending 30 eV above the edge, following the method described in the references [96,97]. The XANES spectrum is obtained in the so-called impurity model, by considering the absorbing atom in an excited state. The PAW atomic data for the absorbing atom is generated by using a hole in the 1s orbital of O. This calculation provides a simple way for introducing the core electron-hole interaction in the independent-particle description used here [88]. For each ionic configuration, this impurity is moved onto several O atoms in the cell. Each completed spectrum is obtained by averaging the individual spectra obtained for different impurity positions in the ionic configurations.

The room temperature theoretical spectrum for α-quartz is displayed in figure 4.1b. The calculated spectrum has been shifted in photon energy to match the position of the experimental absorption edge and convolved with the experimental resolution. There is satisfactory agreement both with the experiment and with previous calculated room temperature XANES spectra [98]. As previously noted by Taillefumier et al. [88], the calculated α-quartz spectral features are slightly contracted and the first maximum is narrower compared to measured amorphous SiO_2.

Figure 4.3 displays the calculated O 1s spectra for three electron temperatures, $T_i=T_e$, T_e=20,000 K, and T_e=30,000 K. In each case, spectra are shown for ion temperatures of 300, 5,000, and 10,000 K. In the calculated spectra, the same qualitative changes are seen as in the laser heated spectra. As the ion temperature increases, the edge broadens, and the contrast above the edge is reduce. As the electron temperature increases, a peak forms below the band gap and absorption occurs within the band gap.

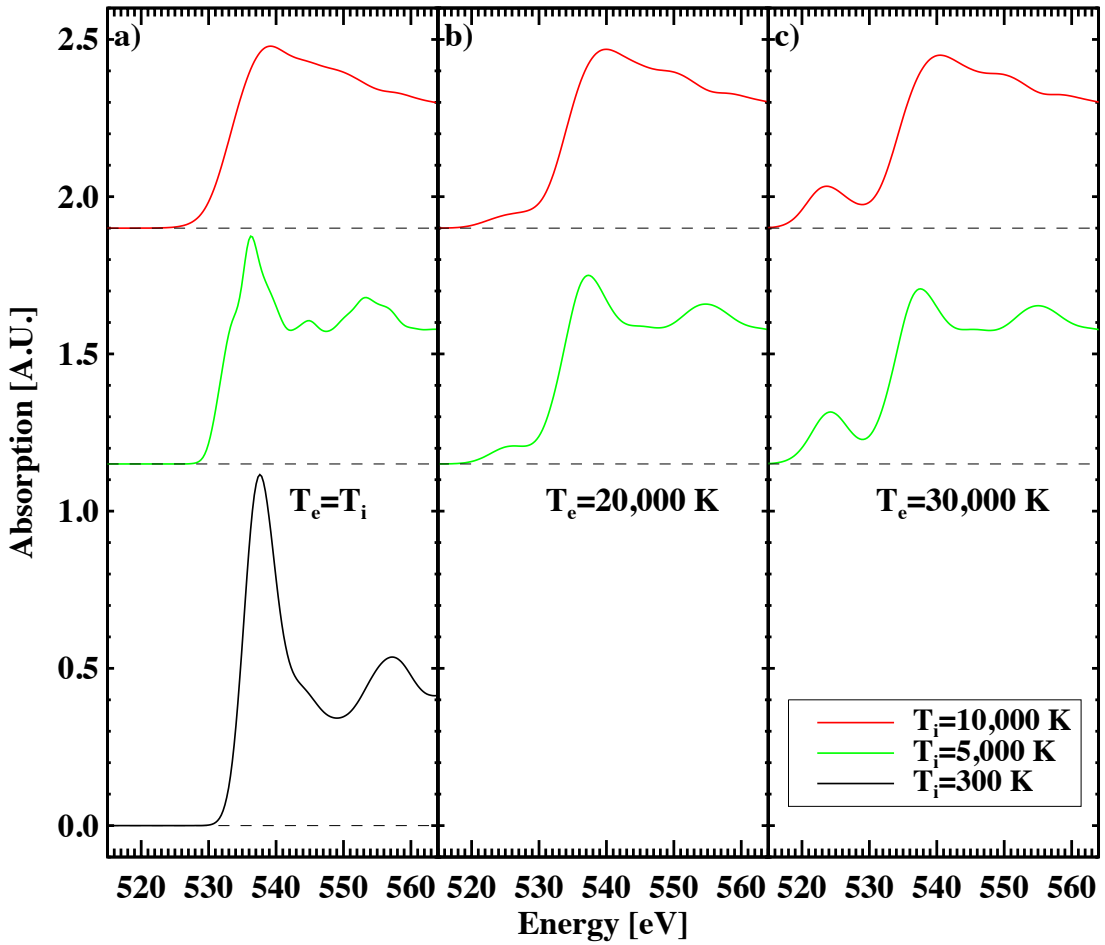

Fig. 4.4 Calculated XANES spectra for WD SiO_2. The calculated O 1s XANES spectra of SiO_2 at T_i= 300 K (α-quartz), 5,000 K and 10,000 K (liquid), where $T_e = T_i$ in a) at T_e=20,000 K in b), and at T_e=30,000 K in c).

Figure 4.4 displays the radial distribution function, g(r) calculated for O-O, Si-O and Si-Si, where the different curves show the equilibrium cases of equal T_e and Ti at 300 K, 5,000 K and 10,000 K. The height of the first peak in all three g(r) curves is reduced dramatically at the elevated temperatures. For the Si-O g(r), this change may be interpreted as a result of broken Si-O bonds. In the g(r) for O-O at 10,000 K a small peak is observed at 1.4 Å, indicative of O atoms directly bonded to other O atoms. In general, the diminished structure in the g(r) reflects an increased disorder in the high temperature liquid SiO_2.

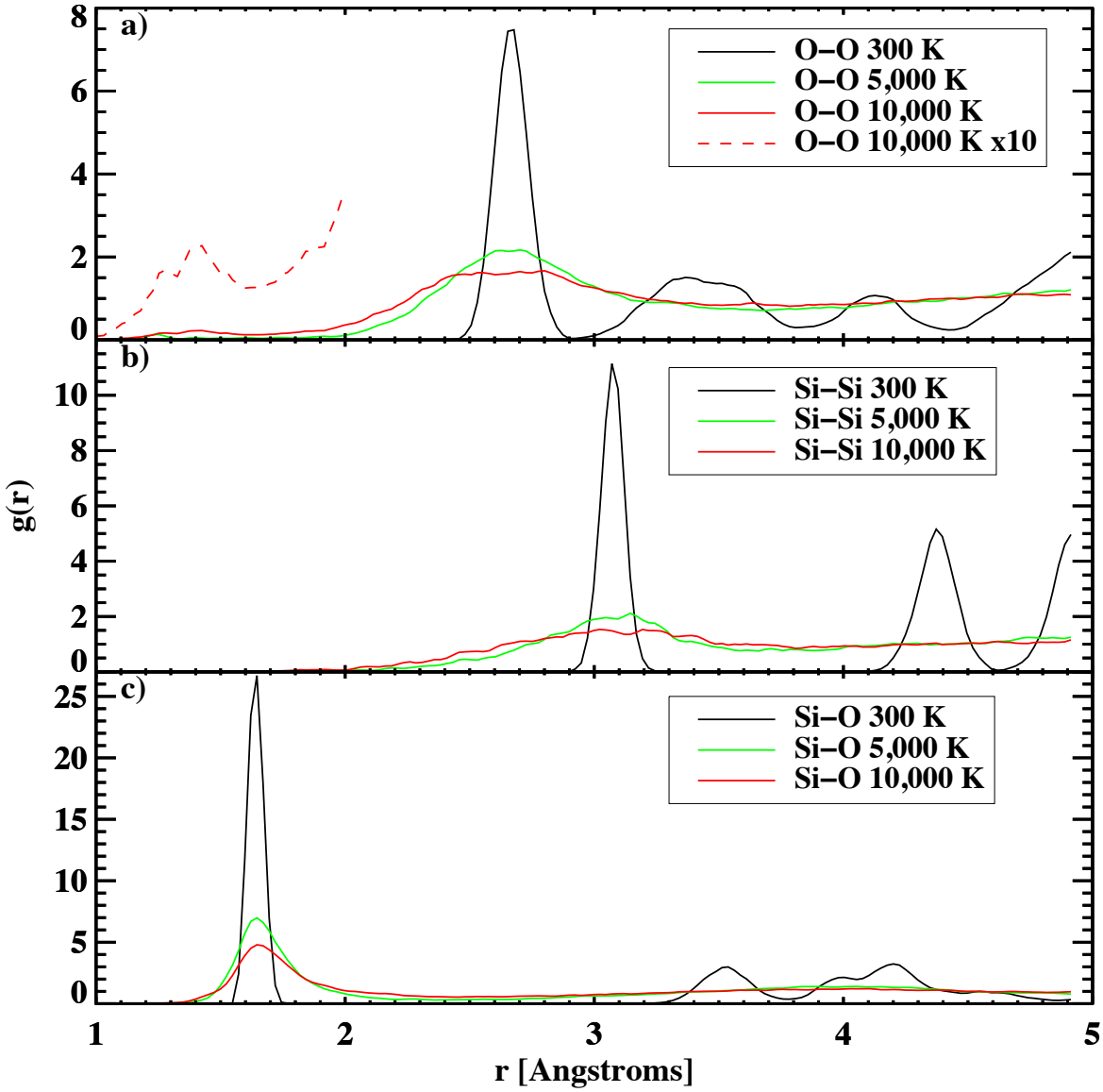

FIG. 4.5 Radial distribution functions of SiO_2, g(r), for SiO_2 under the conditions of $T_e = T_i$ at 300 K, 5,000 K and 10,000 K for O-O a), Si-Si b), and Si-O c). The 10,000 K O-O g(r) in a) (red dashed line) has be multiplied by 10 to illuminate the peak at 1.4 Å.

4.4 WD SiO2 Discussion

As previously pointed out in Mancic *et al.* [50] for the case of aluminum, the sharpness of the spectral features is correlated to the degree of local order. As the ionic temperature increases, the contrast of the minimum above the edge was reduced when the aluminum became a high temperature liquid. The experimental spectra in figure 4.2 show this behavior, with the contrast decreasing as the laser fluence increases. In the calculated XANES spectra, the absorption edge is broadened, and the structure above the edge becomes increasingly less marked at high ion temperature. As temperature

increases, the SiO_4 tetrahedra are broken which can be seen by the decreased height of the first peak in the Si-O radial distribution function on figure 4.4c. The minimum above the edge is present in the experimental laser-heated spectra as well as in the calculated spectra at 300 and 5,000 K, but missing in the calculation at 10,000 K. This comparison indicates that the experimental ion temperature is less than 10,000 K.

Absorption within the band gap is seen in both the experimental laser-heated in figure 4.4 and calculated XANES spectra at T_i of 5,000 and 10,000 K. At low laser fluence, there is a small absorption in the band gap. At the higher fluences, this absorption increases. As the temperature increases, the band gap is filled with defect states originating from broken Si-O bonds [79]. This loss of bonding states in the electron structure is reflected in the ion structure by the reduced height of the first peak of g(r) for Si-O. The observation of broken Si-O bonds and increased disorder indicate a possible mechanism for laser-induced optical damage as well as for laser writing of waveguides.

The effect of the electron temperature on the SiO_2 XANES spectra is now considered. The O 1s XANES spectra show the unoccupied p-like DOS. For quartz, the topmost valence band has been assigned to non-bonding oxygen 2p orbitals [99]. This band is occupied at room temperature and does not appear on the spectra. As electronic temperature increases, and this band will start to be depopulated by the Fermi Dirac function and appear in the XANES spectrum as a pre-edge peak. When the electronic temperature increases, the size of the pre-edge peak increases as the number of empty states rises. There is also a shift of the pre-edge peak to lower photon energy as states are depopulated further from the Fermi level. In both experimental and calculated spectra, this behavior is observed.

As the structure of SiO_2 is modified by the ultrafast laser pulse [79] [78], it is important to consider if different O bonding geometries may contribute to the pre-edge feature. A pre-edge peak has been previously measured at 528.3 eV for vitreous silica and attributed to a π^* state from O-O bonding [100]. Here, the pre-edge peak is seen at a different energy, 526 eV. Oxygen atoms in three-membered rings have been predicted [79], but the XANES spectral signature of these O atoms is not known. The calculated density of states below the Fermi level changes at the different temperatures: 300, 5000 and 10,000 K and may be effected by the presence of different oxygen structures. Nevertheless, the presence of the pre-edge peak results from the depopulation of these electronic states by the Fermi Dirac occupation function associated with the elevated electronic temperature.

Electron-phonon coupling has also been extensively modeled in metals [30], and measured in proton heated carbon [47] and shock compressed silicon [46]. Electron-phonon coupling is dependent on the details of the electronic structure and vibrational spectrum. It can vary by two orders of magnitude, resulting in electron-ion equilibration times of warm dense matter from a few ps to a hundred ps. Using a simple formulation for collisions, based upon a calculated electron-ion collision rate of 2.5 fs^{-1} [101,102], the equilibration time between the electron and ion temperature is estimated to be 43 ps.

Following the formulation given by Lin *et al*. [30] and equation 1.4, the temperature dependent electronic heat capacity is calculated from the density of states (shown in figure) and used to estimate T_e immediately after the laser excitation, giving T_e=20,000, 30,000 and 50,000 for the three absorbed energy densities.

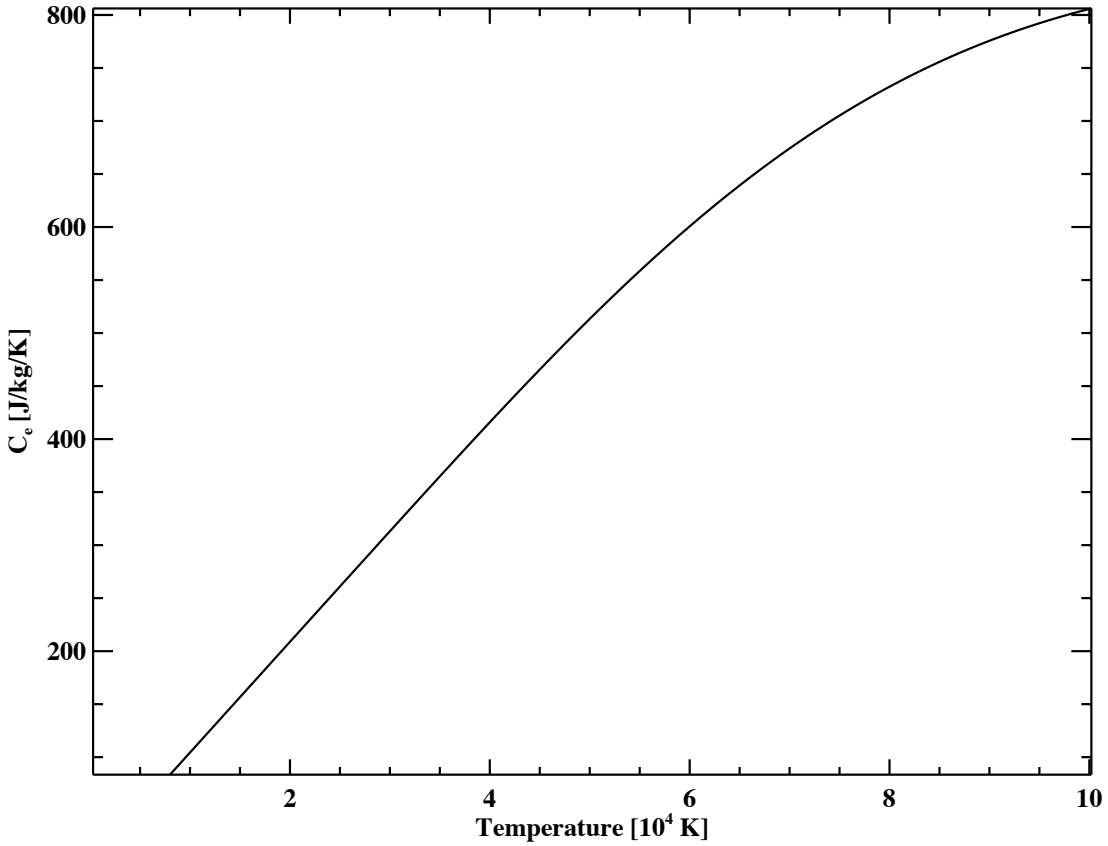

Fig. 4.6 Electron Heat Capacity of SiO_2. For temperature below ~10,000K the heat capacities were omitted due to computational error.

For the measurement at 0-20 ps, the electron temperature may be higher than the ion one. The height of the pre-edge peak is a sensitive measure of the electronic temperature. The calculated absorption spectra show a defined pre-edge at T_e=30,000 K, which is not present at T_e=20,000 K. The calculation underestimates the band gap as 5.5 eV compared to the known value of 8.9 eV [82] because of a known limitation of DFT [99]. For this reason, a direct determination of T_e is omitted. This may also over estimate the temperature dependent electron heat capacity. Nonetheless, it is concluded that the warm dense SiO_2 formed by the ultrafast laser excitation is observed to be in a non-equilibrium state with $T_e > T_i$.

In conclusion, measurements and calculations have been performed of the XANES spectrum of warm dense SiO_2. The heated material is seen to have an electronic structure distinct from the room temperature solid. Through comparisons of measured and simulated spectra, the spectral features are understood and insight into both the local

ionic and electronic behavior is gained. Following the laser excitation, Si-O bonds are broken, resulting in states within the band gap that increase with laser fluence. Spectral features constrain the ionic temperature, while a peak below the band gap shows unoccupied states in the valence bands consistent with a high electronic temperature, indicating the presence of a non-equilibrium liquid with $T_e > T_i$. A reduced sharpness of spectral features reflects an increased disorder in this high temperature liquid. These XANES measurements provide a detailed description of how SiO_2 transforms from an insulator with well-defined local structure to a high temperature liquid with reduced Si-O bonding.

Chapter 5

Warm Dense Copper

X-ray absorption spectroscopy is an effective probe of electronic structure. However, for a characterization of electronic structure to be meaningful, the warm dense matter must be in a well-defined state with determined physical quantities, such as temperature, density and pressure. As discussed in section 1.4, isochoric heating and the use of time resolved techniques can measure a sample of known density [103,104]. However, accurate measurement of temperature has proven to be difficult. Optical pyrometry is a good diagnostic for temperature, but the short time scales associated with isochoric heating limits signal levels and the emissivity of materials in the WDM regime is not precisely known [105]. X-ray Thomson scattering has demonstrated the capability to determine the temperature, electron density, and ionization degree [106], making it a powerful diagnostic for WDM research. However, Thomson scattering has a large temperature uncertainty (more than 1 eV) at low temperatures. On the other hand, x-ray absorption spectroscopy provides information on electronic structure and optical pump / x-ray probe techniques have been developed to study dynamical properties [64]. Recently, a study of the x-ray absorption spectrum (XAS) of warm dense aluminum heated by laser-accelerated protons was reported [50]. A broadening of the *K* edge was observed and attributed to a change in the electron population near the Fermi energy at high temperature. In addition, a loss of structure in the absorption spectrum was attributed to a loss of order in the high temperature liquid. For Cu, a photoemission study using ultrafast laser-heating observed a reduced intensity in the *3d* peak. This change was attributed to a lower occupation of the *d* band at the elevated electron temperature [104].

Here we present a study of the electronic structure of warm dense copper created by ultrafast laser excitation and probed by time resolved x-ray absorption spectroscopy. The x-ray absorption spectrum near the Cu L_2 and L_3 edges probes the unoccupied electronic density of states (DOS) in 3*d* and 4*s* bands. Under strong optical excitation, the electron temperature T_e of solid density Cu is quickly increased to ~ 1 eV. The experimental XAS are compared with the theoretical XAS derived from MD-DFT calculations. This framework provides an accurate measurement of electron temperature, and from the time dependence of the electron temperate, electron-phonon coupling of the non-equilibrium state of warm dense copper can be inferred.

5.1 Experimental Parameters

The experiment was performed at beamline 6.0.2 of the Advanced Light Source, the setup is detailed in chapters 2 and 3. The sample is a freestanding Cu foil of 70 nm thickness coated on both sides with 6 nm of amorphous carbon to prevent oxidation of the Cu surface. The foil is mounted to a supportive mesh (70 lines per inch). In this case, the pump beam was frequency doubled to 400 nm and focused (250 × 200 μm FWHM). The x-ray energy was tuned to the Cu *L* edges and the spot size was set to 200 × 100 μm

for the spatial overlap with the laser focus. The x-ray bandwidth was approximately 60 eV. The streak camera provides 2 ps temporal resolution [65]. The data was acquired during multi-bunch operation (section 2.1). The background signal present in multi-bunch operation (section 3.6) required the use of an MCP image intensifier (section 3.7) for gating purposes. This resulted in an energy resolution of 1.1 eV and a Lorentzian line shape at the Cu *L* edges [55]. At the streak camera the x-ray intensity is estimated to be 10^4 (photons/pulse/eV/2 ps).

The 400 nm pump wavelength was chosen because of the absorbance of Cu, shown in figure 5.1. The d-band of Cu lies approximately 2 eV below the Fermi level and is completely occupied in the ground state configuration ([Ar] $3d^{10}$ $4s^1$). This results in a small density of states (figure 5.2) near the Fermi level, and a small absorbance for photon energies less than 2 eV. By frequency doubling the 400 nm photons have sufficient energy (3.1 eV) to access the high density of states in the d-band and excite 3*d*-*4p* interband transitions. This increases the room temperature laser absorption from approximately 5% at 800 nm to approximately 50% at 400nm. A measurement of the reflection and transmission (section 2.4) of the 400 nm laser light indicates that 60% of the laser energy is absorbed in the pumped sample. The optical penetration depth of the laser is short (14nm [45]), so the most of the laser energy is absorbed at the front surface. However, the ballistic electrons (section 1.4) heat the sample uniformly over the electron mean free path (70 nm [44]). The sample is irradiated with an incident laser fluence of 0.33 ± 0.07 J/cm^2, which corresponds to an absorbed energy density of $3.6 \pm 0.7 \times 10^6$ J/kg. Fourier Domain Interferometry (FDI) of Cu indicates a surface expansion velocity of ~ 1 nm/ps therefore a near-constant density will be maintained for a time of order a few ps following the ultrafast laser pulse.

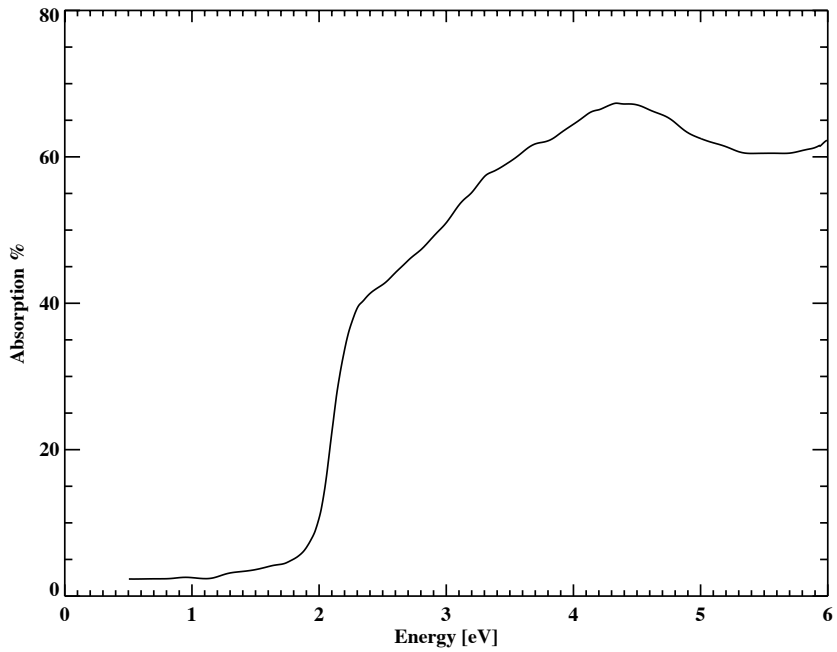

Fig. 5.1 Copper absorbance. The room temperature absorbance of copper has a sharp increase at ~2 eV due to the availability of 3d-4p interband transitions. Generated from [107].

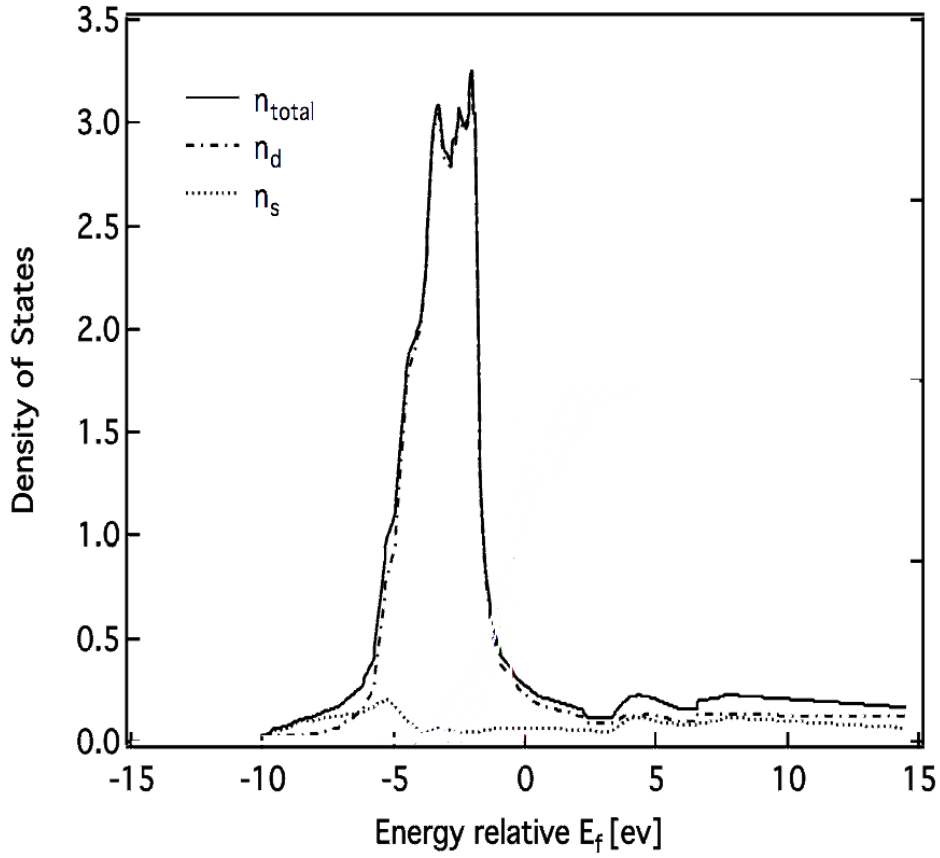

Fig. 5.2 Copper DOS at room temperature. The total density of states is shown in the solid line and the partial density of states are shown in the dashed lines (d-band) and the dotted line (s-band). Adapted from [108].

5.2 Experimental XANES of WD Copper

The laser pulse at $t = 0$ introduces a rapid increase in the absorption, below both the L_3 and L_2 edges that slowly recovers in ~ 20 ps. Figure 5.3 shows the XANES of warm dense copper at selected times. The room temperature spectrum is observed without a laser pulse and is averaged over 70 ps. The three peaks of XANES spectrum follow the observed solid Cu spectrum under ambient conditions [109]. Because of the 2 ps streak camera time resolution, the XANES at $t = 0$ includes an average of the WDM spectra and the room temperature spectrum. At 2 ps, the position of the L_3 edge is shifted to lower photon energy, and the absorption above the original L_3 edge is decreased. Around the L_2 edge, the same phenomena are observed although the effects are smaller because of the larger L_2 natural linewidth caused by the allowed Coster-Kronig Auger transition. After 6 ps, the L_3 edge appears broadened, and by 20 ps time delay the difference from the room temperature XANES is further reduced. These dynamics indicate that electrons are excited from below to above the Fermi level ε_F, and that there is a relaxation of the electronic excitation on a time scale of ~ 6 ps.

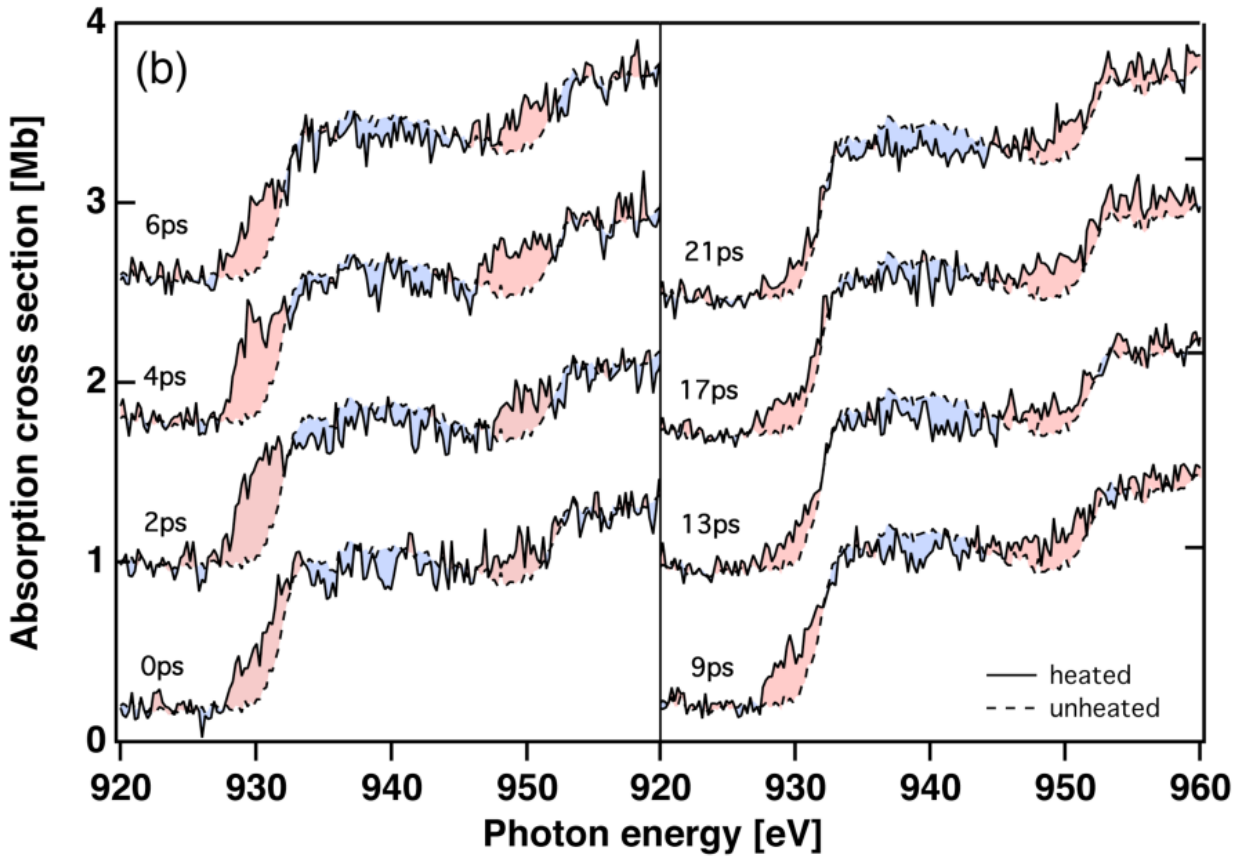

Fig. 5.3 XANES of WD Copper. The XAS of warm dense copper after the arrival of the laser pulse (T=0 ps) at selected times (solid curves). For comparison, the room temperature XAS of Cu is also shown as the dotted curves.

5.3 MD-DFT Calculations of WD Copper

To further interpret the measured XAS, it is necessary to compare with MD-DFT calculations. For the initial state, a face centered cubic solid at ambient conditions is assumed, and the solid density of Cu is maintained for all calculations. A cubic supercell containing 32 atoms is used. For the room temperature calculations T_i=T_e=300 K. An ultrasoft pseudopotential is used to describe the Cu ions with *3d*, *4s* and *4p* as valence states, and the electronic wave functions are expanded by a planewave basis with periodic boundary conditions. The electronic structure is optimized for each time step and the atomic configuration is propagated based on Newtonian mechanics. For the MD simulations, the Chadi-Cohen's two special k-points sampling for fcc crystal was used [110]. On those atomic configurations, the x-ray absorption cross sections are calculated from the dipole transition matrix elements between the Cu *2p* core state and unoccupied states (Kohn-Sham eigenstates). The Quantum Espresso package [111] is used to generate both the atomic configurations and the Kohn-Sham eigenstates, and the prescription developed by Prendergast and Galli is used to reconstruct the oscillatory property of electronic wave functions near the vicinity of nuclei from the smoothed pseudo wave functions [112]. The k-points integration is performed using the

interpolation scheme described in by Predergast [113]. To obtain satisfactory ensemble averages for each absorption spectrum, an average over all 32 atoms in a single cell and for 200 independent snapshots was performed. In terms of system size, the convergences of both the DOS and the absorption spectrum were achieved.

The room temperature measured and calculated absorption spectra are shown in figure 5.4. The Fermi distribution for 300 K is applied to the solid x-ray absorption cross section. The total x-ray absorption spectrum is constructed as the superposition of L_3 and L_2 edges, where the L_2 edge is obtained by shifting L_3 edge spectrum by 20 eV. Deviations from the statistical 2:1 ratio of L_3:L_2 is observed for *3d* transition metals [114], so an L_3:L_2 branching ratio of 1.8:1 is chosen to fit the experimental spectrum. A single scaling factor adjusted the absolute cross section of all the calculations to the measurements. Energy and edge-dependent lifetime broadening is separately added to the L_3 and L_2 edge spectra [115]. The whole spectrum is convolved with a 1.1 eV Lorentzian function, representing the experimental resolution.

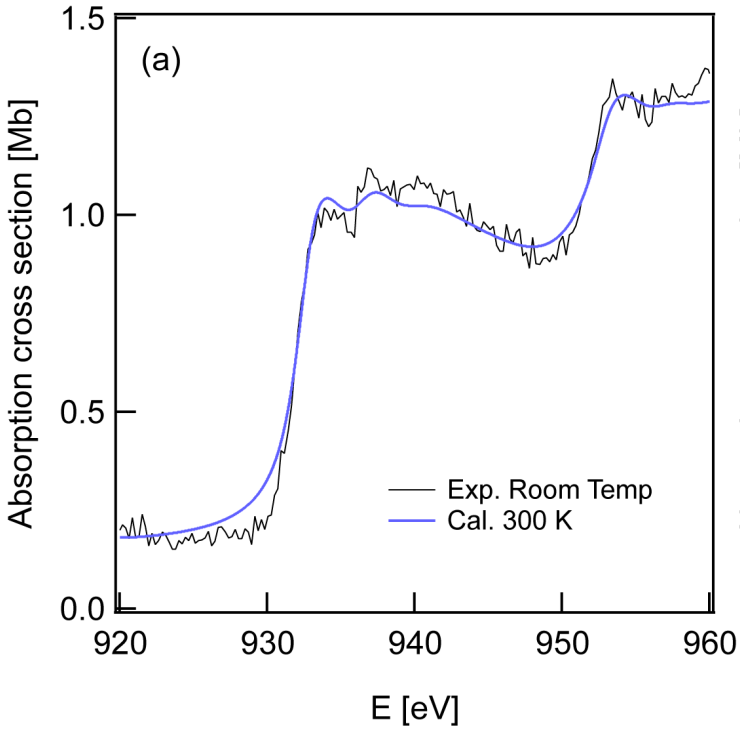

Fig. 5.4 Room temperature XANES fit of Copper.

For the state following the laser pulse, liquid atomic configurations at electron temperature, T_e of 12448 K and ion temperature, T_i of 3846 K are used in the MD-DFT Calculations. It should be noted that the calculated x-ray absorption cross section was not very sensitive to the T_e and T_i used for the MD simulations but depend strongly on the T_e used to calculate the XANES. Therefore, T_e and T_i are chosen based on the two temperature model, which is described in section 5.4. Initially the optical excitation heats the electrons and the ions remain cold. However, on a timescale less than the detector resolution, the electron-phonon coupling may increase the ion temperature higher than the melting point. Typical comparisons of the measured and calculated XAS are shown

in figures 5.5 and 5.6. Because of the sensitivity of the *L*-edges to the electron temperature, the T_e can be determined with an accuracy of ~ 1000 K by comparing the edge shift and broadening.

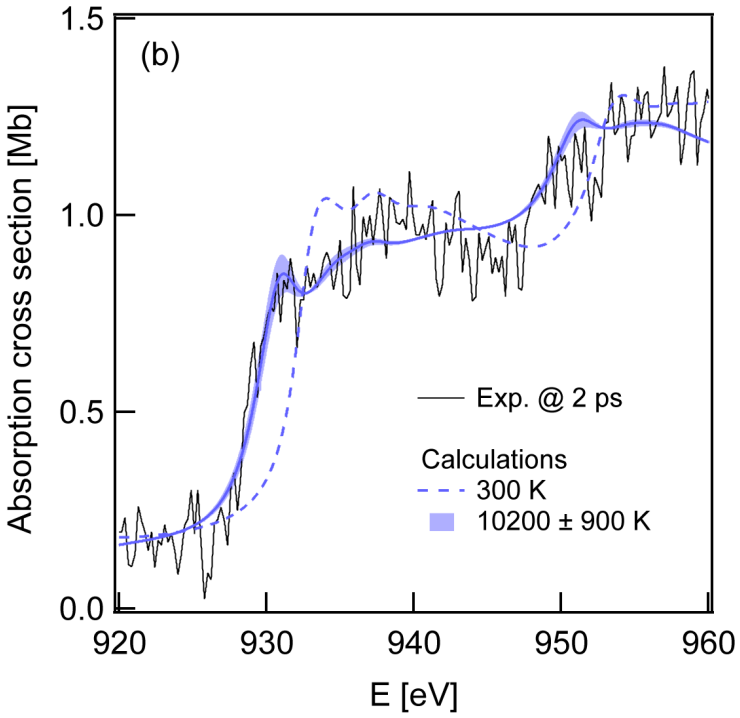

Fig. 5.5 WD XANES fit of Copper at 2ps.

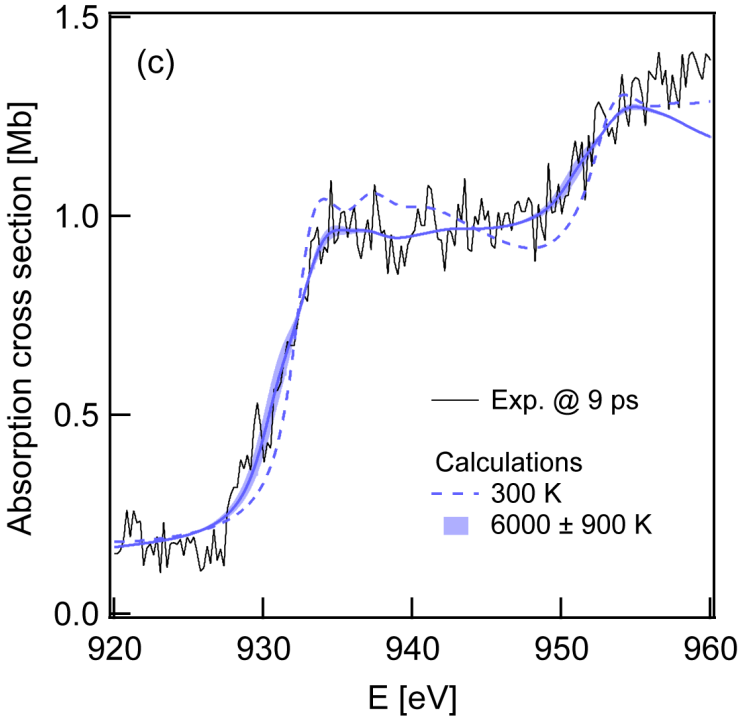

Fig. 5.6 WD XANES fit of Copper at 9ps.

The strong red shift of the *L*-edge at early time is a consequence of the elevated electron temperature and the high *d*-DOS below ε_F. The broadening of the edge at later times (e.g. 9 ps) results from the lower electron temperatures. It is also noted that the calculated XAS reproduces the shape of the experimental XAS above the edge, which has ~ 10 % lower absorption than the room temperature solid. This reduction cannot be explained by the electron occupation at ~ 10000 K. The solid and liquid DOS at these energies are also similar (figure 5.7). Therefore, the change in the XAS above the edge is explained by a decrease in the x-ray absorption matrix elements for the $2p \rightarrow s, d$ transitions. Overall, there is a quantitative agreement between the measured and calculated XAS.

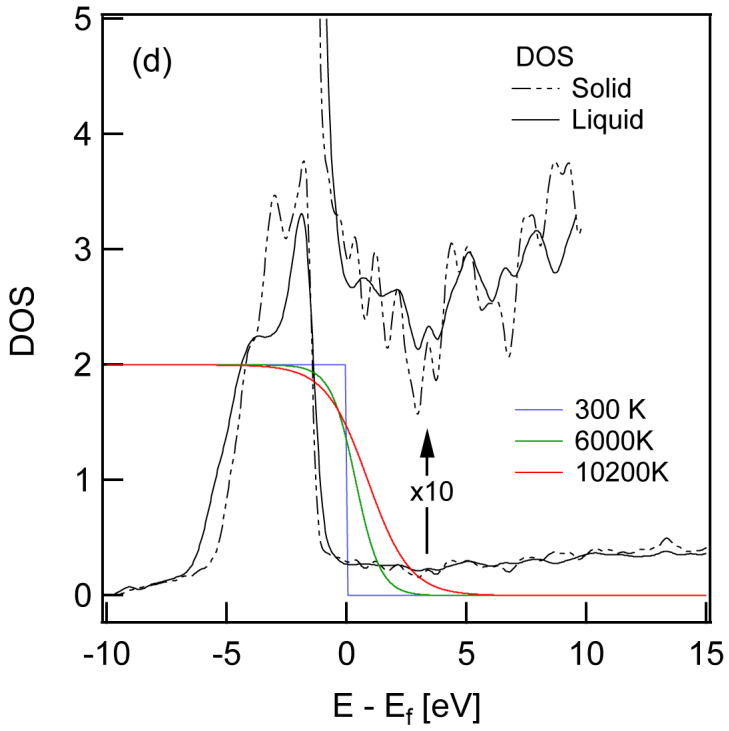

Fig. 5.7 Solid and liquid DOS of Copper.

Optical pyrometry data was also taken of the heated Cu foil. The pyrometry setup uses six fast photodiodes to measure the emission from the target surface at six different energy bands with a temporal resolution of 400 ps. The emitted light is imaged onto an optical fiber, the output of the optical fiber is then collimated and reflected by six band pass interference filters (550±40 nm, 750±40 nm, 900±40 nm, 1,100±20 nm, 1,300±40 nm, and 1,500±40 nm). Photodiodes behind the band-pass filters measure the relative intensity at each wavelength range. The setup is calibrated with tungsten ribbon lamp of known brightness temperature. Further details on this experimental setup can be found in the reference [105]. The optical pyrometry indicates a peak brightness temperature of ~ 3100 K at 400 ps (figure 5.8). This result is in reasonable agreement with the XAS given the differences in the time scales of the two techniques.

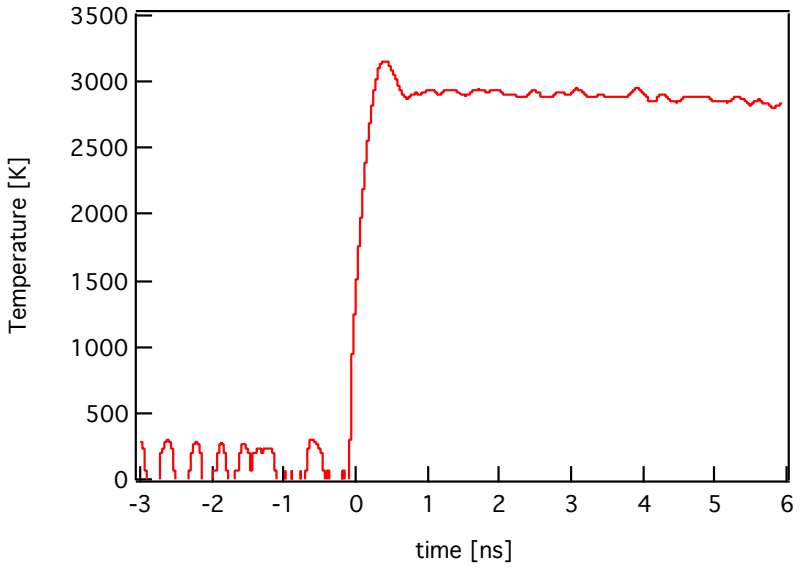

Fig. 5.8 Optical pyrometry of WD copper.

Density changes may result in a shift in the absorption edge [96]. However, simulations of copper at 0.5 of solid density did not well reproduce the measured XAS at and above the edges. From the low density calculation and the FDI results, it is concluded that constant density is a good approximation for early time delays while at later time delays, > 5 ps, hydrodynamic expansion could play a role. We also note that the electron temperature of Cu determined by comparing experimental and calculated XANES is sensitive to the energy of the *d*-band. In fact, the calculated energy of the *d*-band of solid Cu is overestimated by 0.4 eV when referred to photoemission data. The overestimation of the *d*-band energy is a common disadvantage of the DFT methods [116].

5.4 Two-Temperature Model

The dynamical evolution of the electron temperature is shown in figure 5.9. The measured T_e quickly increases to a peak of ~ 10200 K at 2 ps. It starts to decrease and reaches ~ 4500 K after 10 ps.

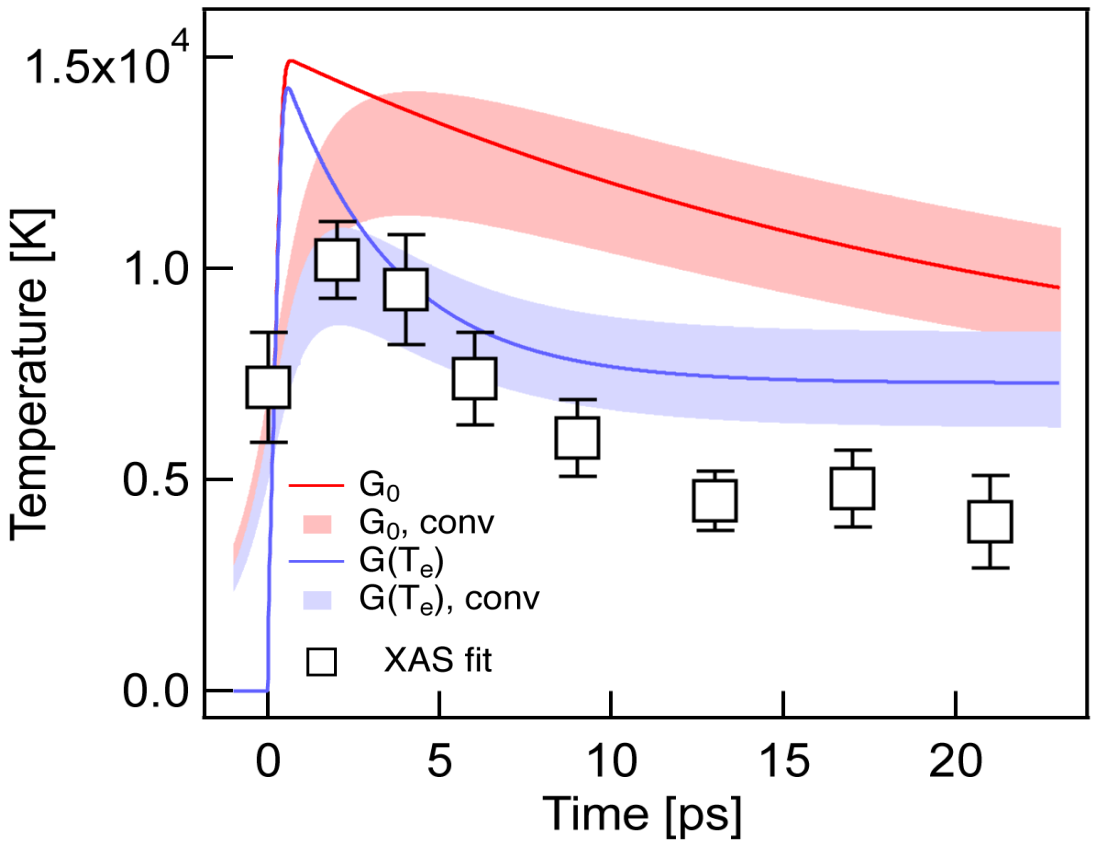

Fig. 5.9 Temporal evolution of T_e. Experimental-derived values of the T_e are shown as squares. For G_0 (red) and $G(T_e)$ (blue), solid lines are the T_e calculated by the TTM. The shaded curves include the experimental accuracies in the S_L and the temporal resolution of the detector.

To understand the observed dynamics of warm dense copper, we employ the two-temperature model (TTM) [118]. This model, widely used for femtosecond laser-solid interactions, describes the temporal evolution of T_e and T_i according to,

$$C_e(T_e)\frac{dT_e}{dt} = -G(T_e)[T_e - T_i] + S_L(t) \tag{5.1}$$

$$C_i\frac{dT_i}{dt} = G(T_e)[T_e - T_i] \tag{5.2}$$

where G is the electron-phonon coupling factor, and C_e and C_i are the electron and ion heat capacities, respectively. C_e is obtained from equation 1.4. C_i is 3.5×10^6 J/m^3 K, obtained by the Dulong-Petit law and is assumed to be constant. S_L is the energy deposition by the laser pulse. For the electron-phonon coupling parameter, a value of $G_0 = 10^{17}$ Wm^{-3} K^{-1} is experimentally measured up to the temperature of 2200 K [119]. Recently, Lin *et al*. derive an expression for the T_e-dependent electron-phonon coupling factor $G(T_e)$ (equation 1.1) and calculate the values for various metals including Cu [30], for which $G(T_e)$ increases dramatically from room temperature to a value of 5.3×10^{17} Wm^{-3} K^{-1} at 10000 K. Using the calculated $C_e(T_e)$ and the values of $G(T_e)$ shown in figures 5.10 and 5.11, $T_e(t)$ and $T_i(t)$ have been derived. The same calculations with a constant $G_0 = 10^{17}$ Wm^{-3} K^{-1} have also been performed for comparison. The results are

shown in 5.9.

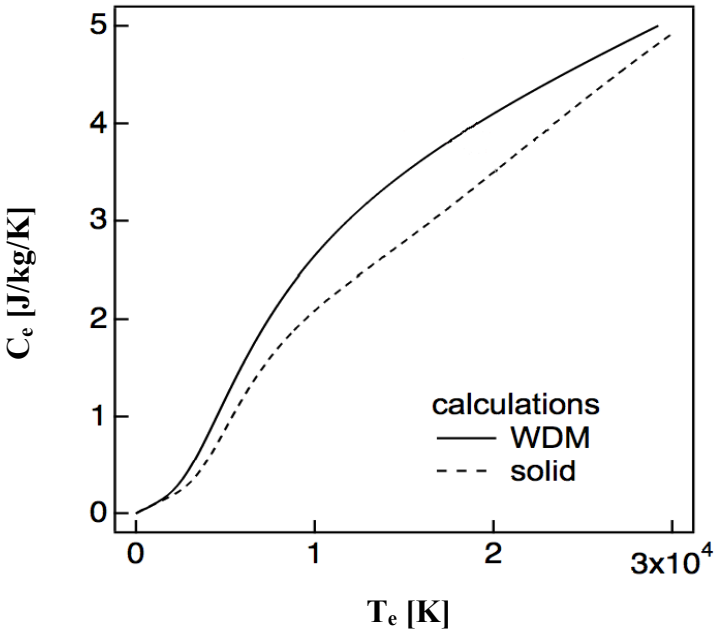

Fig. 5.10 Temperature dependent electron heat capacity. Calculated from the density of solid density of states (dashed line) [30] and calculated from the liquid density of states (solid line).

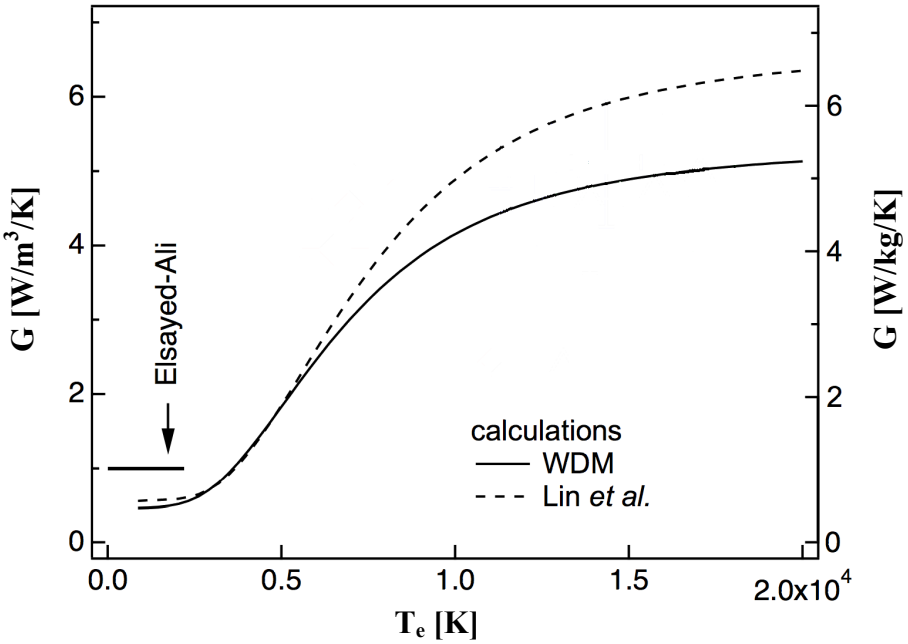

Fig. 5.11 Temperature dependent electron-phonon coupling. Calculated from the density of solid density of states (dashed line) [30] and calculated from the liquid density of states (solid line).

Both results show that the electron temperature peaks at the end of the laser pulse, and then decreases. But comparing to the constant G_0, the temperature dependent $G(T_e)$ provides lower values of T_e, a faster decrease in T_e, and as a result a better agreement with the experimental data. It indicates that the electron-phonon coupling factor of Cu is enhanced in this temperature regime. We note that at longer time delay the experimentally observed electron temperatures are lower than the TTM calculations, indicating the onset of additional electron cooling mechanisms. Hydrodynamic motion is a possible cause.

In conclusion, we have observed the evolution of the unoccupied electron DOS of warm dense copper via time-resolved XAS. Good agreement is observed between measured XAS and calculated spectra based on the DOS of liquid Cu. From the edge shift and broadening, the electron temperature of non-equilibrium states of warm dense matter could be determined in the 10000 K regime. The reduction of x-ray absorption above the edge results from a change in the transition matrix elements. The evolution of electron temperature can be described by a two-temperature model including T_e-dependent electron heat capacities and electron-phonon coupling factors.

Chapter 6

Warm Dense Nickel

The relative position of the Fermi level to the d-band plays a crucial role in determining the electronic properties of transition metals. These properties include optical reflectivity, heat capacity, electrical and thermal conductivity, and the electron-phonon coupling parameter. For this reason, it is interesting to study and compare WDM of transition metals for which the Fermi level has a different location with respect to the d-band. Previously, Copper was studied by x-ray absorption spectroscopy, measuring the unoccupied DOS of the warm dense state. In the case of copper, the Fermi level is located above the d-band, so the d-band is full with a nominal ground state configuration is [Ar] $3d^{10}$ $4s^{1}$ (figure 5.2). This leads to several important predictions for copper's electronic properties, such as an increasing electron-phonon coupling parameter with increasing temperature, as shown in figure 5.11 [30]. By comparison, the Fermi level in nickel is located just below the top of the d-band and yields a ground state configuration of [Ar] $3d^{8}$ $4s^{2}$ (figure 6.1), and results in a high DOS at the Fermi level.

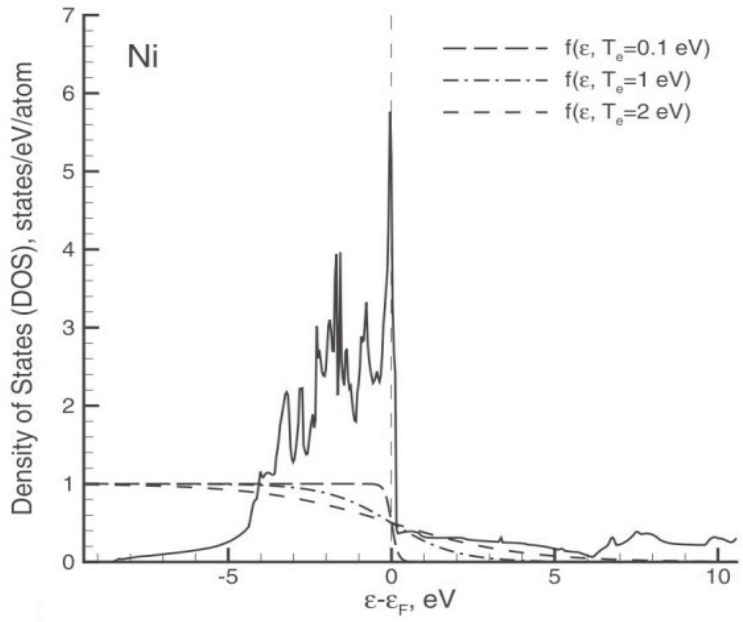

Fig. 6.1 Nickel DOS at Room Temperature. From [30].

This dictates (equation 1.1) that while nickel has strong electron-phonon coupling at room temperature, an order of magnitude stronger than copper, it will sharply decrease with increasing electron temperature, as shown in figure 6.2. The afore mentioned differences between copper and nickel, despite their proximity to one another on the periodic table, make nickel an interesting candidate for study to confirm these predictions and further the understanding of the role of d-band electrons in a material's physical properties at high temperature.

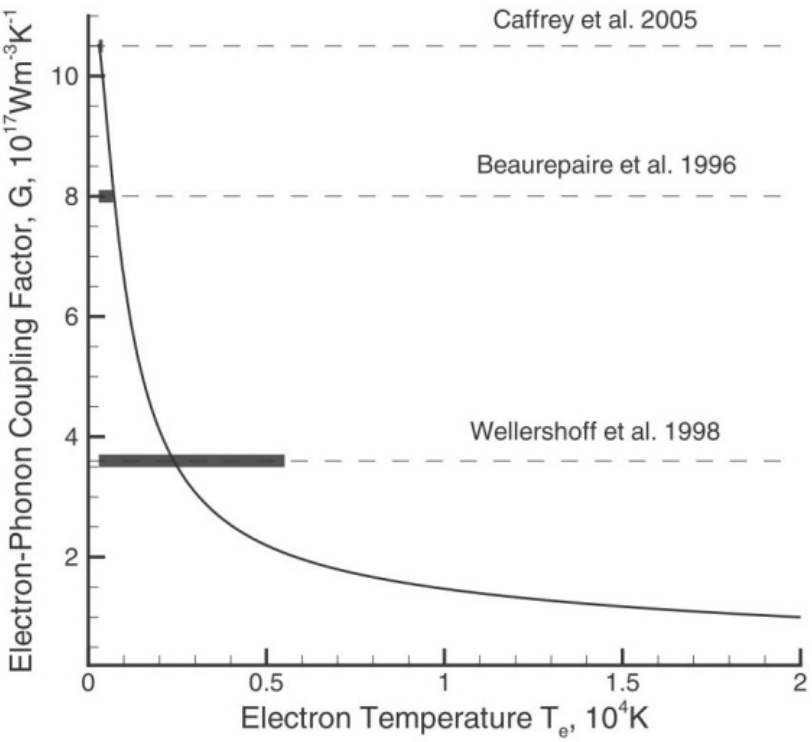

Fig. 6.2 Calculated temperature electron-phonon coupling in nickel. From [30].

6.1 Experimental Parameters

The experiment was performed at beamline 6.0.2 of the Advanced Light Source, and the experimental setup is detailed in chapters 2 and 3. The sample is 20 nm of Nickel tamped on each side by 100 nm of SiO_2. The mostly transparent SiO_2 layer is added to restrict the expansion of the sample and allow for longer timescales to be studied. The SiO_2 tamping layers with an approximate sound speed of 4000 m/s are estimated to keep the sample at constant density for ~ 50 ps. The thickness of the nickel layer is chosen in order that the nickel layer is uniformly heated while maintaining structural integrity. The ballistic electron mean free path is estimated at 11 nm [44], and the optical skin depth is 10 nm at 800 nm [46]. A 150 fs, ~1-20 mJ Ti:sapphire laser pulse is focused to 350 μm x 350 μm at the surface of the sample. The 1.55 eV photons within the optical laser pulse initially pump the 3d-4p interband transition, but once in the 4p band, the promoted electrons can absorb additional optical photons. The optical laser absorption was measured by the methods described in section 2.4. However, to estimate the absorption of the tamping layer, an additional absorption measurement was performed on a free standing, 100 nm SiO_2 sample. This absorption within the SiO_2 was measured to be less than 5%, which is consistent with the results from chapter 4. The absorption of the nickel layer, shown in figure 6.3, was measured to be between 60-70%. It is not known what fraction of the laser light pumps the interband transition compared to the free-free transition of electrons promoted to the 4p band.

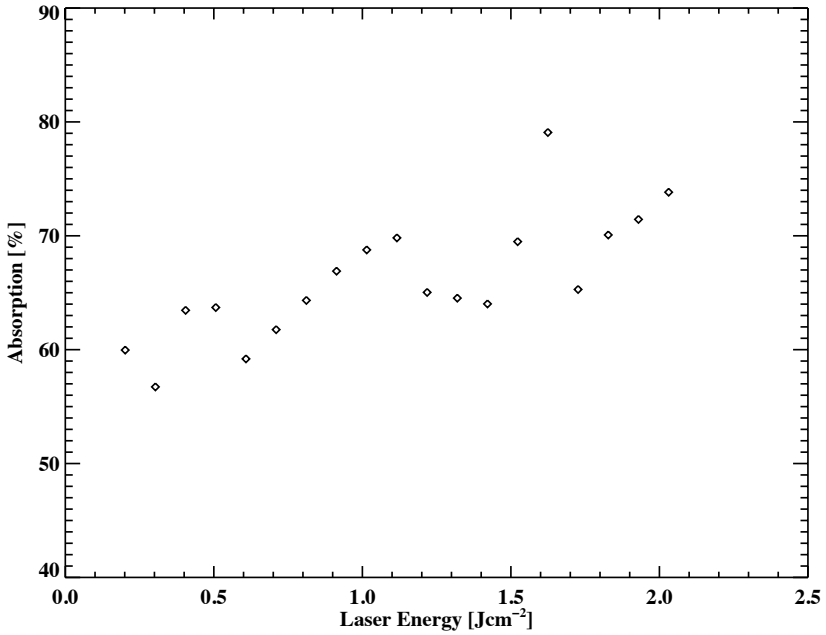

Fig. 6.3 Nickel laser absorption.

The sample is probed by a 70 ps, polychromatic X-ray pulse tuned to the nickel L-edges. A pair of slits reduces the X-ray spot size to 150μm x 250μm, so that an area of relatively uniform fluence is sampled within the laser spot. The near edge spectra (~70 eV) are collected by the streak camera with a resolution of 0.65 eV [56,66]. Each optical laser pulse creates a hole in the target, consequently the sample is rastered, and single shot spectra are collected at ~1 Hz. Roughly one hundred images are combined for each laser fluence.

6.2 Nickel XANES

The spectra collected from the tamped nickel targets, shown in figure 6.4, exhibit novel behavior. The heated spectra show clear deviations from the room temperature spectra: the absorption edge is red shifted by ~1.2 eV, the absorption peak is broadened, and the absorption above the edge decreases. Furthermore, the spectral shape does not change substantially over the observed 30 ps window. Figure 6.4 also shows spectra for three fluences (0.35, 0.7, and 1.4 J/cm^2 corresponding to absorbed energy densities of 12, 24, and 50 MJ/kg), and the spectra at these fluences all look remarkably similar in shape to one another.

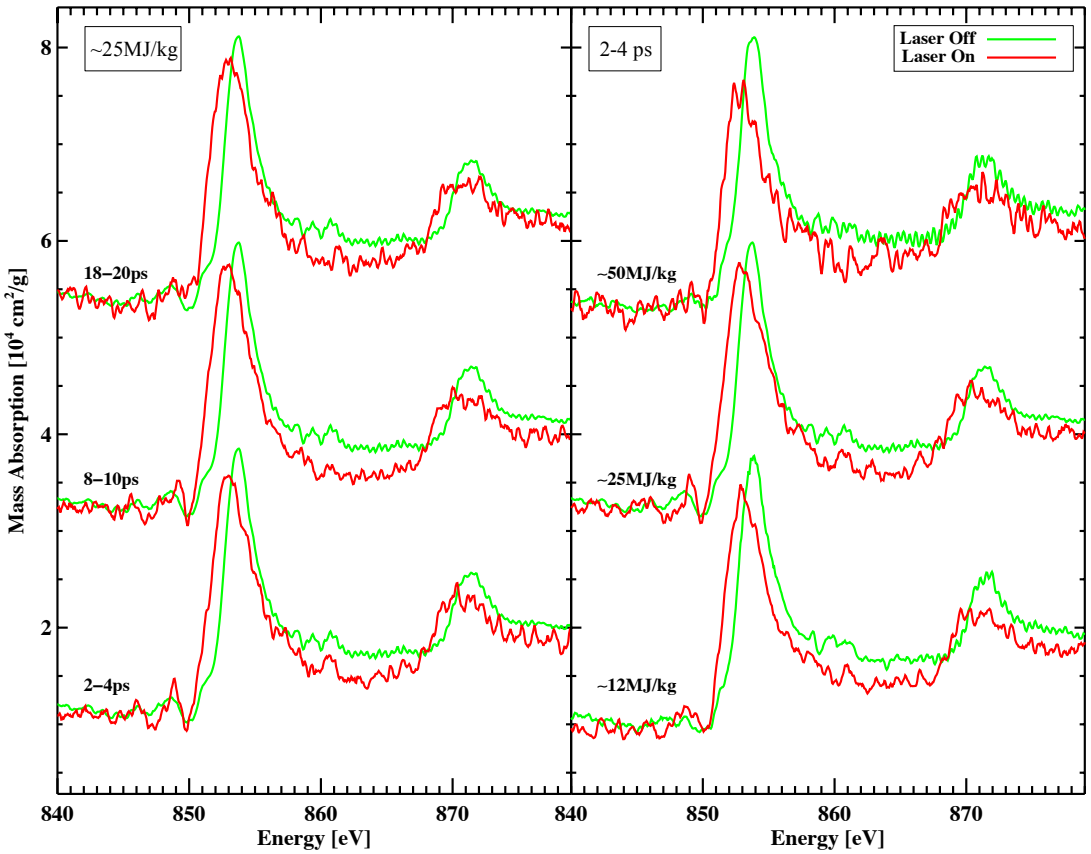

Fig. 6.4 XANES of nickel. Room temperature data is shown in green and heated (laser on) data is shown in red. (Left) Data at 25MJ/kg shown at three times, 2-4 ps, 8-10 ps and 18-20 ps after the arrival of the laser. (Right) Data from three absorbed energy densities (12MJ/kg, 25MJ/kg, 50MJ/kg) red curves are time averaged from 2-4ps.

6.3 MD-DFT Calculations of WD XANES

The experimental data are compared with calculations generated by MD-DFT. From the analysis based on the two temperature model, a set of electron temperatures and ionic temperatures for the given delay times were determined. First-principles molecular dynamics simulations within the DFT were then performed at these physical conditions using Quantum-espresso package [30]. The simulation box containing 32 Ni atoms were used together with the 2^3 k-point sampling in order to address the larger size effect of electronic degree of freedom than that of ionic degree of freedom. The ultrasoft pseudo potential for the ionic core of Nickel together with the plane wave expansion for the electronic wave functions were used where the cutoff energy for the wave function was set at 30 Rydberg and the cutoff energy for the charge density was set at 300 Rydberg. From each simulation, multiple snapshots were chosen at the time steps separated by several hundred femtoseconds in order to have uncorrelated atomic configurations. On these configurations, the X-ray absorption cross-section matrix elements within the dipole approximation were then calculated using the prescription for the pseudo potential based scheme described in the reference [113]. The dense k-point sampling (20^3 k-points)

by interpolation [114] was sampled in order to ensure the convergence on the broad spectral feature originating from the highly dispersive free electron like states. We adopted the no-core-hole approximation for the final state, which was found to be a good approximation for metallic systems [109]. The average was then taken over the uncorrelated snapshots, though the snapshot-to-snapshot variation of dipole matrix elements turned out to be small. The calculated x-ray absorption spectra are generated in several steps. First, the density of states is used to calculate the temperature dependent chemical potential. The density of states is then multiplied by the x-ray transition matrix elements. For a given temperature, the Fermi function selects the unoccupied states. The L_3 and L_2 absorption spectra are then independently corrected for lifetime broadening [116], and the L_3 and L_2 spectra are added together with an energy shift of 17.5 eV and a weighting of 2:1. Finally, the generated spectrum is convolved with the detector resolution (0.65eV). This method produces excellent agreement for the room temperature spectra (figure 6.5), with only minor disagreement occurring at very high photon energy, beyond 875eV. This result yields confidence that the DOS and matrix elements calculated are accurate for the room temperature sample.

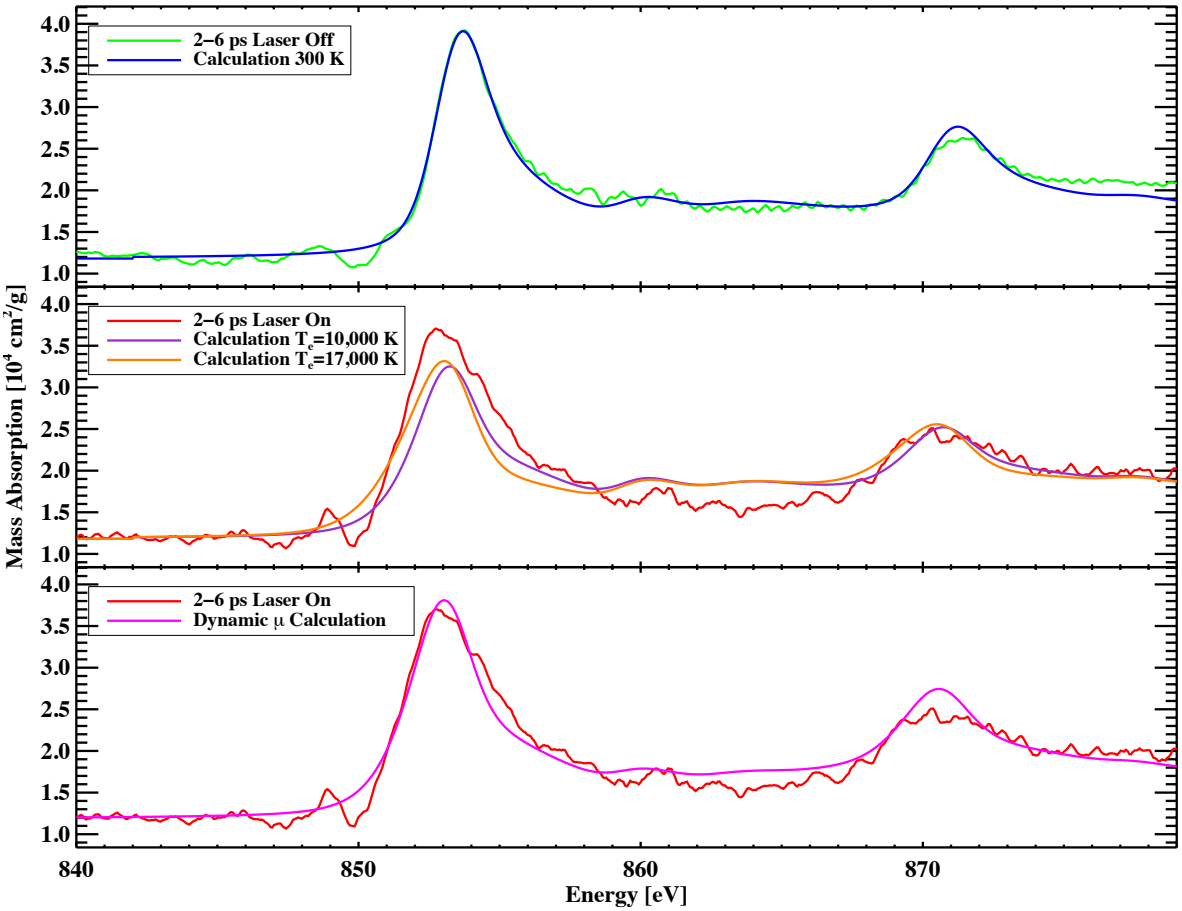

Fig. 6.5 Measured and Calculated XANES of Nickel. (Top) Measured room temperature spectrum (green) and calculated spectrum at 300K (blue). (Middle) Measured heated spectrum at 2-6 ps, calculated spectrum at 10,000K and 17,000K electron temperatures. (Bottom) Measured heated spectrum and a calculated spectrum as described in section 6.4.

The high temperature spectra generated by the method described above show unsatisfactory agreement to the observed spectra. A calculation at an electronic temperature of 10,000 K is shown in figure 6.5. The calculated shift of the absorption edge is smaller than the observed shift and the calculated height of the maximum absorption is lower than in the measured spectrum. If the temperature of the calculation is increased, the edge will shift to lower photon energy, but the slope will become too gradual and the maximum absorption will be too low. It should also be noted here that the calculation does shows a weak dependence on ion temperature. Furthermore, an attempt to account for possible sample non-uniformity, by averaging different electronic temperatures, did not improve the agreement to the observed spectra, as it also results in a reduced peak height and a broadened edge.

The slope of the absorption edge is the most direct measure of sample temperature, because in the absence of a discontinuity in the DOS or matrix elements, the shape of the edge follows the Fermi occupation function. Using the temperature dependent electron heat capacities, the expected electron temperature is in excess of 25,000K for each fluence (~25,000, 50,000, and 100,000K for 12 MJ/kg, 24 MJ/kg, and 50 MJ/kg), much higher than the electronic temperature of ~10,000K in the calculated spectrum. This difference indicates a disconnect between the calculated temperature and the laser fluence delivered to the sample. The x-ray absorption measurement is not sensitive to the p electrons because of the forbidden p-p transition.

6.4 Adjustable Chemical Potential

To reconcile the calculation and the observed spectra, the following approach is adopted. First, the chemical potential set as an adjustable parameter in addition to the electron temperature in order to match the position and slope of the absorption edge. This procedure results in a red-shift of the chemical potential by 0.305 eV while the electron temperature remains at 10,000 K. There is now good agreement with the d-band resonance, but 0.35 valence electrons remain missing from the system. These electrons are then placed uniformly in the s, p, and d bands in a uniform energy distribution extending 15 eV above the Fermi level. The number of electrons in the system is now conserved. The agreement between the calculation and experiment is dramatically improved, both near the edge and at higher energy. This result also suggests a non-equilibrium distribution of electrons, which persists over a 30 ps time scale. It is expected that electrons which initially undergo a d-p transition by the absorption of an optical photon can undergo subsequent free-free absorption creating a non-equilibrium electron distribution. Sequential multi-photon absorption must be present because the absorbed laser energy corresponds to more than 3 photons per atom, while only 0.15 electrons are within the optical photon energy, 1.55 eV, of the Fermi level. These conditions create a distribution of electrons well above the initial Fermi level. Non-equilibrium electron distributions have been observed in aluminum excited by extreme ultraviolet free electron laser radiation [120], but these distributions relax on a time scale

of a few hundred fs. The suggestion of non-equilibrium electron distributions persisting on a timescale of 30 ps is an unanticipated result.

We investigated the unoccupied electronic density of states of warm dense nickel through time-resolved x-ray absorption spectroscopy. When comparing the measured x-ray absorption spectra with molecular dynamics and density functional theory calculations, we were unable to generate agreement given a single electron temperature. Employing a model based on a non-equilibrium electron distribution, a satisfactory fit is achieved. This non-equilibrium electronic state is suggested to persist for a timescale of 10s of picoseconds.

Chapter 7

Conclusions

A novel system for time resolved x-ray absorption spectroscopy of warm dense matter has been developed at the Advanced Light source synchrotron. A femtosecond laser pulse is used isochorically heat matter to warm and dense states. An ultrafast x-ray streak camera in integrated with an x-ray beamline. Ultrafast x-ray absorption spectroscopy probes the unoccupied electronic density of states before the onset of hydrodynamic expansion or electron-ion equilibrium is reached. Through comparison with molecular dynamics and density functional theory calculations, changes in the absorption spectra can be correlated to the physical properties of the warm dense matter states. This framework has been used to successfully study three materials in warm dense matter conditions.

In warm dense silicon dioxide, a new pre-edge absorption feature was observed below the bandgap and correlated with the promotion of valence electrons into the conduction band. This indicated a high electronic temperature. Absorption within the bandgap was correlated to Si-O bonds broken, as the sample transitioned into a liquid state. Oscillations above the edge were correlated with ionic disordering, which was consistent with an ionic temperature that was lower than the electronic temperature.

In warm dense copper, the measured absorption spectra could be accurately fit with calculated spectra. This gleaned an accurate measurement of electronic temperature. The temporal evolution of the electronic temperature was studied with a two temperature model, which required the temperature dependent treatment of the electronic heat capacity and electron-phonon coupling parameter.

In warm dense nickel, changes in the absorption spectra were found to be independent of incident laser fluence. The measured spectra did not agree with the calculated spectra. Employing a model of non-equilibrium electronic distribution a good fit was achieved.

Bibliography

[1] R. W. Lee, H. A. Baldis, R. C. Cauble, O. L. Landen, J. S. Wark, A. Ng, S. J. Rose, C. Lewis, D. Riley, J. C. Gauthier, and P. Audebert, Laser Part. Beams **20**, (2003).

[2] U.S. Department of Energy, Office of Science and National Nuclear Security Administration, Basic Research Needs for High Energy Density Laboratory Physics (2009).

[3] J. W. Chan, T. Huser, S. Risbud, and D. M. Krol, Opt. Lett. **26**, 1726 (2001).

[4] M. Koenig, A. Benuzzi, B. Faral, J. Krishnan, J. M. Boudenne, T. Jalinaud, C. Rémond, A. Decoster, D. Batani, D. Beretta, and T. A. Hall, Appl. Phys. Lett. **72**, 1033 (1998).

[5] M. Ross, Nature **292**, 435 (1981).

[6] K. Sokolowski-Tinten, J. Bialkowski, A. Cavalleri, M. Boing, H. Schuler, and D. von der Linde, in *CLEO/Europe Conference on Lasers and Electro-Optics* (IEEE, 1998), pp. 259–259.

[7] K. Sokolowski-Tinten, J. Bialkomiski, M. Boing, A. Cavalleri, and D. von der Linde, in *Quantum Electronics and Laser Science Conference* (Opt. Soc. America, 1999), pp. 231–232.

[8] K. Sokolowski-Tinten, S. Kudryashov, J. Bialkowski, M. Boing, D. von der Linde, A. Cavalleri, H. O. Jeschke, M. E. Garcia, and K. H. Bennemann, in *Quantum Electronics and Laser Science Conference* (2000), p. 189.

[9] A. Benuzzi-Mounaix, F. Dorchies, V. Recoules, F. Festa, O. Peyrusse, A. Lévy, A. Ravasio, T. Hall, M. Koenig, N. Amadou, E. Brambrink, and S. Mazevet, Phys. Rev. Lett. **107**, 165006 (2011).

[10] Y. Shimotsuma, M. Sakakura, K. Miura, J. Qiu, P. G. Kazansky, K. Fujita, and K. Hirao, J. Nanosci. Nanotechnol. **7**, 94 (2007).

[11] D. D. Nolte, Solid-State Electronics **33**, 295 (1990).

[12] J. D. Lindl, *Inertial Confinement Fusion: the Quest for Ignition and Energy Gain Using Indirect Drive* (AIP Press, 1998).

[13] R. L. McCrory, J. M. Soures, C. P. Verdon, F. J. Marshall, S. A. Letzring, S. Skupsky, T. J. Kessler, R. L. Kremens, J. P. Knauer, H. Kim, J. Delettrez, R. L. Keck, and D. K. Bradley, Nature **335**, 225 (1988).

[14] B. Spears, D. Hicks, C. Velsko, M. Stoyer, H. Robey, D. Munro, S. Haan, O. Landen, A. Nikroo, and H. Huang, J. Phys.: Conf. Ser. **112**, 022003 (2008).

[15] S. P. Regan, R. Epstein, V. N. Goncharov, I. V. Igumenshchev, D. Li, P. B. Radha, H. Sawada, W. Seka, T. R. Boehly, J. A. Delettrez, O. V. Gotchev, J. P. Knauer, J. A. Marozas, F. J. Marshall, R. L. McCrory, P. W. McKenty, D. D. Meyerhofer, T. C. Sangster, D. Shvarts, S. Skupsky, V. A. Smalyuk, B. Yaakobi, and R. C. Mancini, Phys. Plasmas **14**, 056305 (2007).

[16] P. W. McKenty, V. N. Goncharov, R. P. J. Town, S. Skupsky, R. Betti, and R. L. McCrory, Phys. Plasmas **8**, 2315 (2001).

[17] R. F. Smith, J. H. Eggert, R. Jeanloz, T. S. Duffy, D. G. Braun, J. R. Patterson, R. E. Rudd, J. Biener, A. E. Lazicki, A. V. Hamza, J. Wang, T. Braun, L. X. Benedict, P. M. Celliers, and G. W. Collins, Nature **511**, 330 (2014).

[18] NASA, Http://Kepler.Nasa.Gov/Mission/Discoveries (2015).

[19] F. Birch, J. Geophys. Res. **57**, 227 (2012).
[20] P. Shearer and G. Masters, Geophysical Journal International **102**, 491 (1990).
[21] J. M. Brown, T. J. Ahrens, and D. L. Shampine, J. Geophys. Res. **89**, 6041 (1984).
[22] H. J. Melosh, in *The Formation of Uranus and Neptune Among Jupiter and Saturn*, edited by H. E. Newsom and J. H. Jones (Oxford, 1989), pp. 69–83.
[23] G. A. Glatzmaier and P. H. Roberts, Physics of the Earth and Planetary Interiors **91**, 63 (1995).
[24] M. Jakubík, A. Morbidelli, L. Neslušan, and R. Brasser, A&A **540**, A71 (2012).
[25] E. W. Thommes, M. J. Duncan, and H. F. Levison, The Astronomical Journal **123**, 2862 (2002).
[26] W. B. Hubbard, T. Guillot, M. S. Marley, A. Burrows, and J. I. Lunine, Planet. Space Sci. **47**, 1175 (1999).
[27] T. Guillot, Science **286**, 72 (1999).
[28] C. T. Russell, Rep. Prog. Phys. **56**, 687 (1999).
[29] J. Leconte and G. Chabrier, Nature Geosci. **6**, 347 (2013).
[30] Z. Lin, L. Zhigilei, and V. Celli, Phys. Rev. B **77**, 075133 (2008).
[31] W. McMillan, Phys. Rev. **167**, 331 (1968).
[32] G. Grimvall, *The Electron-Phonon Interaction in Metals* (North-Holland Pub. Co., 1981).
[33] W. Kohn and L. J. Sham, Phys. Rev. **140**, A1133 (1965).
[34] R. Car and M. Parrinello, Phys. Rev. Lett. **55**, 2471 (1985).
[35] L. B. Da Silva, P. Celliers, G. W. Collins, K. S. Budil, N. C. Holmes, T. W. Barbee Jr, B. A. Hammel, J. D. Kilkenny, R. J. Wallace, M. Ross, and R. Cauble, Phys. Rev. Lett. **78**, 483 (1997).
[36] J. Zhang, J. Yang, Y. Xu, G. Yang, Y. Ding, J. Yan, J. Yuan, Y. Ding, Z. Zheng, Y. Zhao, and Z. Hu, Phys. Rev. E **79**, 016401 (2009).
[37] G. Rochau, J. Bailey, and J. MacFarlane, Phys. Rev. E **72**, 066405 (2005).
[38] D. H. H. Hoffmann, V. E. Fortov, I. V. Lomonosov, V. Mintsev, N. A. Tahir, D. Varentsov, and J. Wieser, Phys. Plasmas **9**, 3651 (2002).
[39] T. Ao, Y. Ping, K. Widmann, D. F. Price, E. Lee, H. Tam, P. T. Springer, and A. Ng, Phys. Rev. Lett. **96**, 055001 (2006).
[40] J. F. Seely, in *Laser Interaction and Related Plasma Phenomena* (Springer US, Boston, MA, 1974), pp. 835–847.
[41] S. Brorson, J. Fujimoto, and E. Ippen, Phys. Rev. Lett. **59**, 1962 (1987).
[42] C. Suárez, W. Bron, and T. Juhasz, Phys. Rev. Lett. **75**, 4536 (1995).
[43] T. Juhasz, H. Elsayed-Ali, G. Smith, C. Suárez, and W. Bron, Phys. Rev. B **48**, 15488 (1993).
[44] J. Hohlfeld, S. S. Wellershoff, J. Güdde, U. Conrad, V. Jähnke, and E. Matthias, Chemical Physics **251**, 237 (2000).
[45] M. M. Murnane, H. C. Kapteyn, M. D. Rosen, and R. W. Falcone, Science **251**, 531 (1991).
[46] A. D. Rakic, A. B. Djurisic, J. M. Elazar, and M. L. Majewski, Appl. Opt. **37**, 5271 (1998).
[47] P. Celliers, A. Ng, G. Xu, and A. Forsman, Phys. Rev. Lett. **68**, 2305 (1992).
[48] T. G. White, J. Vorberger, C. R. D. Brown, B. J. B. Crowley, P. Davis, S. H.

Glenzer, J. W. O. Harris, D. C. Hochhaus, S. Le Pape, T. Ma, C. D. Murphy, P. Neumayer, L. K. Pattison, S. Richardson, D. O. Gericke, and G. Gregori, Scientific Reports **2**, 889 (2013).
[49] B. L. Henke, E. M. Gullikson, and J. C. Davis, Atomic Data and Nuclear Data Tables **54**, 181 (1993).
[50] J. Stöhr, *NEXAFS Spectroscopy* (Springer Berlin Heidelberg, Berlin, Heidelberg, 1992).
[51] A. Mančić, A. Lévy, M. Harmand, M. Nakatsutsumi, P. Antici, P. Audebert, P. Combis, S. Fourmaux, S. Mazevet, O. Peyrusse, V. Recoules, P. Renaudin, J. Robiche, F. Dorchies, and J. Fuchs, Phys. Rev. Lett. **104**, 035002 (2010).
[52] P. Leguay, A. Lévy, B. Chimier, F. Deneuville, D. Descamps, C. Fourment, C. Goyon, S. Hulin, S. Petit, O. Peyrusse, J. Santos, P. Combis, B. Holst, V. Recoules, P. Renaudin, L. Videau, and F. Dorchies, Phys. Rev. Lett. **111**, 245004 (2013).
[53] B. I. Cho, P. A. Heimann, K. Engelhorn, J. Feng, T. E. Glover, M. P. Hertlein, T. Ogitsu, C. P. Weber, A. A. Correa, and R. W. Falcone, Synchrotron Radiation News **25**, 12 (2012).
[54] K. J. Kim, AIP Conf. Proc. **184**, 565 (1989).
[55] D. Attwood, *Soft X-Rays and Extreme Ultraviolet Radiation* (Cambridge University Press, Cambridge, 2009).
[56] P. A. Heimann, T. E. Glover, D. Plate, H. J. Lee, V. C. Brown, H. A. Padmore, and R. W. Schoenlein, AIP Conf. Proc. **879**, 1195 (n.d.).
[57] M. P. Hertlein, A. Scholl, A. A. Cordones, J. H. Lee, K. Engelhorn, T. E. Glover, B. Barbrel, C. Sun, C. Steier, G. Portmann, and D. S. Robin, J. Synchrotron Rad. **22**, (2015).
[58] C. Sun, G. Portmann, M. Hertlein, J. Kirz, and D. S. Robin, Phys. Rev. Lett. **109**, 264801 (2012).
[59] S. Kwiatkowski, K. M. Baptiste, W. Barry, J. Julian, R. Low, D. Plate, G. J. Portmann, and D. Robin, in *Proceedings of the European Particle Accelerator Conference* (Edinburgh, Scotland, 2006), p. 3547.
[60] E. K. Zavoisky and S. D. Fanchenko, Appl. Opt. **4**, 1155 (1965).
[61] D. J. Bradley, A. G. Roddie, W. Sibbett, M. H. Key, M. J. Lamb, C. L. S. Lewis, and P. Sachsenmaier, Optics Communications **15**, 231 (1975).
[62] J. Feng, H. J. Shin, J. R. Nasiatka, W. Wan, A. T. Young, G. Huang, A. Comin, J. Byrd, and H. A. Padmore, Appl. Phys. Lett. **91**, 134102 (2007).
[63] A. F. Bartelt, A. Comin, J. Feng, J. R. Nasiatka, T. Eimüller, B. Ludescher, G. Schütz, H. A. Padmore, A. T. Young, and A. Scholl, Appl. Phys. Lett. **90**, 162503 (2007).
[64] A. M. Lindenberg, I. Kang, S. L. Johnson, T. Missalla, P. A. Heimann, Z. Chang, J. Larsson, P. H. Bucksbaum, H. C. Kapteyn, H. A. Padmore, R. W. Lee, J. S. Wark, and R. W. Falcone, Phys. Rev. Lett. **84**, 111 (2000).
[65] S. Johnson, P. Heimann, A. Lindenberg, H. Jeschke, M. Garcia, Z. Chang, R. Lee, J. Rehr, and R. Falcone, Phys. Rev. Lett. **91**, 157403 (2003).
[66] J. Feng, K. Engelhorn, B. I. Cho, H. J. Lee, M. Greaves, C. P. Weber, R. W. Falcone, H. A. Padmore, and P. A. Heimann, Appl. Phys. Lett. **96**, 134102 (2010).

[67] B. L. Henke, J. Liesegang, and S. D. Smith, Phys. Rev. B **19**, 3004 (1979).
[68] H. D. Young, R. A. Freedman, and L. Ford, *Sears and Zemansky's University Physics* (Addison-Wesley, 2006).
[69] D. P. Lowney, P. A. Heimann, H. A. Padmore, E. M. Gullikson, A. G. MacPhee, and R. W. Falcone, Review of Scientific Instruments **75**, 3131 (2004).
[70] K. Halbach and R. F. Holsinger, Part. Accel. **7**, 213 (1976).
[71] M. Berz, Nuclear Instruments and Methods in Physics Research **298**, 473 (1990).
[72] D. E. Aspnes, S. M. Kelso, R. A. Logan, and R. Bhat, J. Appl. Phys. **60**, 754 (1986).
[73] A. Mar, G. M. Loubriel, F. J. Zutavern, M. W. O'Malley, W. D. Helgeson, D. J. Brown, H. P. Hjalmarson, A. G. Baca, R. L. Thornton, and R. D. Donaldson, Plasma Science **28**, 1507 (2000).
[74] A. Rosen and F. J. Zutavern, *High-Power Optically Activated Solid-State Switches* (Artech House, 1994).
[75] E. Sakai, Nuclear Instruments and Methods in Physics Research **196**, 121 (1982).
[76] G. J. Price and G. W. Fraser, Nuclear Instruments and Methods in Physics Research **474**, 188 (2001).
[77] G. W. Fraser, Nuclear Instruments and Methods in Physics Research **206**, 445 (1983).
[78] M. M. Shakya and Z. Chang, Appl. Phys. Lett. **87**, 041103 (2005).
[79] N. Fukata, Y. Yamamoto, K. Murakami, M. Hase, and M. Kitajima, Appl. Phys. Lett. **83**, 3495 (2003).
[80] M. Boero, A. Oshiyama, P. Luigi Silvestrelli, and K. Murakami, Physica B: Condensed Matter **376-377**, 945 (2006).
[81] A. Denoeud, A. Benuzzi-Mounaix, A. Ravasio, F. Dorchies, P. M. Leguay, J. Gaudin, F. Guyot, E. Brambrink, M. Koenig, S. Le Pape, and S. Mazevet, Phys. Rev. Lett. **113**, 116404 (2014).
[82] K. Bange, C. Ottermann, and O. Anderson, in *Thin Films on Glass*, edited by H. Bach and D. Krause (Springer Berlin Heidelberg, Berlin, Heidelberg, 2003), pp. 99–223.
[83] B. El-Kareh, *Fundamentals of Semiconductor Processing Technology* (Springer US, Boston, MA, 1995).
[84] L. Martin-Samos, G. Bussi, A. Ruini, E. Molinari, and M. J. Caldas, Phys. Rev. B **81**, 081202 (2010).
[85] B. Stuart, M. Feit, A. Rubenchik, B. Shore, and M. Perry, Phys. Rev. Lett. **74**, 2248 (1995).
[86] K. Starke, D. Ristau, H. Welling, T. V. Amotchkina, M. Trubetskov, A. A. Tikhonravov, and A. S. Chirkin, in *XXXV Annual Symposium on Optical Materials for High Power Lasers: Boulder Damage Symposium*, edited by G. J. Exarhos, A. H. Guenther, N. Kaiser, K. L. Lewis, M. J. Soileau, and C. J. Stolz (SPIE, 2004), pp. 501–514.
[87] B. T. Poe, C. Romano, and G. Henderson, Journal of Non-Crystalline Solids **341**, 162 (2004).

[88] Z. Wu, F. Seifert, B. Poe, and T. Sharp, J. Phys.: Condens. Matter **8**, 3323 (1999).
[89] M. Taillefumier, D. Cabaret, A.-M. Flank, and F. Mauri, Phys. Rev. B **66**, 195107 (2002).
[90] I. Davoli, E. Paris, S. Stizza, M. Benfatto, M. Fanfoni, A. Gargano, A. Bianconi, and F. Seifert, Physics and Chemistry of Minerals **19**, (1992).
[91] F. Liebau, *Structural Chemistry of Silicates* (Springer Berlin Heidelberg, Berlin, Heidelberg, 1985).
[92] X. Gonze, B. Amadon, P. M. Anglade, J. M. Beuken, F. Bottin, P. Boulanger, F. Bruneval, D. Caliste, R. Caracas, M. Côté, T. Deutsch, L. Genovese, P. Ghosez, M. Giantomassi, S. Goedecker, D. R. Hamann, P. Hermet, F. Jollet, G. Jomard, S. Leroux, M. Mancini, S. Mazevet, M. J. T. Oliveira, G. Onida, Y. Pouillon, T. Rangel, G. M. Rignanese, D. Sangalli, R. Shaltaf, M. Torrent, M. J. Verstraete, G. Zerah, and J. W. Zwanziger, Computer Physics Communications **180**, 2582 (2009).
[93] F. Bottin, S. Leroux, A. Knyazev, and G. Zérah, Phys. Rev. B **42**, 329 (2007).
[94] J. Perdew, K. Burke, and M. Ernzerhof, Phys. Rev. Lett. **77**, 3865 (1996).
[95] M. Torrent, F. Jollet, F. Bottin, G. Zérah, and X. Gonze, Computational Materials Science **42**, 337 (2008).
[96] P. Blöchl, Phys. Rev. B **50**, 17953 (1994).
[97] V. Recoules and S. Mazevet, Phys. Rev. B **80**, 064110 (2009).
[98] S. Mazevet, M. Torrent, V. Recoules, and F. Jollet, High Energy Density Physics **6**, 84 (2010).
[99] Z. Wu, F. Seifert, B. Poe, and T. Sharp, J. Phys.: Condens. Matter **8**, 3323 (1996).
[100] G. Kresse, M. Marsman, L. E. Hintzsche, and E. Flage-Larsen, Phys. Rev. B **85**, 045205 (2012).
[101] N. Jiang and J. C. H. Spence, Ultramicroscopy **106**, 215 (2006).
[102] P. Martin, S. Guizard, P. Daguzan, G. Petite, P. D'Oliveira, P. Meynadier, and M. Perdrix, Phys. Rev. B **55**, 5799 (1997).
[103] D. Arnold, E. Cartier, and D. DiMaria, Phys. Rev. B **45**, 1477 (1992).
[104] Y. Ping, D. Hanson, I. Koslow, T. Ogitsu, D. Prendergast, E. Schwegler, G. Collins, and A. Ng, Phys. Rev. Lett. **96**, 255003 EP (2006).
[105] A. J. Nelson, J. Dunn, J. Hunter, and K. Widmann, Appl. Phys. Lett. **87**, 154102 (2005).
[106] P. A. Ni, M. I. Kulish, V. Mintsev, D. N. Nikolaev, V. Y. Ternovoi, D. H. H. Hoffmann, S. Udrea, A. Hug, N. A. Tahir, and D. Varentsov, Laser Part. Beams **26**, 583 (2008).
[107] H. J. Lee, P. Neumayer, J. Castor, T. Döppner, R. W. Falcone, C. Fortmann, B. A. Hammel, A. L. Kritcher, O. L. Landen, R. W. Lee, D. D. Meyerhofer, D. H. Munro, R. Redmer, S. P. Regan, S. Weber, and S. H. Glenzer, Phys. Rev. Lett. **102**, 115001 (2009).
[108] P. Johnson and R. Christy, Phys. Rev. B **11**, 1315 (1975).
[109] H. Ebert, J. Stöhr, S. Parkin, M. Samant, and A. Nilsson, Phys. Rev. B **53**, 16067 (1996).
[110] M. Grioni, J. Goedkoop, R. Schoorl, F. de Groot, J. Fuggle, F. Schäfers, E.

Koch, G. Rossi, J. M. Esteva, and R. Karnatak, Phys. Rev. B **39**, 1541 (1989).
[111] D. Chadi and M. Cohen, Phys. Rev. B **8**, 5747 (1973).
[112] P. Giannozzi, S. Baroni, N. Bonini, M. Calandra, R. Car, C. Cavazzoni, D. Ceresoli, G. L. Chiarotti, M. Cococcioni, I. Dabo, A. Dal Corso, S. de Gironcoli, S. Fabris, G. Fratesi, R. Gebauer, U. Gerstmann, C. Gougoussis, A. Kokalj, M. Lazzeri, L. Martin-Samos, N. Marzari, F. Mauri, R. Mazzarello, S. Paolini, A. Pasquarello, L. Paulatto, C. Sbraccia, S. Scandolo, G. Sclauzero, A. P. Seitsonen, A. Smogunov, P. Umari, and R. M. Wentzcovitch, J. Phys.: Condens. Matter **21**, 395502 (2009).
[113] D. Prendergast and G. Galli, Phys. Rev. Lett. **96**, 215502 (2006).
[114] D. Prendergast, Phys. Rev. B **80**, 235126 (2009).
[115] R. Leapman and L. Grunes, Phys. Rev. Lett. **45**, 397 (1980).
[116] J. E. Müller, O. Jepsen, and J. W. Wilkins, Solid State Communications **42**, 365 (1982).
[117] V. P. Zhukov and E. V. Chulkov, Uspekhi Fizicheskikh Nauk **179**, 113 (2009).
[118] S. I. Anisimov, B. L. Kapeliovich, and T. L. Perelman, Soviet Physics Journal of Experimental and Theorhetical Physics **39**, 375 (1974).
[119] H. Elsayed-Ali, T. Norris, M. Pessot, and G. Mourou, Phys. Rev. Lett. **58**, 1212 (1987).
[120] N. Medvedev, U. Zastrau, E. Förster, D. O. Gericke, and B. Rethfeld, Phys. Rev. Lett. **107**, 165003 (2011).